

# ON THE SURFACE WIND STRESS FOR STORM SURGE MODELING

Jie Gao

A dissertation submitted to the faculty at the University of North Carolina at Chapel Hill in partial fulfillment of the requirements for the degree of Doctor of Philosophy in the Department of Marine Sciences

Chapel Hill  
2018

Approved by:

Rick Luettich

Brian Blanton

Casey Dietrich

Johanna Rosman

John Bane

©2018  
Jie Gao  
ALL RIGHTS RESERVED

## ABSTRACT

Jie Gao: On The Surface Wind Stress For Storm Surge Modeling  
(Under the direction of Rick Luettich)

When wind blows over the open water, it exerts a shear stress at the water surface that transfers horizontal momentum vertically downward across the air–sea interface, driving the upper-ocean circulation, non-tidal sea surface elevation fluctuation, and formation of the surface wind waves. Thus, an accurate estimate of the surface wind stress is crucial to atmospheric, storm surge, and wave modeling. In this study, we have two major objectives: 1) development of a Generalized Asymmetric Holland Model (GAHM), and 2) implementation and evaluation of different surface drag laws for storm surge modeling.

Two major improvements over the classic Holland Model (HM) were made in this study. First of all, the assumption of cyclostrophic balance at radius to the maximum wind (RMW) was removed to eliminate the influence of the Rossby number ( $R_o$ ) on the gradient wind solution. Secondly, a composite wind method was employed to synthesize storm information from multiple storm isotachs. The GAHM has been fully implemented in the ADCIRC model for real-time storm surge forecast, and initial model evaluation indicated an improved forecasting skill over the classic HM, especially when dealing with TCs with a small  $R_o$ .

It is generally accepted by the storm surge modeling community that the surface drag coefficient  $C_d$  increases linearly with wind speed at low to moderate winds and levels off or even decreases at high winds. In this study, several sea state dependent surface drag laws, including

two explicit momentum flux models (RHG and DCCM), were implemented to study their behaviors under various wind and wave regimes, and to address the uncertainties in storm surge modeling. Initial evaluation suggested that the wave saturation tail level plays a big role in determining the surface stress, and the influence of the resolved part of the spectrum can be relatively small. Also, surge patterns were found to be greatly influenced by the spatial patterns of  $C_d$ , indicating a large uncertainty in storm surge modeling when using different drag laws. In the future, surge data of real hurricane cases are needed to quantify the performance of each drag law.

To my parents, and my dear husband Ao,  
without whom none of my success would be possible.

## ACKNOWLEDGEMENTS

The success of this work was only possible with the contributions of my committee members, colleagues, and collaborators. First, I want to thank my advisor Rick Luettich for giving me the opportunity to work on this exciting topic in his lab. Being a great mentor, he provided plenty of guidance but also taught me to become an independent researcher. I also want to thank my committee members, Brian Blanton, Casey Dietrich, Johanna Rosman, and John Bane for giving me constructive ideas on my research topics, and providing guidance at different stages of my graduate studies. Also, many thanks to Tetsu Hara and Isaac Ginis at the University of Rhode Island for collaborating with us, and Brandon Reichl for providing source codes and documentation of RHG and DCCM. Chapter 3 was inspired by their previous works.

I thank members in our lab, including Jason Fleming, Crystal Fulcher, Tony Whipple, Ryan Neve, Jana Haddad, and Taylor Asher, for being there for me when I needed help. I also want to thank our IT support analyst Kar Howe and our student services manager Violet Anderson for their countless help.

Last but not least, many thanks to the collaborative research STORM (a Scalable Toolkit for an Open community supporting near Realtime high resolution coastal Modeling) for funding the research, and the IT department at the University of North Carolina-Chapel Hill for providing computing resources and technical support.

## TABLE OF CONTENTS

LIST OF TABLES.....	x
LIST OF FIGURES.....	xi
1. INTRODUCTION.....	1
1.1 Parametric Vortex Wind Model.....	1
1.2 Surface Wind Stress and Drag Coefficient .....	3
1.3 Reviews of Commonly Used Surface Drag Laws .....	4
GARRATT and GFDL14: Wind Speed-Dependent $C_d$ .....	5
POWELL: Storm Sector-Dependent $C_d$ .....	6
SWELL: DSPR-Dependent $C_d$ .....	8
Wave Age and Wave Steepness: Wave Age- and Steepness-Dependent $z_0$ .....	10
1.4 Explicit Surface Wind Stress .....	12
2. DEVELOPMENT AND EVALUATION OF A GENERALIZED ASYMMETRIC HOLLAND VORTEX MODEL .....	16
2.1 Introduction .....	16
2.2 Model Description.....	21
2.2.1 The classic Holland Model (1980) .....	21
2.2.2 Derivation of GAHM's Formulas .....	23
2.2.3 Calculation of the Spatially Varying RMW .....	27
2.2.4 A Linearly-weighted Composite Wind Method .....	30

2.3 Study Cases .....	32
2.4 Model Results using the Single-Isotach Approach.....	38
2.4.1 Model Consistency at Distances to the Highest Isotach.....	38
2.4.2 Evaluation of the RMW and the Modeled Maximum Wind.....	40
2.5 Model Results using the Multiple-Isotach Approach .....	42
2.5.1 Evaluations of Composite Wind Fields .....	43
2.5.2 Model Consistency at Distances to All Available Isotach .....	47
2.6 Summary and Discussion.....	49
 3. EXPLICIT SURFACE WIND STRESS UNDER TROPICAL CYCLONES FOR STORM SURGE MODELING .....	 52
3.1 Introduction .....	52
3.1.1 RHG and DCCM .....	52
3.1.2 Objectives .....	55
Sensitivity Study of the Explicit Surface Wind Stress on diagnostic tail and prognostic 2D spectrum.....	56
Impact of Different Drag Laws on Storm Surge Modeling .....	57
3.2 Methodology .....	58
3.2.1 Implementation of Sea State Dependent Stress in the Coupled ADCIRC + SWAN.....	58
3.2.2 Experimental Design.....	61
Experiment A .....	62
Experiment B .....	62
3.3 Sensitivity Study of the Explicit Sea State Dependent Stress.....	62
3.3.1 Directionally-integrated Wave Spectra and Saturation Spectra .....	62
3.3.2 Integrated Wave Form Stress .....	71



3.3.3 Sensitivity of $C_d$ to Prognostic Wave Spectrum and Diagnostic spectral tail .....	77
Deep Water .....	77
Shallow Water .....	81
3.3.4 Summary and Conclusions .....	85
3.4. Storm Surge Study using Different Drag Laws .....	86
3.4.1 Drag Comparison among Different Methods .....	86
3.4.2 Influence on Storm Surge .....	90
3.4.3 Summary and Conclusions .....	92
4. DISCUSSION AND CONCLUSIONS .....	94
4.1 Discussion on the GAHM .....	94
4.2 Discussion on Surface Wind Stress and Storm Surge Modeling .....	95
REFERENCES .....	99

## LIST OF TABLES

Table

2.1	Meteorological details of seven recent hurricanes listed in chronological order .....	33
2.2.	Parameters of storm characteristics at three snapshots of Irene (2011) .....	38
2.3.	Statistical analysis of modeled winds at distances to all isotachs based on all seven storms .....	49
3.1.	Drag laws in ADCIRC.....	56
3.2.	Physics packages in SWAN.....	58
3.3	Input and output list for RHG and DCCM .....	59
3.4.	Specification of saturation tails in this study .....	60

## LIST OF FIGURES

### Figure

1.1	Measured $C_d$ from different field and laboratory studies, showing a large spread (Black et al. (2007)). The squares, plus signs, and diamonds are CBLAST observations from different quadrants of the storms. ....	4
1.2	Comparison of $C_d$ among GARRATT (capped at $2.5 \times 10^{-3}$ ), GFDL14, and SWAN-FIT. ....	6
1.3	Different behaviors of $C_d$ in the rear, right and left storm sectors by Powell et al. (2007). ....	7
1.4	$C_d$ values sorted over three storm sectors by Holthuijsen et al. (2012). ....	9
1.5	The geographic pattern of the calculated wave directional spreading for Hurricane Luis (1995) in Panel A and Fran (1996) in Panel B by Holthuijsen et al. (2012). The contours of $\sigma_\theta = 45^\circ$ and $\sigma_\theta = 50^\circ$ are indicated with black dashed lines. Black arrow indicates the hurricane motion. ....	9
1.6	(A) The drag coefficient of Ho12 via (1.8), and (B) The drag coefficient with the expression of Wu (1982) capped at $2.5 \times 10^{-3}$ by Holthuijsen et al. (2012). ....	10
2.1	Profiles of $B_g/B$ (left panel) and $\varphi$ (right panel) with respect to $\log_{10} R_o$ , given different $B$ values as shown in different colors. ....	25
2.2	The normalized gradient wind profiles of the HM (left panel) and the GAHM (right panel) as functions of the normalized radial distances and $R_o$ , given different Holland $B$ values. ....	26
2.3	Slices of the normalized gradient wind profiles (as shown in Figure 2.2) at $\log_{10} R_o = 0, 1, \text{ and } 2$ (or correspondingly $R_o = 1, 10, \text{ and } 100$ ). ....	27
2.4	Best tracks and Intensity of seven selected Hurricanes used in this study. Black lines represent hurricane best tracks, and dots represent data entries with 6-hour intervals (occasionally there are exceptions), colored by the maximum sustained wind. ....	35
2.5	Same as Figure 2.4, but dots are colored by Holland $B$ . ....	36
2.6	Same as Figure 2.4 but dots are colored by $R_o$ in base 10 logarithmic scale (averaged over four storm quadrants). ....	37

2.7	Radial wind profiles of Irene (2011) at three different stages. Vertical bars represent the storm isotachs reported in NHC’s “best track” file. The highest isotach (utilized) in each quadrant are plotted in black, while lower isotachs (not utilized) are in gray. ....	39
2.8	Comparison of the modeled and “Best Track” $V_m$ (upper two panels) and the modeled and “Best Track” $R_{max}$ (lower two panels) between the AHM and the GAHM based on all seven hurricanes. ....	41
2.9	Three-dimensional snapshots of Irene’s radial wind profiles (left) and interpolated spatial wind field (right) by the single-isotach approach (upper two panels) and the multiple-isotach approach (lower two panels). ....	43
2.10	Three snapshots (in columns) of Irene’s two-dimensional wind fields by the AHM, GAHM, SLOSH, H*Wind and OWI winds corresponding to Table 2.2. ....	45
2.11	Comparison of the modeled and “Best Track” $V_m$ (upper five panels) and the modeled and “Best Track” $R_{max}$ (lower five panels) based on all seven hurricanes between the AHM, the GAHM, the SLOSH, the H*Wind and OWI winds. ....	46
2.12	GAHM’s composite radial wind profiles of Irene (2011) at 3 different developing stages. Vertical bars represent all available storm isotachs reported in NHC’s “best track” file. ....	48
2.13	Comparison of specified isotachs and modeled winds at distances to specified isotachs for all seven selected hurricanes. ....	49
3.1	Directionally integrated saturation spectrum simulated in WWIII with WWIII original tail, three constant tail level options, and empirical tail of Elfouhaily et al., 1997 for (a) 10 m/s wind, and (b) 40 m/s wind experiments. Three vertical dashed lines represent wavenumbers corresponding to $f_p$ , $1.25 \times f_p$ , and $3 \times f_p$ (Reichl et al., 2014). ....	54
3.2	Coupling different drag laws to ADCIRC+SWAN. ....	59
3.3	Intensity and Best Track of Hurricane Irene (08/20/2011 00:00:00 – 08/29/2011 00:00:00 UTC). Model results are investigated at two instances indicated by the circles. ....	61
3.4	Spatial wind field at two snapshots: 08/26/2011 03:00 UTC (left panel) and 08/28/2011 21:00 UTC (right panel). Diagnostic stations are shown in white dots. ....	63

3.5	Comparison of 1-D wave spectra (left column) and the corresponding saturation spectra (right column) among Komen, Janssen, and Westhuysen in SWAN at eight stations (shown with different colored lines) at the first snapshot (08/26/2011 03:00 UTC). Three vertical (dashed) lines from left to right in each panel represent the wavenumbers corresponding to $f_p$ , $1.2 \times f_p$ , and $3 \times f_p$ of the first station. ....	65
3.6	Comparison of 1-D wave spectra (left column) and the corresponding saturation spectra (right column) attached with the Reichl's empirical tail among three different physics packages at the first snapshot. ....	66
3.7	Comparison of 1-D wave spectra (left column) and the corresponding saturation spectra (right column) attached with the extended tail among three different physics packages at the first snapshot. ....	67
3.8	Same as Figure 3.5 but at the second snapshot (08/28/2011 21:00 UTC). ....	68
3.9	Same as Figure 3.6 but at the second snapshot (08/28/2011 21:00 UTC). ....	69
3.10	Same as Figure 3.7 but at the second snapshot (08/28/2011 21:00 UTC). ....	70
3.11	Wave spectra, saturation spectra, and integrated wave form stress profiles at 08/26/2011 03:00 UTC: a) Directionally integrated SWAN wave spectra using Komen physics package, b) SWAN saturation spectra, c) SWAN spectra with Reichl's empirical tail, d) Saturation spectra with Reichl's empirical tail, d) 1-D wave form stress over k, e) CDF of 1-D form stress over k. ....	73
3.12	Wave spectra, saturation spectra, and integrated wave form stress profiles at 08/26/2011 03:00 UTC for the extended tail option at 08/26/2011 03:00 UTC. ....	74
3.13	Same as Figure 3.11, except at 08/28/2011 21:00 UTC when wave field reaches steady state. ....	75
3.14	Same as Figure 3.12, except at 08/28/2011 21:00 UTC when wave field reaches steady state. ....	76
3.15	Spatial plot of wind speed, $C_d$ , Saturation tail level, and DSPR at 08/26/2011 00:00 UTC for Reichl's empirical tail option. ....	79
3.16	Same as Figure 3.22, but for the extended tail option at 08/26/2011 00:00 UTC. ....	80

3.17	3D plot of Wind (x), DSPR (y), $C_d$ (z) and Saturation level B (color) for Reichl's empirical tail option (upper panel)) and the extended tail (lower panel)) at 08/26/2011 00:00 UTC. ....	81
3.18	Same as Figure 3.15 for Reichl's empirical tail option, but for shallow water at 08/26/2011 00:00 UTC. ....	83
3.19	Same as Figure 3.16 for the extended tail option, but for shallow water at 08/26/2011 00:00 UTC. ....	84
3.20	Same as Figure 3.17, but for shallow water at 08/27/2011 06:00 UTC. ....	85
3.21	Spatial plots of the wind speed, $C_d$ from DCCM, water elevation and a few wave for the deep water condition at 08/26/2011 00:00:00 UTC. ....	87
3.22	Spatial distribution of $C_d$ among different drag laws at 08/26/2011 00:00:00 UTC. Upper panels from left to right: Garratt, GFDL14, Powell, Swell (Ho12). Lower panels from left to right: RHG, DCCM, Wave Age (D03) and Wave Steepness (YT01). ....	88
3.23	Comparison of $C_d$ as a function of wind speed at 08/26/2011 00:00:00 UTC. ....	88
3.24	Same as Figure 3.21, but at 08/27/2011 06:00:00 UTC. ....	89
3.25	Same as Figure 3.22, but at 08/27/2011 06:00:00 UTC. ....	90
3.26	Same as Figure 3.23, but at 08/27/2011 06:00:00 UTC. ....	90
3.27	Spatial plot of Maximum water elevation resulted from different drag laws. ....	91
3.28	Using Garratt as bench mark, Maximum water elevation from different drag laws relative to Garratt. ....	92

## **CHAPTER 1: INTRODUCTION**

### **1.1 Parametric Vortex Wind Model**

Timely and accurate estimate of the surface pressure and wind fields of a tropical cyclone (TC) is critical to storm surge forecasting and coastal risk assessment. Currently, prediction of a TC's wind field can be achieved through multiple approaches. One approach is through the use of atmospheric models, which are either statistical, dynamical, or combined statistical-dynamical, to obtain wind forecasts or nowcasts. The statistical ones empirically predict the evolution of a TC by extrapolating from historical datasets, while the dynamical models solve the full set of primitive equations of fluid flow in the atmosphere to obtain numerical results, which are quite computationally intensive.

In recent years, the kinematic analysis approach showed promise to offer more realistic and accurate wind estimates, either in real-time or in hindcast mode. One example is the Surface Wind Analysis System (H\*Wind) operated by the Hurricane Research Division (HRD) before 2014, which produces H\*Wind snapshots of TCs from 1993 – 2013 by assimilating all available surface wind observations (e.g., from ships, buoys, coastal platforms, reconnaissance aircrafts, and satellites, etc.) into a common framework for height (10m), exposure, and averaging period (Powell et al., 1996). Given its versatile inputs, the H\*Wind products are considered to be among the most sophisticated and reliable surface wind reconstructions.

A third approach, which is the parametric approach, is favored for its simplicity and lower cost that are vital for timely operational forecasting. In this approach, the surface wind

field of a TC can be estimated as the sum of the storm vortex winds and the background winds of the environment. The vortex winds are usually depicted by a radial wind profile, whose formula is either derived from the gradient or cyclostrophic wind balance equation, or simply an empirical expression acquired from historical storm events. The background winds are of a much larger scale, and among other factors, are responsible for steering the movement of a TC (Shapiro, 1983) and considered to account for some of the asymmetry observed in the overall wind field. Currently, there is no clear consensus on how to determine the distribution of background winds due to insufficient observational data. In many applications, it was common to set the background winds equal to the storm's translational velocity  $\vec{V}_T$  (e.g., Powell et al., 2005; Mattocks and Forbes, 2008), while in many others, the background winds were assumed to be in the same direction as  $\vec{V}_T$  but with reduced magnitudes by various factors (e.g., radially varies between 0-0.5 by Jelesnianski et al., 1992, Phadke et al., 2003, and Hu et al., 2012; azimuthally varies between 0-0.5 by Georgiou, 1985, and Xie et al., 2006; constant 0.6 by Emanuel et al., 2006; constant 0.5 by Lin et al., 2012a). Lin and Chavas (2012b) introduced a methodology via vector decomposition of H\*Wind surface wind fields to investigate the relationship between the surface background winds and  $\vec{V}_T$ , and found that statistically the surface background winds are reduced by a factor of  $\alpha = 0.55$  and rotated counter-clockwise (in the Northern Hemisphere) by an angle of  $\beta = 20^\circ$  relative to  $\vec{V}_T$ .

The classic Holland Model (HM, 1980) is one of most commonly used analytical vortex models, which is also one of the meteorological forcing options in the ADCIRC storm surge model (NWS = 19). A thorough look at its formulation reveals that the HM suffers a few flaws due to the assumptions made during its derivation. Development of a more generalized Holland Model is presented in Chapter 2.



## 1.2 Surface Wind Stress and Drag Coefficient

When wind blows over the open water, it exerts a shear stress at the water surface that transfers horizontal momentum vertically downward across the air–sea interface, driving the upper-ocean circulation, non-tidal sea surface elevation fluctuation, and formation of the surface wind waves. Thus, an accurate estimate of the surface wind stress is crucial to atmospheric, storm surge, and wave modeling. In common practice, the surface wind stress in storm surge model is parameterized using the bulk formula

$$\vec{\tau} = \rho_a C_d \vec{U}_{10} |\vec{U}_{10}|, \quad (1.1)$$

where  $\rho_a$  is the density of air,  $C_d$  is the surface drag coefficient, and  $\vec{U}_{10}$  is the wind speed at 10m height. Assuming neutral stability, the mathematical representation of the mean wind velocity profile within the atmospheric boundary layer (ABL) is given by the logarithmic law

$$\frac{u}{u_*} = \frac{1}{\kappa} \ln \frac{z}{z_0}, \quad (1.2)$$

where  $u$  is the wind speed at height  $z$ ,  $\kappa$  is the von Karman constant (determined experimentally to be  $\sim 0.40$ ),  $z_0$  is the surface roughness length, and  $u_*$  is the friction velocity defined by

$$|\vec{\tau}| = \rho_a u_*^2. \quad (1.3)$$

Charnock (1955) proposed that a simple non-dimensional relation exists between  $z_0$  and  $u_*$

$$\alpha = \frac{z_0 g}{u_*^2}, \quad (1.4)$$

where  $\alpha$  is the so-called Charnock constant, typically ranging from 0.015 to 0.035 depending on different sea state, and  $g$  is the acceleration due to gravity. Here, sea state refers to the general

condition of the ocean surface with respect to wave characteristics such as wave height, period, or wave spectrum at a given time and location. Based on Eqs. 1.1~1.4,  $C_d$  can be rewritten as

$$C_d = \left( \frac{u_*}{|\bar{U}_{10}|} \right)^2 \text{ or } C_d = \left( \kappa / \ln \left( \frac{10}{z_0} \right) \right)^2. \quad (1.5)$$

The drag coefficient therefore can be regarded as a measure of the roughness of the sea, and is influenced by many factors such as the wind speed, atmospheric stability, and sea state, etc.

### 1.3 Reviews of Commonly Used Surface Drag Laws

Many approaches have been developed to estimate the surface wind stress  $\vec{\tau}$  (or described in terms of surface roughness  $z_0$  or surface drag coefficient  $C_d$ ). However, results are far from conclusive, especially under a wide range of wind and wave regimes (Figure 1.1). In this section, a few common surface drag laws are described in detail.

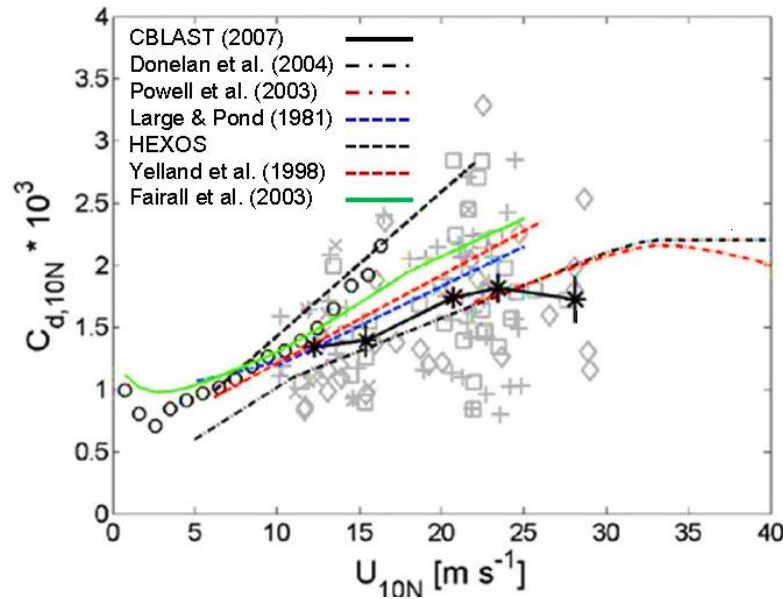


Figure 1.1 Measured  $C_d$  from different field and laboratory studies, showing a large spread (Black et al. (2007)). The squares, plus signs, and diamonds are CBLAST observations from different quadrants of the storms.

### **GARRATT and GFDL14: Wind Speed-Dependent $C_d$**

The majority of previous studies were conducted in low to moderate wind regimes lower than 25 m/s. Their results suggest that  $C_d$  is wind speed-dependent and can be expressed as a linear function of  $|\vec{U}_{10}|$  (e.g., Garratt, 1977; Smith, 1980; Large and Pond, 1981; Wu, 1982; Yelland and Taylor, 1996)

$$C_d \times 10^3 = a + b|\vec{U}_{10}|, \quad (1.6)$$

where parameters  $a$  and  $b$  are empirically determined. For the GARRATT drag law,  $a=0.75$  and  $b=0.067$ . Equation (1.6) predicts a monotonic increase of  $C_d$  with wind speed, and in extreme wind speeds values of  $C_d$  are simply extrapolated. Wind measurements under hurricane wind forcing were made available via the use of the Global Positioning System (GPS) dropsondes. Powell et al. (2003, hereinafter P03) analyzed 331 GPS dropsonde data from 15 storms (1997-1999) and concluded that, contrary to previous thoughts,  $C_d$  tends to level off around ~34 m/s and then decrease with increasing wind speed, possibly due to air-flow separation and the existence of sea spray and white-capping at high winds. Laboratory tank measurements by Donelan et al. (2004) and theoretical studies by Soloviev et al. (2014) predicted a similar behavior of  $C_d$  to drop off at high wind speeds. To adopt these new findings, a cap value can be simply applied to existing formulas to represent the leveling off of  $C_d$  at high wind speeds. In ADCIRC, Garratt's formula is typically capped at  $2.5 \times 10^{-3}$  or  $3.5 \times 10^{-3}$ .

A more sophisticated approach is to fit a polynomial curve to capture the leveling off and then decreasing of  $C_d$  at high wind speeds, such as the GFDL14 drag law used in the GFDL hurricane model, and SWAN-FIT, the 2<sup>nd</sup> order polynomial implemented in SWAN (Zijlema et al., 2012) as an alternative to Wu's linear formula. A comparison of  $C_d$  is given by Figure 1.2.

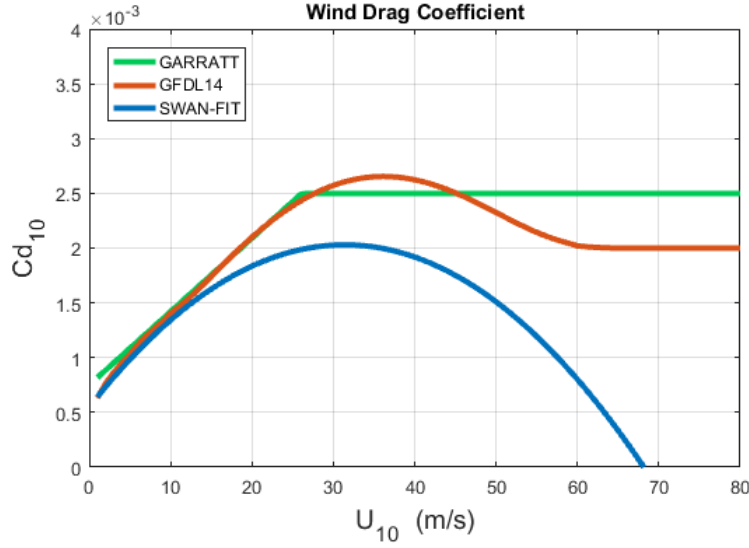


Figure 1.2. Comparison of  $C_d$  among GARRATT (capped at  $2.5 \times 10^{-3}$ ), GFDL14, and SWAN-FIT.

### POWELL: Storm Sector-Dependent $C_d$

In the Coupled Boundary Layer Air-Sea Transfer (CBLAST, 2000-2005) field experiment, Black et al. (2007) identified three storm sectors with distinctive wave characteristics, partitioned by the  $20^\circ$ ,  $150^\circ$  and  $240^\circ$  angle relative to the storm forward motion:

- 1) Rear sector with unimodal, short-wavelength ( $\sim 150 - 200$ m) waves moving with the wind, 2) Right sector with bimodal or trimodal spectra shifting to longer wavelengths ( $\sim 200 - 300$ m) moving outward by up to  $45^\circ$  relative to the wind directions, and 3) Left sector with unimodal spectra, peak long-wavelength waves ( $\sim 200 - 350$ m) moving outward relative to the wind by  $60^\circ - 90^\circ$ .

Following closely to the work by Black et al. (2007), Powell et al. (2007, hereinafter P07) extended P03 and examined a composite of GPS dropsonde datasets to investigate the azimuthal behavior of  $C_d$ . Their results indicate that  $C_d$  varies differently with wind speed in different storm-relative sectors, as shown in Figure 3.3: 1) In the rear sector ( $151 - 240^\circ$ ),  $C_d$  is fairly

constant and decreases at wind speed above 34 m/s, 2) In the right sector (20 - 150°),  $C_d$  is relatively constant with wind speed, but a slight increase was suggested at wind speed above 45 m/s, and 3) In the front left sector (241 - 20°),  $C_d$  is the most sensitive to wind speed, and increases to a maximum value of  $4.7 \times 10^{-3}$  at wind speed of 36 m/s and then decreases rapidly at higher winds.

Powell's findings contradicted numerical modeling results by Moon et al. (2004), who estimated a higher  $C_d$  in the right and front of the storm where longer, higher, and more fully developed waves dominate, and a lower  $C_d$  in the rear and left of the storm with shorter and younger waves. It is recommended that further investigations be conducted in light of this inconsistency. Powell's storm sector-dependent  $C_d$  formula has been implemented in ADCIRC (Dietrich, 2010) as an alternative to Garratt's formula.

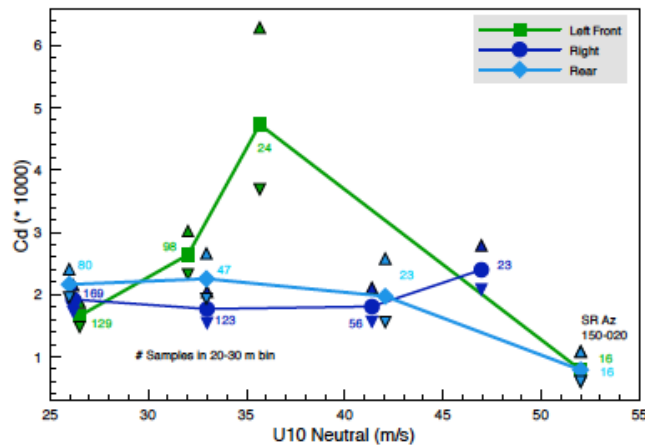


Figure 1.3. Different behaviors of  $C_d$  in the rear, right and left storm sectors by Powell et al. (2007)

### **SWELL: DSPR-Dependent $C_d$**

Partition of the three storm sectors in Black et al. (2007) is always conducted at fixed angles relative to the storm forward motion, and the attribution of swell type is always categorized (following, opposing or cross swell). Parameterization of  $C_d$  based on three swell types is problematic, as the physical processes influencing the surface wind drag should not vary discontinuously with swell type and in geographic space, and should not depend on storm forward motion. To resolve this issue, Ho12 proposed to grade swell type continuously using the wave directional spreading variable DSPR  $\sigma_\theta$ , which by definition accounts for the swell in proportion to its energy relative to the energy of local windsea. DSPR is defined as (in analogy with the definition of standard deviation):

$$\sigma_\theta^2 = \langle \sin^2(\theta) \rangle, \quad (1.7)$$

where  $\theta$  is the wave direction relative to the mean wave direction, and the operator  $\langle \rangle$  represents the average over spectral direction weighted with wave energy density (Battjes, 1972). Typically,  $\sigma_\theta$  is  $\sim 30^\circ$  for a pure windsea without swell (Holthuijsen, 2007), and grows significantly larger if crossing and opposing swell exist.

Ho12 sorted the  $C_d$  values obtained from 1149 GPS dropsondes wind profiles (1998-2005) over the three storm sectors (or equivalently the three types of swell) in different wind speed groups (Figure 1.4), and derived an informally fitted empirical expression of  $C_d$  in terms of  $|\bar{U}_{10}|$  as a preliminary assessment:

$$C_d \times 10^3 = \min \left\{ \left[ a + b \left( \left| \bar{U}_{10} \right| / \left| \bar{U}_{ref,1} \right| \right)^c \right], d \left[ 1 - \left( \left| \bar{U}_{10} \right| / \left| \bar{U}_{ref,2} \right| \right)^e \right] \right\}. \quad (1.8)$$

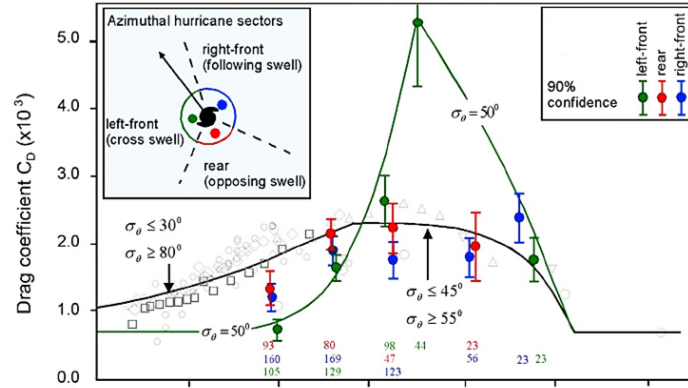


Figure 1.4.  $C_d$  values sorted over three storm sectors by Holthuijsen et al. (2012)

Based on case studies of Hurricane Luis (1995) and Fran (1996), Ho12 found that the  $45^\circ$  and  $55^\circ$  contour lines of  $\sigma_\theta$  corresponded reasonably well with the boundaries of the three storm sectors (Figure 1.5), which provides the range of validity of (1.8) and its coefficients in terms of  $\sigma_\theta$ .

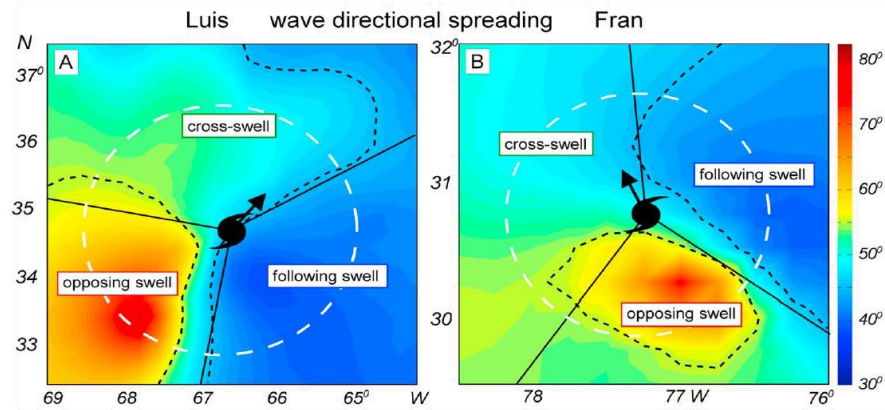


Figure 1.5. The geographic pattern of the calculated wave directional spreading for Hurricane Luis (1995) in Panel A and Fran (1996) in Panel B by Holthuijsen et al. (2012). The contours of  $\sigma_\theta = 45^\circ$  and  $\sigma_\theta = 50^\circ$  are indicated with black dashed lines. Black arrow indicates the hurricane motion.

Ho12 tested this  $\sigma_\theta$ -dependent  $C_d$  parameterization for Hurricane Katrina (2005), and found that both the estimated  $C_d$  and surface wind stress fields contrasted sharply with previously accepted views (Figure 1.6). Holthuijsen's work draws our great attention, as this new

parameterization obviously would result in different outcomes in wind, wave, and storm surge predictions if it were used. We plan to implement and test the Ho12 parameterization in the coupled ADCIRC and SWAN model in the future.

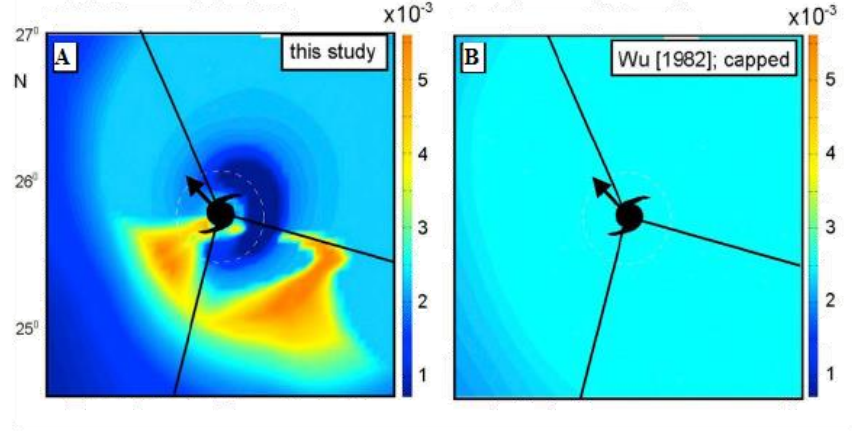


Figure 1.6. (A) The drag coefficient of Ho12 via (1.8), and (B) The drag coefficient with the expression of Wu (1982) capped at  $2.5 \times 10^{-3}$  by Holthuijsen et al. (2012).

### Wave Age and Wave Steepness: Wave Age- and Steepness-Dependent $z_0$

It has long been recognized that sea state plays an important role in affecting the surface momentum flux at the air-sea interface, and many attempts have been made to relate surface wind stress (or equivalently  $C_d$ ,  $z_0$  or  $\alpha$ ) to wave parameters that characterize the sea state. Consider a pure windsea with a single spectral peak, free of contamination from swell. The windsea usually has a universal spectral shape that results from the coupled system of wind, wind waves, and surface currents. Therefore, the local windsea can be characterized by the phase velocity at the spectral peak  $c_p$ , and similarly, the momentum flux through the coupled system can be characterized by  $u_*$  or  $|\vec{U}_{10}|$ . Thus, it is possible to represent the developmental stage of the sea with a dimensionless “wave age”  $c_p/u_*$  or  $c_p/|\vec{U}_{10}|$ . Older waves that travel close to the wind speed do not contribute much drag; while younger waves are the main rough elements.



Thus, wave age is a plausible candidate to describe the sea surface roughness. Kitaigorodskii and Volkov (1965) made the first attempt to relate sea surface roughness to the sea state, and proposed that the Charnock's constant  $\alpha$  depends on wave age. Since that, numerous efforts have been made in the field and laboratories to find the relation between  $z_0$  and  $c_p/u_*$ , but no definitive conclusions have been reached (e.g., Geernaert 1986; Toba et al. 1990; Smith et al. 1992; Donelan et al. 1993; Oost et al. 2002; Drennan et al. 2003). Part of the problem lies in the fact that by definition both  $z_0$  and wave age depend on  $u_*$ , which could lead to potential spurious correlations between these two variables (Kenney, 1982). To eliminate the issue, Drennan et al. (2003, hereinafter D03) combined five datasets of different sources that represent a variety of wind-wave conditions, and concluded that a power-law relation exist between  $z_0/H_s$  and the inverse wave age

$$z_0/H_s = 3.35(u_*/c_p)^{3.4}, \quad (1.9)$$

where  $H_s$  is the significant wave height. Equation (1.9) implies that younger waves are rougher than older waves. Note that for wind-waves in local equilibrium with the wind, there is a strong statistical interdependence between the variables in (1.9). Thus, the extent to which the wave age-dependent formula differs from or has in common with the conventional wind speed-dependent formula under different wind-wave conditions is a question that needs to be answered. Also, a clear wave age-dependent surface drag has not been observed in open ocean under hurricane wind forcing, so we should be cautious to use it in storm surge modeling.

Hsu (1974) took a different path to relate surface roughness to the sea state, and suggested that  $z_0$  depended on the wave slope  $H_s/L_p$ , where  $L_p$  is the wavelength of waves at the peak frequency. Using measurements from three field experiments, Taylor and Yelland

(2001, hereinafter TY01) proposed a wave steepness-dependent formula, which predicts a power law relation between the dimensionless roughness  $z_0/H_s$  and steepness of the dominant waves

$$z_0/H_s = 1200(H_s/L_p)^{4.5} . \quad (1.10)$$

Using this formula, the roughness changes due to fetch or duration limitations are small. Equation (1.10) reconciles many observations that previously had appeared scattered, except for data corresponding to very young waves. Drennan et al. (2005) evaluated both D03 and TY01 using eight assembled datasets, and found that these two methods yielded rather different estimates of roughness depending on the sea states. Each method has its own merits and limitations: 1) in conditions with a dominant wind sea, both methods yield better estimates than the traditional bulk formula, 2) in general conditions with mixed sea, the steepness method performs better, 3) for underdeveloped younger wind sea, the wave age method yields better results, and 4) for swell-dominated conditions, neither methods did well. Implementation of both methods does not require explicit knowledge of the wave spectrum.

#### **1.4 Explicit Surface Wind Stress**

Wave field associated with a hurricane is rather complex both in space and time due to the translational nature of a hurricane and the curvature of the winds, an explicit parameterization of surface wind stress that depends on the 2D wave spectrum is desired. We hope that by incorporating the 2D wave spectrum (both the long wave spectrum and short wave spectrum tail) into the stress formulations, more physics can be captured to explain the large amount of scatters in the surface drag measurements.

Since the pioneering work on wind wave evolution by Miles (1957) and Phillips (1958), considerable efforts have been made to study the spectral shape and equilibrium range of wind

waves. The most important contribution on the shape of wave spectrum comes from the JOint North Sea Wave Project (JONSWAP, Hasselmann et al., 1973), in which a universal spectral shape (normalized over spectral peak) was found for waves in idealized fetch-limited, deep water conditions. Waves in the equilibrium range are quasi-saturated, meaning that their slope is limited by breaking and does not increase much with wind speed. Up until now, our knowledge of the wave spectrum in the equilibrium range is still limited, especially under high wind conditions. There is debate over the shape of the high frequency spectral tail, but the  $f^{-5}$  tail (Phillips, 1958; Pierson and Moskowitz, 1964; JONSWAP, Hasselmann et al., 1973) and the  $f^{-4}$  tail (Toba, 1973; Donelan et al., 1985; Hwang et al., 2000) are most widely used. Note, wave spectra in wavenumber space and in frequency space can be inter-changed using straightforward Jacobian transformations. The  $k^{-4}$  tail corresponding to the  $f^{-5}$  tail in frequency spectrum is most often used in a wavenumber spectrum. Numerical wave models typically resolve wave spectrum to a certain frequency, and an empirical tail needs to be attached to extend the spectrum to high frequency range.

Based on conservation of momentum in the marine boundary layer, Janssen (1989) and later Chalikov and Makin (1991) introduced a theory that takes into account the directional wavenumber spectrum  $\Psi(k, \theta)$  to describe the exchange of momentum at the air-sea interface, where  $\Psi(k, \theta)$  is defined as

$$\overline{\eta^2} = \int_0^k \int_{-\pi}^{\pi} \Psi(k, \theta) d\theta d\vec{k}, \quad (1.11)$$

with  $\overline{\eta^2}$  being the mean square surface displacement. The total stress is supported by both the turbulent motions of the air  $\tau_t$  and the wave-induced motions due to the wind waves  $\tau_f$

$$\vec{\tau} = \vec{\tau}_t(z) + \vec{\tau}_f(z). \quad (1.12)$$

At the sea surface  $z = 0$  the total flux equals to the sum of the viscous stress  $\tau_v \equiv \tau_t(0)$  and form stress  $\tau_f \equiv \tau_f(0)$ . The viscous stress comes through the direct molecular interaction at the surface, and can be calculated from the law of smooth wall, with viscous drag coefficient adjusted for the sheltering effect in the presence of waves (Donelan et al., 2012), and the form stress is given by the rate of change of wave momentum in time due to the wind source input

$$\vec{\tau}_f = \int \frac{\partial}{\partial t} \vec{P}_{wind} d\vec{k}. \quad (1.13)$$

To characterize the input rate of momentum from the atmosphere to waves, here we define

$$\frac{\partial}{\partial t} \vec{P}_{wind} = \beta(k, \theta) \vec{P}_{wind}, \quad (1.14)$$

where  $\vec{P}_{wind}$  is the pressure exerted on the water surface by wind, and  $\beta(k, \theta)$  is the wave growth rate. Parameterization of  $\beta(k, \theta)$  varies in different studies. Assuming dispersion relation  $\omega^2 = gk$ , the wave momentum is given by (Phillips, 1977)

$$\vec{P}_{wind} = \rho_w \frac{\omega}{k} \Psi(k, \theta) \vec{k}, \quad (1.15)$$

where  $\rho_w$  is the density of water, and  $\omega$  is the wave frequency. Combining Eqs. (1.13~1.15), the form drag can be expressed as

$$\vec{\tau}_f = \rho_w \int_0^k \int_{-\pi}^{\pi} \omega \beta(k, \theta) \Psi(k, \theta) d\theta d\vec{k} d\vec{k} \quad (1.16)$$

In a fully developed sea, waves near the spectral peak propagate close to the wind speed and thus do not contribute much form drag to the total stress. Intuitively, the rough elements of the form drag in this situation come from the steep shorter waves in the spectral tail. The flaw of

these types of model is that the form drag calculated using (1.16) is very sensitive to the high frequency tail, and there is little known about the spectral tail under hurricane wind conditions.

Both the RHG and DCCM are explicit momentum flux models. Their description and model implementation in the coupled ADCIRC+SWAN will be carried out in Chapter 3 (along with other described drag laws in Section 1.3). Investigation of different drag laws on storm surge modeling will also be conducted.

## CHAPTER 2: DEVELOPMENT AND EVALUATION OF A GENERALIZED ASYMMETRIC HOLLAND VORTEX MODEL

### 2.1 Introduction

There are many kinds of parametric wind models exist, which use similar sets of storm parameters but distinct methods to offer TC pressure and wind estimates. One example is the SLOSH (Sea, Lake, and Overland Surges from Hurricanes, Jelesnianski et al., 1992) wind model, which is among the most important features of the SLOSH storm surge model currently used by the National Weather Service (NWS) for storm surge guidance. The SLOSH describes a circularly-symmetric storm vortex superimposed upon the background winds calculated from  $\vec{V}_T$ . It takes the radius to maximum wind (RMW) and central pressure deficit as its key model inputs, and first estimates the maximum wind empirically and then solves for the pressure and wind fields. Houston et al. (1999) did a model comparison between analyzed wind observations and the SLOSH modeled winds for seven cases in five hurricanes, and found that the SLOSH underestimated the peak winds by 15% in Hurricane Emily (1993), and by 6% or less in the rest cases. Also, the mean wind speed and mean inflow angle for the SLOSH winds were 14% stronger and 19° less than those observed in the region of strongest winds.

Another example is the classic Holland Model (1980, hereafter HM), which is a pressure-wind relationship model that features two shape parameters  $A$  and  $B$  in its radial pressure and wind profile equations. By assuming a cyclostrophic balance in the region of maximum winds, where the Coriolis force is negligible compared to the pressure gradient and centripetal force in

the gradient wind equation, the RMW is found to be entirely defined by  $A$  and  $B$ , independent of the central pressure deficit and the maximum wind. It is logical to speculate that the cyclostrophic assumption is only reasonable when the Rossby number ( $R_o$ , which is a dimensionless number relating the ratio of nonlinear accelerations to the Coriolis force) at the RMW is large (details given in section 2.2.2). A great feature of the HM is that both  $A$  and  $B$ , as well as the RMW if it is absent from model inputs, can be readily derived from a limited set of wind observations, or determined climatologically for a standard hurricane. This feature is extremely useful when the RMW is not available at the time of forecasting. For example, in the event of a TC, the National Hurricane Center (NHC) issues forecast advisories every six hours to update the current and future (forecasts made for 12, 24, 36, and 72 hours from the current synoptic time) storm location, the central pressure, the observed maximum sustained wind, the radii to the specified 34-, 50-, and 64-kt storm isotachs in each of the NorthEast (NE), SoutEast (SE), SouthWest (SW), and NorthWest (NW) storm quadrants, etc. Based on the radius to a specified isotach in one quadrant, the RMW can be solved by fitting the isotach data to the HM's wind profile via a root-finding algorithm. The HM uses an azimuthally constant RMW to construct its axis-symmetrical wind field. Given their simplicity and reasonable forecasting skill, the HM and its variants have been used extensively for operational forecasting of TC winds over the past few decades.

Willoughby and Rahn (2004) evaluated the HM by comparing the statistically fitted HM profiles with wind observations measured by the Hurricane Research Division (HRD) aircraft, and concluded that the HM suffers from two systematic errors: 1) The areas of strong winds in the eyewall and of nearly calm winds at the vortex center are too wide, and 2) the wind decreases too rapidly with distance from the maximum wind, both inside and outside the eye. To address

these issues, Willoughby et al. (2006, WM) proposed a new family of sectionally continuous profiles that allow the wind to increase in proportion to a power of radius inside the eye and decay exponentially outside the eye with a smooth transition in between. Unlike the HM, which is a pressure-wind relationship model, the WM calculates the geopotential height of a given pressure through an outward integration of the gradient wind acceleration. The storm parameters featured in the WM, including the exponent for the power law inside the eye, and a single- (dual-) exponential decay length(s) outside the eye, were derived using least square fits based on a sample of 493 observed profiles, and accurate estimation of these parameters require ample wind data both inside and outside the storm eye. The WM's wind profile was shown to fit historical wind observations more accurately. However, in the event of a TC when only limited storm information is available at the time of forecasting, statistically fitted parameters from historical TC events might not lead to an optimum fit to each individual storm.

Since the 1980s, extensive reconnaissance aircraft data have become more widely available due to the advantage of modern technology. The extended dataset led Holland et al. (2010, hereafter HM10) develop a revised version to the classic HM by: 1) allowing a linearly varying exponent in the wind equation to better fit inner and outer wind observations made at any level; and 2) adding a secondary wind maxima with specified magnitude and range to the primary winds to accommodate more complex wind profiles. The HM10 showed improvements over the classic HM to achieve better fit to the hurricane reconnaissance data for a range of North Atlantic hurricanes. However, its application in real TC cases requires an accurate estimate of the RMW as input during the time of forecasting, which might not be available, at least in the NHC's forecast advisories.



Another attempt was made by Wood et al. (2013, hereafter WW13) to extend the existing tangential wind model of Wood and White (2011) and tailor it for TC application. The WW13 proposed a partitioned TC wind profile that was able to render as many as three wind maxima during an Eye Replacement Cycle (ERC). It features five key storm parameters in each of its primary, secondary, and tertiary tangential wind formulations: the RMW, the maximum wind, and three shape parameters including the growth parameter  $\kappa$ , and the decay parameter  $\eta$ , and the size parameter  $\lambda$ . Each intuitive shape parameter has its unique physical meaning and acts independently in controlling different portions of the wind profile. In the WW13, the gradient wind is readily derived from the cyclostrophic wind in terms of the cyclostrophic Rossby number  $Ro_C$ , and the total pressure profile is partitioned into different components corresponded with the multi-maxima wind profile, calculated via cyclostrophic balance. It was noted that the WW13 was optimized to define a relatively peaked TC with a large  $Ro_C$  that typically ranging from 10 to 100 (Willoughby, 1990; Willoughby and Rahn, 2004). For a TC with a relatively broad profile and  $Ro_C$  less than 10, the RMW was often found to be displaced towards the TC center, and both the RMW and the maximum wind needed to be mathematically adjusted. The WW13 showed sophistication in obtaining optimum fit to known radial profiles, but it also requires an accurate estimate of the RMW as input data to accomplish that, which may render it inconvenient for operational forecasting.

Naturally, there is considerable variability in the estimated surface wind fields constructed with different parametric wind models. Up until now, there is not much consensus on which model is better than the others considering different aspects and the available datasets being used in each scenario. Although the HM suffers from systematic errors as discussed earlier, its simple formulation, and most importantly, its relaxation on requiring an accurate

RMW as input data allow the HM to be widely used for operational forecasting. Based on the HM, Xie et al. (2006) developed a real-time hurricane surface wind forecasting system that is characterized by an azimuthally-varying RMW for better depicting surface wind structure of an asymmetric TC such as a land falling hurricane, *a.k.a.* the asymmetric Holland model (AHM). Using radii to the highest isotach (34, 50, or 64 kt) in each of the 4 storm quadrants, the RMW is calculated in each quadrant and then fitted azimuthally around the storm center via a polynomial interpolation.

Mattocks et al. (2006) implemented Xie's work in the ADCIRC model (Luettich, Westerink, and Scheffner, 1991; Westerink et al., 1992) and uses the coupled model for real-time storm surge and wave forecasting for the state of North Carolina. This operational system has many advantages: 1) it allows an ocean simulation to be launched as soon as an NHC forecast advisory is issued, usually hours before other numerical wind products become available, 2) a synthetic wind field is computed on the fly at each time step during the entire simulation period, and 3) by varying storm parameters, such as storm track or storm forwarding speed, a series of ensemble members of forecasts for strategic assessment of coastal emergencies can be provided. As an improved application of the HM, the AHM works great for intense but relatively narrow TCs with a large  $R_o$ , for which the cyclostrophic assumption made at the RMW is valid. However, for a generally weak but broad TC, or a strong TC at its developing or dissipating stages, the AHM is inferior as the Coriolis force is no longer negligible at the RMW. Cases like these will mostly lead to underestimations of the peak winds, as well as unrealistic wind profiles in the AHM.

The goal of this study was to improve the AHM and to develop a Generalized Asymmetric Holland Vortex Model (GAHM) for general operational purpose. It was expected

that by eliminating the cyclostrophic assumption at the RMW, the GAHM should be able to generate high-quality representative wind fields for a wide range of TCs. Also, a composite wind method should be implemented in the GAHM in order to fully use all multiple storm isotachs in NHC's forecast or "best track" advisories. Detailed descriptions of the GAHM, including derivation of formulae and model implementation, are given in section 2.2. Following that, section 2.3 gives the background of seven recent hurricanes that struck the U.S. East Coast and the Gulf of Mexico, used as study cases. Evaluation of model consistency of the GAHM's formulae were carried out in section 2.4, and in section 2.5 the composite wind method was implemented to look at the overall spatial wind field. Section 2.6 draws the final conclusions and proposes future work for further improvement of the GAHM.

## 2.2 Model Description

### 2.2.1 The classic Holland Model (1980)

As the development of GAHM in this study is based on the classic HM (1980), a brief derivation of HM's formulations is presented below. To start with, the surface pressure profile in HM is approximated by a rectangular hyperbolic equation and is given as

$$P(r) = P_c + (P_n - P_c)e^{-A/r^B}, \quad (2.1)$$

where  $P$  is the pressure at radius  $r$ ,  $P_c$  is the central pressure,  $P_n$  is the ambient pressure,  $A$  and  $B$  are scaling parameters that can be estimated empirically from observations.

Substituting (2.1) into the gradient wind equation yields an equation for the gradient wind profile:

$$V_{g(r)} = \sqrt{AB(P_n - P_c)e^{-A/r^B}/\rho r^B + \left(\frac{rf}{2}\right)^2 - \left(\frac{rf}{2}\right)}, \quad (2.2)$$

where  $V_g$  is the gradient wind at radius  $r$ ,  $e$  is the base of natural logarithm,  $\rho$  is the density of air,  $f$  is the Coriolis term,  $f = 2\omega \sin(\text{latitude})$ , and  $\omega$  is the rotational frequency of the earth. Under the assumption that the Coriolis force is negligible compared to the centrifugal force in the region of maximum winds, the cyclostrophic wind is

$$V_c(r) = \sqrt{AB(P_n - P_c)e^{-A/r^B}/\rho r^B}. \quad (2.3)$$

By setting  $dV_c/dr = 0$  at  $r = R_{max}$ , it is obtained that

$$A = R_{max}^B. \quad (2.4)$$

The RMW is defined solely by the scaling parameters  $A$  and  $B$ , and is irrelevant to the relative value of ambient and central pressure. Substituting (2.4) back into (2.3) yields an estimation of  $B$  as a function of the maximum wind speed  $V_{max}$  and the central pressure drop, given by

$$B = V_{max}^2 \rho e / (P_n - P_c). \quad (2.5)$$

It was reasoned by Holland that a plausible ranges of  $B$  would be between 1 and 2.5 to limit the shape and size of the vortex. Based on (2.4) and (2.5), re-organizing the pressure and wind equations gives the final pressure and wind profiles

$$P = P_c + (P_n - P_c)e^{-(R_{max}/r)^B}, \text{ and} \quad (2.6)$$

$$V_g = \sqrt{V_{max}^2 e^{(1-(R_{max}/r)^B)} (R_{max}/r)^B + \left(\frac{rf}{2}\right)^2 - \left(\frac{rf}{2}\right)}. \quad (2.7)$$

Attempts were made to fit wind observations to the surface wind profile using (2.7), however, discrepancies between observed and modeled winds were found negatively correlated to the Rossby number at the RMW

$$R_o = \frac{\text{Nonlinear Acceleration}}{\text{Coriolis force}} \sim \frac{V_{max}^2/R_{max}}{V_{max}f} = \frac{V_{max}}{R_{max}f}. \quad (2.8)$$

The larger the  $R_o$ , the smaller the discrepancies (more discussions will be given later). By definition, a large  $R_o$  ( $\approx 10^3$ ) specifies a system in cyclostrophic balance that is dominated by inertial and centrifugal forces with negligible Coriolis force, such as a tornado or the inner core of an intense hurricane, while a small value ( $\approx 10^{-2} \sim 10^2$ ) signifies a system in geostrophic balance that is strongly influenced by the Coriolis force, such as the outer region of a TC. Thus, the cyclostrophic balance assumption made in the HM is valid for describing an intense but narrow TC with a large  $R_o$ , but not suitable for a weak but broad TC with a small  $R_o$ . This intrinsic problem of HM calls our attention to develop the GAHM that would consistently work with a wide range of TCs, and theoretically this could be accomplished by eliminating the assumption of the cyclostrophic balance at the RMW in the GAHM.

### 2.2.2 Derivation of GAHM's Formulas

Following the HM, the pressure profile in the GAHM is likewise approximated by a rectangular hyperbolic equation, given by (2.1), and the wind profile is obtained by substituting (2.1) into the gradient wind equation, given by (2.2). Without assuming cyclostrophic balance at the RMW, by setting  $dV_g/dr = 0$  at  $r = R_{max}$  in (2.2), the adjusted Holland B parameter, hereafter referred to as  $B_g$ , is derived as

$$\begin{aligned}
B_g &= (V_{max}^2 + V_{max}R_{max}f)\rho e^\varphi / \varphi(P_n - P_c) \\
&= B \frac{(1+1/R_o)e^{\varphi-1}}{\varphi},
\end{aligned} \tag{2.9}$$

where  $\varphi$  is a scaling factor newly introduced, initially defined as

$$\varphi = A/R_{max}^B \text{ (or } A = \varphi R_{max}^B \text{)}, \tag{2.10}$$

and later derived as

$$\begin{aligned}
\varphi &= 1 + V_{max}R_{max}f/B_g (V_{max}^2 + V_{max}R_{max}f) \\
&= 1 + \frac{1/R_o}{B_g(1+1/R_o)}.
\end{aligned} \tag{2.11}$$

Equation (2.10) indicates that the RMW in the GAHM is not entirely defined by the shape parameters  $A$  and  $B$  as in the HM, but also by a scaling factor  $\varphi$ . Closed forms of expression for  $B_g$  and  $\varphi$  are not given in this study, instead, their numerical solutions can be calculated by solving (2.9) and (2.11) iteratively in the model. Intuitively, the values of  $B_g/B$  and  $\varphi$  are always larger than (or in rare cases equal to) 1, depending on the values of  $R_o$  and  $B$ . Figure 2.1 illustrates how the numerically solved  $B_g/B$  and  $\varphi$  vary with  $R_o$  given different  $B$  values. For easier viewing, here  $R_o$  is plotted in base 10 logarithmic scale. It is evident that, both  $B_g/B$  and  $\varphi$  remain close to 1 when  $\log_{10}R_o$  is within the range of  $[1, 2]$ , but  $B_g/B$  increases dramatically when  $\log_{10}R_o$  drops below 1 and almost doubles at  $\log_{10}R_o = 0$ . Rate of change of  $B_g/B$  with respect to  $\log_{10}R_o$  is slightly larger for a smaller  $B$ , which is also true for  $\varphi$ .

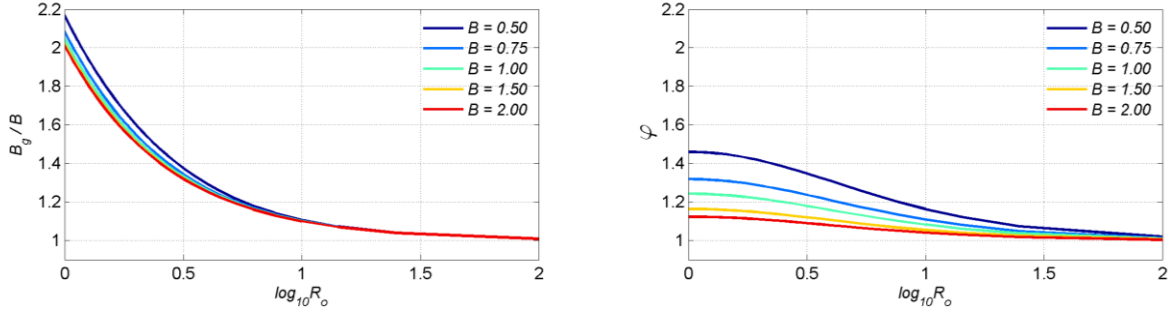


Figure 2.1. Profiles of  $B_g/B$  (left panel) and  $\varphi$  (right panel) with respect to  $\log_{10} R_o$ , given different  $B$  values as shown in different colors.

Substitute (2.9) & (2.11) into (2.1) and (2.2) yields the final equations for GAHM's pressure and wind profiles

$$P = P_c + (P_n - P_c)e^{-\varphi(R_{max}/r)^{B_g}}, \text{ and} \quad (2.12)$$

$$V_g = \sqrt{V_{max}^2(1 + 1/R_o)e^{\varphi(1-(R_{max}/r)^{B_g})}(R_{max}/r)^{B_g} + \left(\frac{rf}{2}\right)^2 - \left(\frac{rf}{2}\right)}. \quad (2.13)$$

Influence of the Coriolis force on the shape of the radial pressure and wind profiles are evidenced by the presence of  $R_o$  and  $\varphi$  in (2.12) and (2.13). A special scenario is when we set  $f = 0$ , which corresponds to an infinitely large  $R_o$ , the GAHM then reduces to the HM. Otherwise, for TCs with a relatively small  $R_o$ , the influence of the Coriolis force on the pressure and wind structures should and can only be addressed by the GAHM. It meets our expectation that GAHM's solution approaches to that of HM's when the influence of Coriolis force is small, but departs from it when the Coriolis force plays an important role in the system. The above reasoning can be demonstrated by Figure 2.2, which shows the normalized gradient wind profiles of the HM (left panel) and the GAHM (right panel) as functions of the normalized radial distances, the Holland  $B$  parameter, and  $R_o$ . In each panel, each layer represents the normalized gradient winds corresponding to a different Holland  $B$  value. Ideally, the line of intersection (shown by the black line in each panel) between all the layers and the plane of  $r/R_{max} = 1$

should be on the plane of  $V_g/V_{max} = 1$ , no matter what the value of  $R_o$ . However, the black line formed in the HM in the left panel deviates from the plane of  $V_g/V_{max} = 1$  as  $\log_{10} R_o$  decreases from 2 to close to 0 ( $R_o$  decreases from 100 to 1), while the black line formed in the GAHM in the right panel maintains constantly on the plane of  $V_g/V_{max} = 1$  regardless of how  $R_o$  changes.

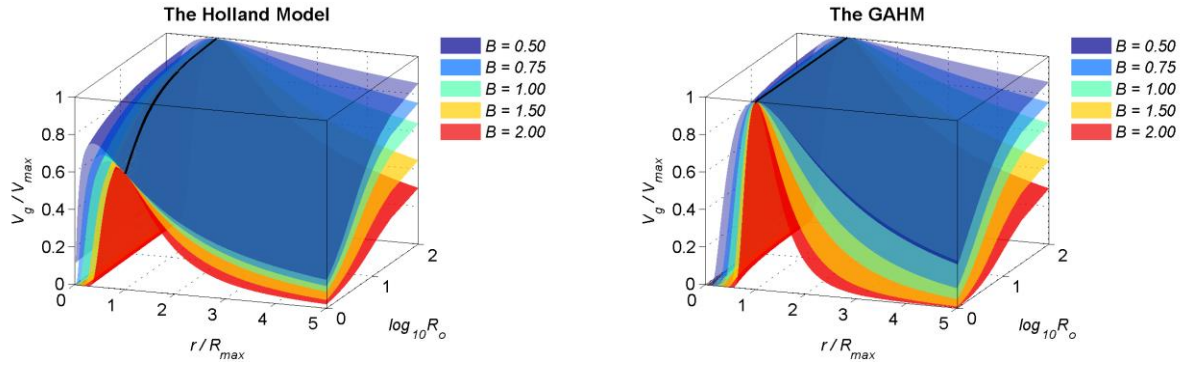


Figure 2.2. The normalized gradient wind profiles of the HM (left panel) and the GAHM (right panel) as functions of the normalized radial distances and  $R_o$ , given different Holland  $B$  values.

To have a dissective look of the results shown in Figure 2.2, slices drawn perpendicular to the axis of  $\log_{10} R_o$  at three selected values 0, 1.0, and 2.0, are shown in Figure 2.3. It is well noted that the GAHM performs consistently well in obtaining  $V_g = V_{max}$  at  $r = R_{max}$ , regardless of how  $R_o$  changes. On the other hand, the HM tends to generate distorted wind profiles with the maximum winds skewed inward towards the storm center and underestimated, yielding faulty results of the modeled maximum wind and the RMW. Specifically, underestimation in modeled maximum wind is clear (more than 10%) when  $\log_{10} R_o < 1$ , and misrepresentation of the RMW is larger for a smaller  $B$ . As a result, when both models are applied in real cases, the GAHM is analytically more precise than the HM and can ensure a better match between the observed and the modeled winds. This indicates that assuming the storm information in the NHC's forecast or "best track" advisories is accurate, GAHM is a more reliable and consistent model for operational forecasting purposes.



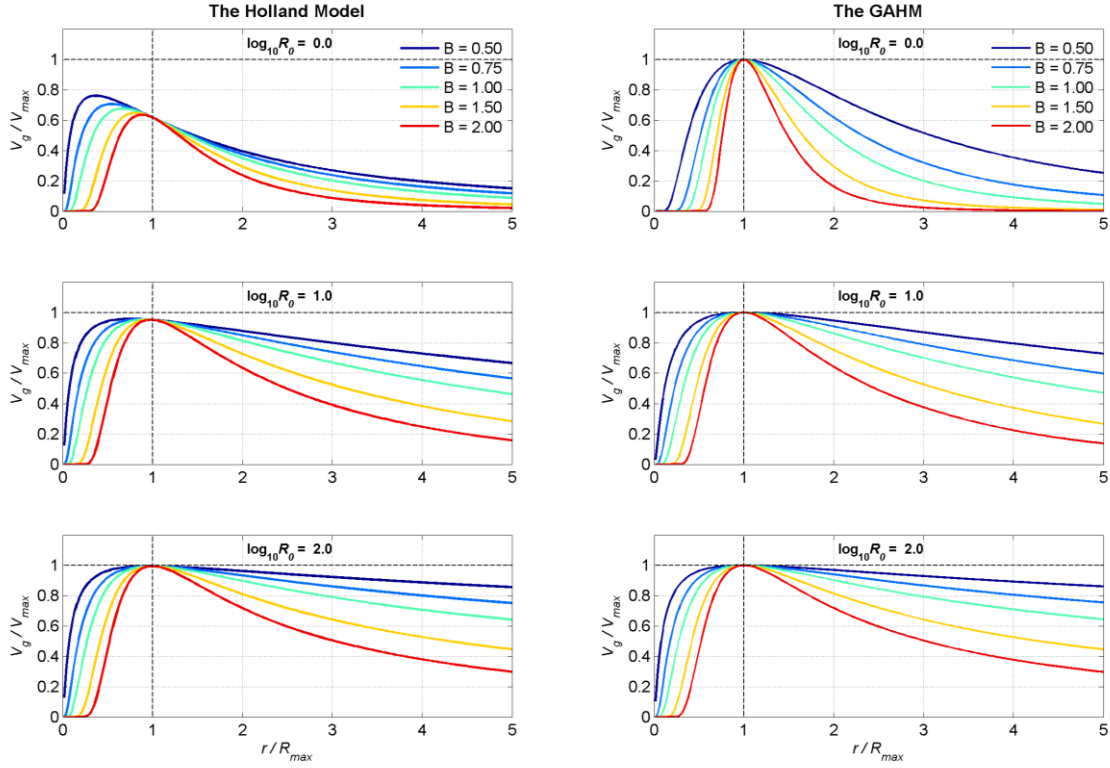


Figure 2.3. Slices of the normalized gradient wind profiles (as shown in Figure 2.2) at  $\log_{10} R_o = 0, 1, \text{ and } 2$  (or correspondingly  $R_o = 1, 10, \text{ and } 100$ ).

### 2.2.3 Calculation of the Spatially Varying RMW

The gradient wind equation describes a three-way balance between the pressure gradient, the centrifugal, and the Coriolis forces of a vortex above the influence of the planetary boundary layer, where the atmospheric flow decouples from surface friction (Powell et al., 2009). With estimated  $B_g$  and the RMW, (2.12) and (2.13) give the radial pressure and wind profiles of a vortex at the same gradient wind level. When adjusting the gradient wind speeds to the standard surface reference level over the ocean of 10m MSL (mean sea level), the boundary layer effect must be considered, including the scalar reduction in wind speed, wind inflow towards the center of the vortex due to frictions, and asymmetry of TC surface wind structure due to the storm forward motion, etc.

As a standard procedure, the quadrant-varying  $B_g$  and the RMW are pre-computed in the ASWIP program (an external FORTRAN program initially written by Flemming et al and further developed in this study to accommodate the GAHM) prior to running an ADCIRC simulation forced with the GAHM wind model. First, the maximum sustained wind and the winds of 34-, 50-, and 64-kt isotachs in NHC's forecast or "best track" advisories, normally reported at 10m height, must be corrected to the gradient wind level to remove the influence of the boundary layer effect. Practically, the maximum gradient wind is calculated as

$$V_{max} = \frac{(V_M - \gamma V_T)}{W_{rf}}, \quad (2.14)$$

where  $V_M$  is the reported maximum sustained wind speed at the 10m level,  $V_T$  is the storm translational speed calculated from successive storm center locations,  $\gamma$  is the damp factor for  $V_T$ , and  $W_{rf}$  is the wind reduction factor for reducing wind speed from the gradient wind level to the surface (Powell et al. 2003). There are several forms of  $\gamma$  exist in the literature, while in this study, the following form was employed

$$\gamma = \frac{V_g}{V_{max}}, \quad (2.15)$$

which is the ratio of gradient wind to the maximum wind along a radial profile. Thus,  $\gamma$  is zero at storm center, increases to a maximum of 1 at the RMW (where  $V_g = V_{max}$ ), and gradually decreases outward to zero. Due to vertical stability differences, variability over the range of 0.7 to 0.9 for  $W_{rf}$  is considered to be reasonable, and a constant 0.9 is applied in this study. The gradient wind at the radius to a specified isotach in each storm quadrant can be obtained by

$$V_r = |\overrightarrow{V_{r\_inflow}}| = \frac{|\overrightarrow{V_{isot}} - \gamma \overrightarrow{V_T}|}{W_{rf}}, \quad (2.16)$$

where  $\overrightarrow{V_{isot}}$  is the isotach wind at the surface with an unknown angle  $\varepsilon$ , and  $\overrightarrow{V_{r\_inflow}}$  is the temporary gradient wind with an inward rotation  $\beta$ , whose magnitude is the same as the final gradient wind of the vortex. Re-writing (2.16) in both x- and y-components yields:

$$V_r \cos(\text{angle}(i) + 90 + \beta) = V_{isot} \cos(\varepsilon) - \gamma u_T \quad (2.17)$$

$$V_r \sin(\text{angle}(i) + 90 + \beta) = V_{isot} \sin(\varepsilon) - \gamma v_T \quad (2.18)$$

where  $\text{angle}(i)$  is the azimuth angle for each of the NE, SE, SW and NW storm quadrants, given by  $45^\circ$ ,  $135^\circ$ ,  $225^\circ$  and  $315^\circ$ ,  $V_{isot} \cos(\varepsilon)$  and  $V_{isot} \sin(\varepsilon)$  are the zonal and meridional components of  $\overrightarrow{V_{isot}}$ , and  $u_T$  and  $v_T$  are the zonal and meridional components of  $\overrightarrow{V_T}$ . The cross-isobar frictional inflow angle  $\beta$  is taken to be approximately  $25^\circ$  at the outer region, but decreases to zero near the storm center. The following, as described in the Queensland Government's Ocean Hazards Assessment (2001), is adopted to calculate  $\beta$  in this study:

$$\beta = \begin{cases} 10^\circ & r < R_{max} \\ 10^\circ + 75(r - R_{max})/R_{max} & R_{max} < r < 1.2 R_{max} \\ 25^\circ & r > 1.2 R_{max} \end{cases} \quad (2.19)$$

Given an initial guess of the RMW,  $V_r$  can be calculated for each storm quadrant of a specified isotach by combining (2.15), (2.17), (2.18) and (2.19). Then, the values of  $B_g$  and  $\varphi$  can be obtained by substituting  $V_{max}$  and  $V_r$  into (2.9) and (2.11), and solving the coupled equations iteratively until both variables converge. Plugging  $B_g$ ,  $\varphi$ ,  $r$ ,  $V_{max}$  and  $V_r$  back into (2.13), the RMW can be inversely solved by a root-finding algorithm. It should be noted that the calculated RMW is based on an initial estimate of it at the beginning of this process. To get a converged solution, the entire RMW-solving process needs to be repeated, each time using the latest solved RMW until it finally converges. In cases where multiple isotachs are available, the RMW calculated from the highest isotach (physically, only one RMW exist along a radial wind profile

for a simple hurricane vortex) will be used as the pseudo RMW for each lower isotach to set the initial value, and no repetition is needed for the calculated RMW. This procedure ensures that the RMW from the highest isotach is used across all isotachs to keep the cross-isobar frictional inflow angle spatially smooth. Occasionally, we have to deal with situations where  $V_{max} < V_r$  after subtracting the storm translation speed from maximum sustained wind and storm isotach, which usually happens on the right hand side (in the Northern Atmosphere) of a relatively weak fast-moving TC. In this case, we assign  $V_{max} = V_r$ , which is equivalent to setting the RMW equal to the radius to the isotach.

After all calculations are done, the ASWIP program writes the quadrant-varying RMW,  $B_g$  and  $V_{max}$  in addition to the original input data, into a new file in ATCF format, and this file will be used as the single meteorological input file in an ADCIRC simulation.

#### **2.2.4 A Linearly-weighted Composite Wind Method**

During a storm surge simulation run, construction of GAHM's pressure and wind fields is carried out in the ADCIRC model on the fly. Previous studies show that a single vortex generated by parametric wind models might not be able to represent the complex structure of a TC, and the AHM falls into this category since it uses storm information of the highest isotach only. To take advantage of all available isotachs in NHC's forecast or "best track" advisories, an additional feature was added to the GAHM. The GAHM uses a composite wind method to interpolate storm parameters calculated along four quadrant lines onto the entire ADCIRC grid. Given the longitude and latitude of the storm center at time  $t$ , the relative location of a grid node to the vortex center is calculated, specified by azimuth angle  $\theta$  and distance  $d$ . The angle  $\theta$  places the node between two adjacent quadrant lines  $i$  and  $i + 1$ , where  $angle(i) < \theta \leq angle(i + 1)$ . For each storm parameter, including the RMW, the  $B_g$  and  $V_{max}$ , its composite

value at  $(\theta, d)$  are weighted between a pair of pseudo values at  $(angle(i), d)$  and  $(angle(i + 1), d)$ :

$$P_{composite} = \frac{P_{pseudo1}(90-\theta)^2 + P_{pseudo2}\theta^2}{(90-\theta)^2 + \theta^2}. \quad (2.20)$$

The  $P_{pseudo1}$  and  $P_{pseudo2}$  are the pseudo values for a parameter interpolated at distance  $d$  on quadrant lines  $i$  and  $i + 1$  using an inverse distance weighting (IDW) method:

$$P_{pseudo} = f_{34}P_{34} + f_{50}P_{50} + f_{64}P_{64}, \quad (2.21)$$

where  $P_{34}$ ,  $P_{50}$  and  $P_{64}$  are parameter values calculated from the 34, 50 and 64 kt isotachs,  $f_{64}$ ,  $f_{50}$  and  $f_{34}$ , are weighting factors for each isotach, and  $f_{64} + f_{50} + f_{34} = 1$ . The weighting factors are calculated by comparing distance  $d$  with distances to each of the 34, 50 and 64 kt isotachs:

$$\begin{aligned} \text{I. } r < R_{64} & \quad f_{64} = 1, f_{50} = 0, f_{34} = 0 \\ \text{II. } R_{64} \leq r < R_{50} & \quad f_{64} = (r - R_{64}) / (R_{50} - R_{64}), f_{50} = (R_{50} - r) / (R_{50} - R_{64}), f_{34} = 0 \\ \text{III. } R_{50} \leq r < R_{34} & \quad f_{64} = 0, f_{50} = (r - R_{50}) / (R_{34} - R_{50}), f_{34} = (R_{34} - r) / (R_{34} - R_{50}) \\ \text{IV. } r \geq R_{34} & \quad f_{64} = 0, f_{50} = 0, f_{34} = 1 \end{aligned} \quad (2.22)$$

After RMW,  $B_g$  and  $V_{max}$  are interpolated at  $(\theta, d)$ , the scaling factor  $\varphi$  can be calculated via (2.11), and the pressure and gradient wind at the node  $i$  can be calculated from (2.12) and (2.13). The above procedures are performed at each single node of an ADCIRC grid.

Once the pressure and gradient wind fields are calculated at the gradient wind level, they are reduced to the standard 10m reference level to reflect the influence of the boundary layer effect: first, the wind reduction factor  $W_{rf}$  is applied to reduce the magnitude of the scalar wind; then the tangential winds are rotated by an inward flow angle  $\beta$  according to (2.19); and last, the storm translational speed  $\gamma \overrightarrow{V_T}$  is added to the vortex winds. This new composite wind method is simple and efficient, and more importantly, it assures that the constructed surface wind field is

fully consistent with all available wind isotachs provided in NHC’s forecast or “best track” advisories during the life cycle of a TC. Evaluation of this composite method will be conducted in Section 2.5. To use the resulted wind fields as surface wind forcing in ADCIRC, a wind averaging factor should be applied to convert 1-min to 10-min winds.

## 2.3 Study Cases

Evaluation of the GAHM in this study was carried out based on seven selected Hurricanes that struck the Gulf of Mexico and the Eastern United States in the past: Katrina (2005), Rita (2005), Gustav (2008), Ike (2008), Irene (2011), Isaac (2012), and Sandy (2012). Ranging from category 1 to 5 on the Saffir-Simpson Hurricane Wind Scale, these storms vary in storm track, forward motion, size, intensity, duration, and etc., but each caused severe damages to the coastal states due to the destructive winds, wind-induced storm surges, and ocean waves. The “best track” file for each storm, which contains all necessary data and sometimes with additional/revised storm information in the forecast advisories, was retrieved from NHC’s ftp site (<ftp://ftp.nhc.noaa.gov/atcf>; previous years’ data are located in the *archive* directory) and used as model input. Each “best track” file contains the time-series estimates of the latitude and longitude of the storm center, the 1-min maximum sustained surface wind, minimum sea-level pressure, radii to the 34-, 50- and/or 64-kt Isotachs in 4 storm quadrants, the observed radius to the maximum wind (RMW), etc., at 6-hour interval. Since both the GAHM and AHM require a radially-varying RMW to construct the surface pressure and wind fields, the “best track” RMW will not be used as input, but solely for model validation purpose in the next two sections.

Table 2.1 Meteorological details of seven recent hurricanes listed in chronological order

<i>Hurricane</i>	<i>Saffir-Simpson Wind Scale</i>	<i>Maximum Sustained Wind (knot)</i>	<i>Minimum Central Pressure (mbar)</i>	<i>Period from Formation to Dissipation</i>
<i>Katrina</i>	5	150	902	08/23 – 08/30, 2005
<i>Rita</i>	5	155	895	09/18 – 09/26, 2005
<i>Gustav</i>	4	135	941	08/23 – 09/04, 2008
<i>Ike</i>	4	125	935	09/01 – 09/14, 2008
<i>Irene</i>	3	105	942	08/21 – 08/30, 2011
<i>Isaac</i>	1	70	965	08/21 – 09/03, 2012
<i>Sandy</i>	3	95	940	10/22 – 10/01, 2012

Meteorological details of the seven selected hurricanes are given in Table 2.1, and their best tracks are shown in Figure 2.4, with colorbar denoting the maximum sustained wind observed at 6-hour interval. Since both  $B$  and  $R_0$  are used as key parameters in characterizing a TC in this study, their temporal and spatial changes are illustrated in Figure 2.5 and 2.6. Here  $R_0$  is calculated from the GAHM and averaged over 4 quadrants. These three figures demonstrate that when a hurricane goes through different developing stages, not only its maximum sustained wind changes vastly, but also the  $B$  and  $R_0$  values. Typically,  $B$  increases and  $R_0$  decreases as a hurricane strengthens, both within range of (0, 2.5), and vice versa.

Hurricane Irene is a good case to demonstrate the need to develop the GAHM in this study. Irene was a large and destructive hurricane that caused widespread damage to the East Coast of the United States during the late August 2011. It peaked as a Category 3 hurricane with maximum wind speed of 120 mph shortly before hitting the Bahamas, and leveled off in intensity while curving northward. Continuing to weaken, Irene downgraded to a Category 1 hurricane when it made landfall on the Outer Banks of North Carolina on August 27, and later hit New

Jersey and New York City as a tropical cyclone. During its course, Irene brought significant surges to the Mid-Atlantic states through New England, and caused catastrophic inland flooding in New Jersey, Massachusetts and Vermont. As shown in Figure 2.6, for long periods of time at the developing and dissipating stages of Irene, the  $\log_{10}R_o$  drops below 1, which is the boundary value at which the AHM solution begins to deviate from the GAHM.

Evaluation of model performance is given in the next two sections, with section 2.4 focusing on evaluating the consistency of the GAHM's new formulas, and section 2.5 focusing on measuring the efficiency of the composite wind method, both in model consistency and model accuracy. The consistency aspect of model performance can be measured by comparing the modeled maximum winds and winds at the distances to multiple isotachs in 4 storm quadrants with the input NHC's "best track" data. Since GAHM features a set of formulas that were derived from the full gradient wind equation, it is expected that GAHM winds should match the "best track" data more precisely than the AHM winds do. Assessment of model accuracy can be challenging sometimes due to lack of sufficient flight-level data to depict the "true" wind structure of a hurricane vortex. In this study, the re-analysis H\*Wind and the hindcast OWI winds, which are considered to be among the best estimates of hurricane surface wind fields, were used as reference winds for comparison purposes. We also compared the SLOSH winds to the analyzed winds as an additional case.



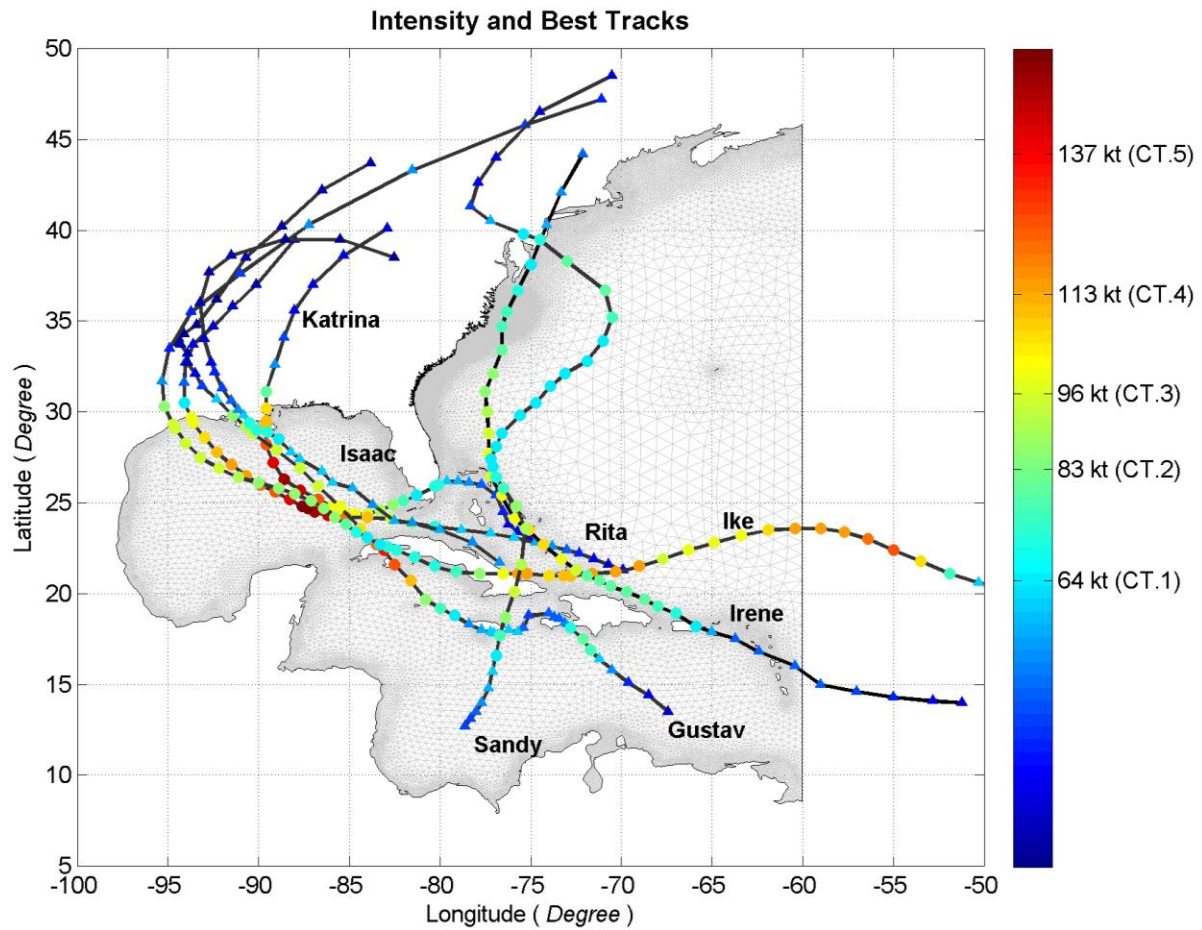


Figure 2.4. Best tracks and Intensity of seven selected Hurricanes used in this study. Black lines represent hurricane best tracks, and dots represent data entries with 6-hour intervals (occasionally there are exceptions), colored by the maximum sustained wind

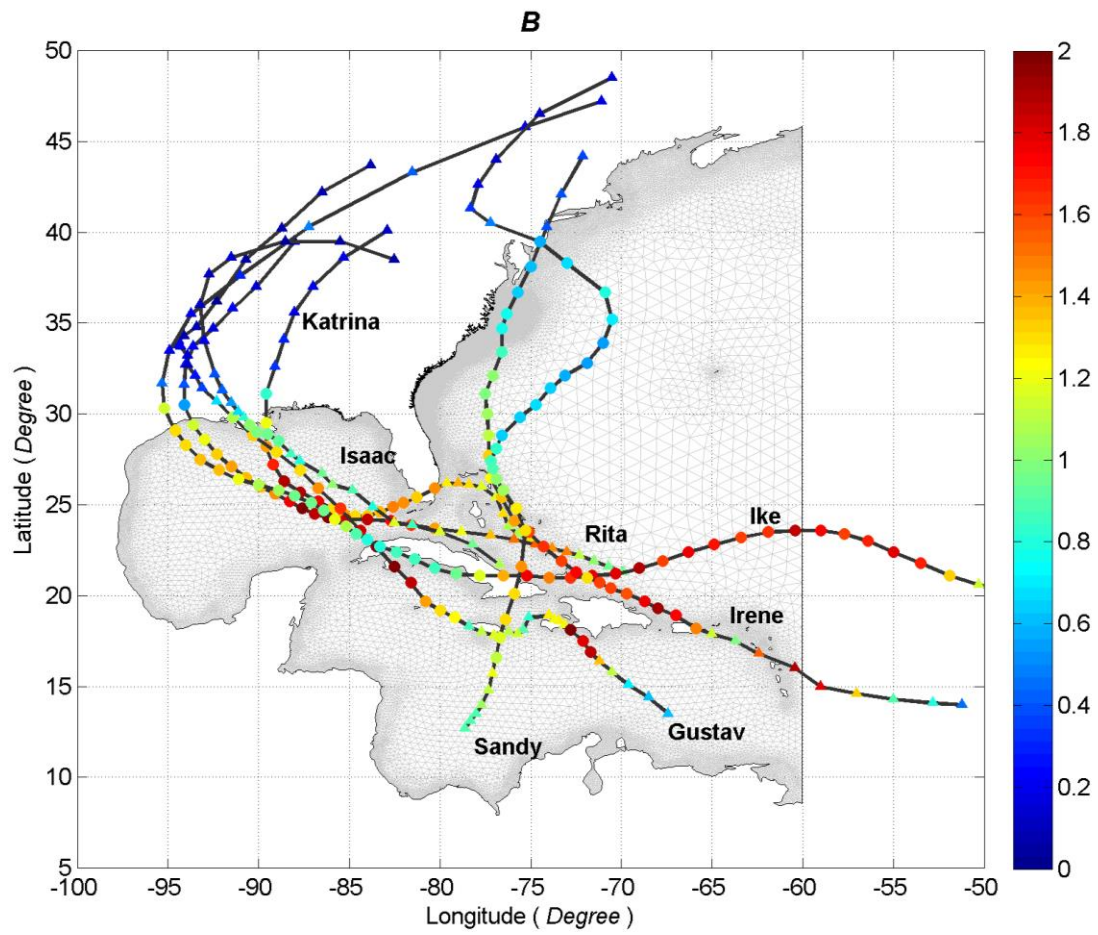


Figure 2.5. Same as Figure 2.4, but dots are colored by Holland  $B$ .

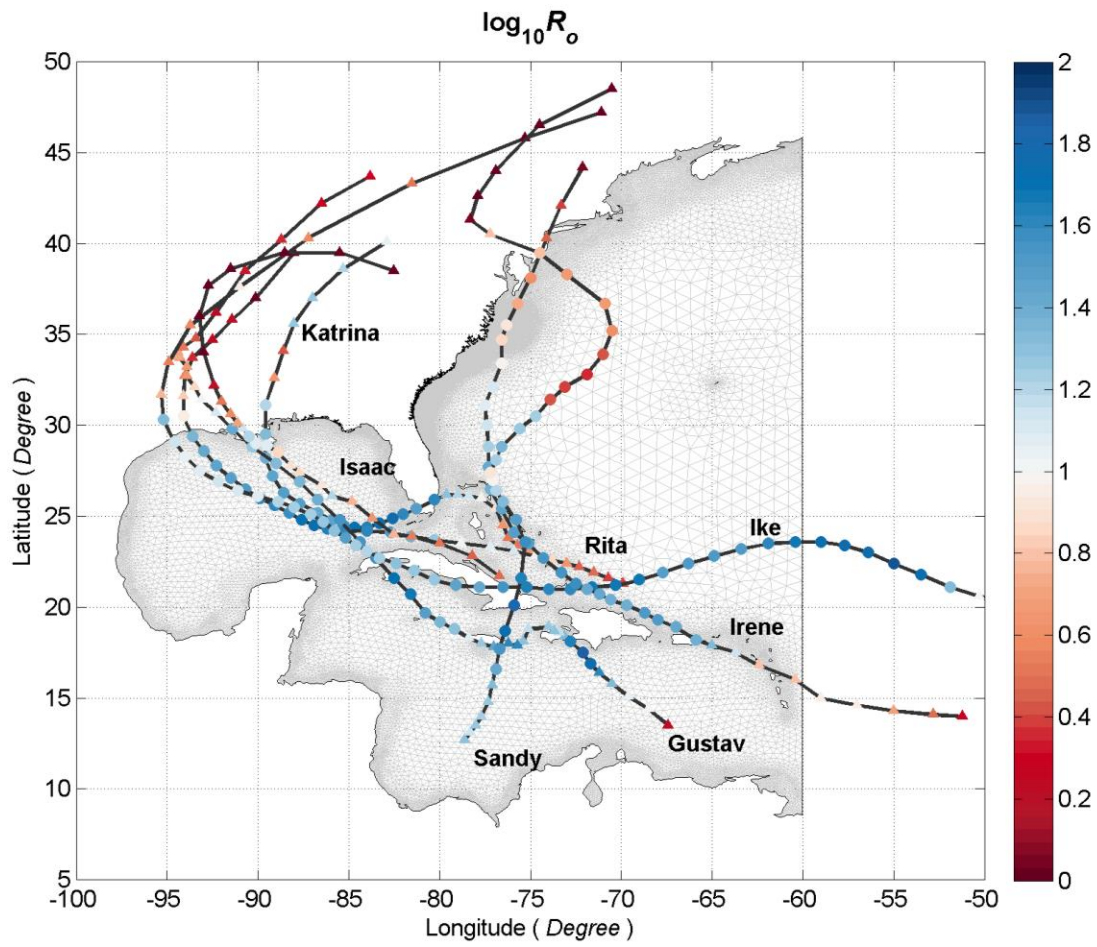


Figure 2.6. Same as Figure 2.4 but dots are colored by  $R_o$  in base 10 logarithmic scale (averaged over four storm quadrants).

## 2.4 Model Results using the Single-Isotach Approach

To evaluate the performance of the GAHM, the single-isotach approach was used when applying the GAHM in real hurricane cases in this section. Using the “best track” file for each selected hurricane, time-series schematic radial wind profiles in 4 storm quadrants (NE, SE, SW and NW), as well as the spatial wind snapshots, were generated using the AHM and the GAHM at the 6-hour interval.

### 2.4.1 Model Consistency at Distances to the Highest Isotach

Figure 2.7 gives three snapshots of the radial wind profiles of Hurricane Irene (2011), at each of its developing, mature and dissipating stages, with a few parameters showing storm characteristics (Table 2.2). The left (right) three panels show cross-section winds from the SW to the NE (the NW to the SE) directions, and all specified isotachs (34, 50, and/or 64-knot) in the “best track” file are plotted in vertical bars at specified distances from the storm center, with the highest one in a dark color and the rest in gray. For a perfect match between the isotachs and the modeled winds, the tip of the vertical bars and the radial profiles must meet at the exact heights.

Table 2.2. Parameters of storm characteristics at three snapshots of Irene (2011)

	<i>2011-Aug-21 18:00</i>				<i>2011-Aug-25 00:00</i>				<i>2011-Aug-28 06:00</i>			
<b>Quadrant</b>	<i>NE</i>	<i>SE</i>	<i>SW</i>	<i>NW</i>	<i>NE</i>	<i>SE</i>	<i>SW</i>	<i>NW</i>	<i>NE</i>	<i>SE</i>	<i>SW</i>	<i>NW</i>
<b><i>B</i></b>	1.00	1.00	1.00	1.00	1.62	1.62	1.62	1.62	0.60	0.60	0.60	0.60
<b><i>B<sub>g</sub></i></b>	1.24	1.03	1.05	1.19	1.69	1.69	1.65	1.68	1.11	0.92	0.72	0.73
<b><i>log<sub>10</sub>R<sub>o</sub></i></b>	0.64	1.44	1.26	0.74	1.37	1.36	1.70	1.41	0.28	0.33	0.74	0.82

Radial wind profiles produced by the GAHM perfectly match the highest isotachs in all quadrants at all time, no matter how  $B$  and  $R_o$  vary, indicating a high model consistency of the GAHM approach. When  $\log_{10}R_o > 1$ , profiles of the AHM generally show good agreement with the highest isotach and are quite similar to those by the GAHM (see the SE and SW quadrants in

the first snapshot), and all four quadrants in the second snapshot. When  $\log_{10} R_o < 1$ , the AHM fails to match any highest isotach due to the issues detailed in section 2.2.1 (see the rest of the quadrants). Note that profiles by either the AHM or the GAHM tend to die off too quickly away from the storm center, and thus fail to match any lower isotach.

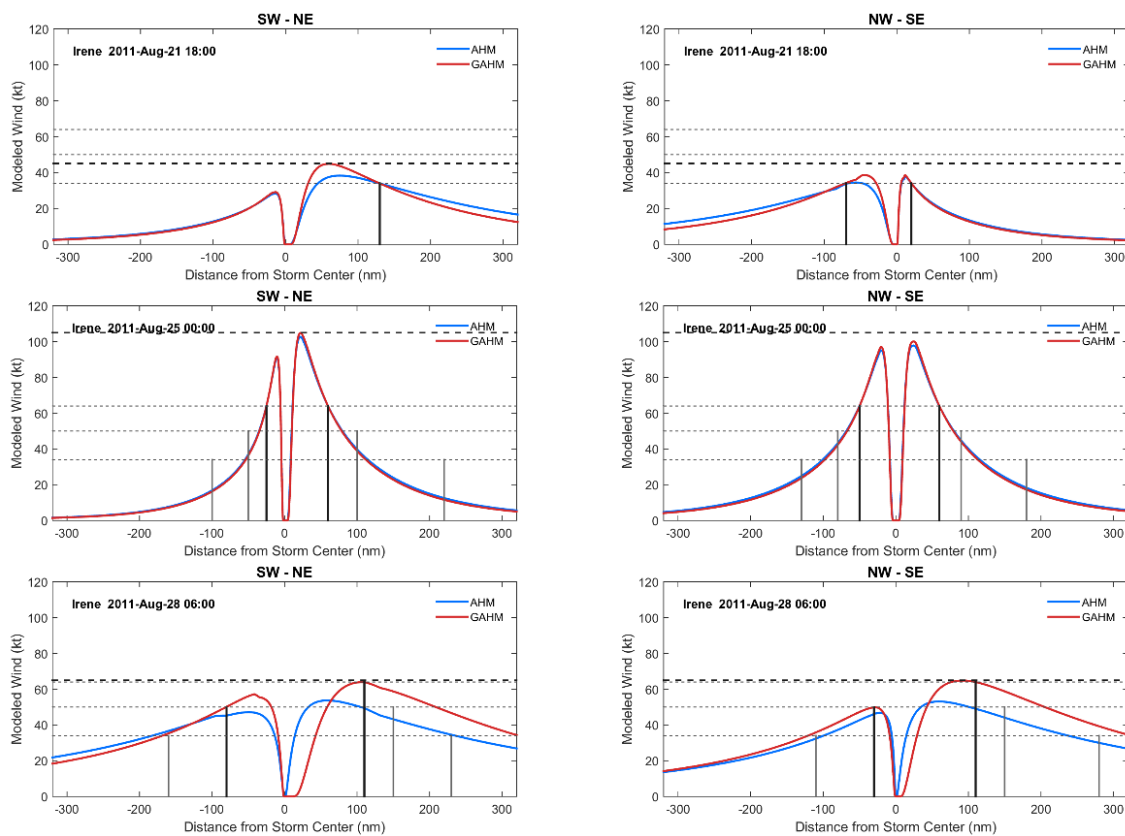


Figure 2.7. Radial wind profiles of Irene (2011) at three different stages. Vertical bars represent the storm isotachs reported in NHC's "best track" file. The highest isotach (utilized) in each quadrant are plotted in black, while lower isotachs (not utilized) are in gray.

### 2.4.2 Evaluation of the RMW and the Modeled Maximum Wind

The time-series maximum wind and the corresponding RMW, which is the distance from storm center to the maximum wind found, were retrieved from the AHM, GAHM spatial wind snapshots for all seven storms. Comparison between the modeled and specified maximum winds in NHC’s “best track” files is shown in the upper two panels of Figure 2.8, with a simple linear regression computed for each panel. The colorbar represents the quadrant-averaged  $R_o$  calculated in the GAHM in base 10 logarithmic scale. Results indicate that the GAHM has an excellent skill in estimating the maximum winds at all times, although overestimation of  $V_M$  can be found near the lower bound of the data. Careful examination of these over-estimates revealed that they were due to bad data entries in the “best track” file. This is particularly common for a weak but fast moving storm, and cautions should be taken when subtracting the storm’s translational speed from the specified maximum wind and isotachs, as the adjusted maximum wind might sometimes be smaller than certain isotach winds in certain quadrants (especially the quadrants with opposing winds to the storm’s forward motion). When such violations occur, the maximum wind will be adjusted accordingly to match the given isotach wind, which is equivalent to setting RMW to the radius to the specified isotach in these violating quadrants. The AHM had larger discrepancies in modeling the maximum wind, especially when  $\log_{10} R_o < 1$  near the lower bound of the data, which is a direct consequence of the cyclostrophic balance assumption made during derivation of AHM’s formula.

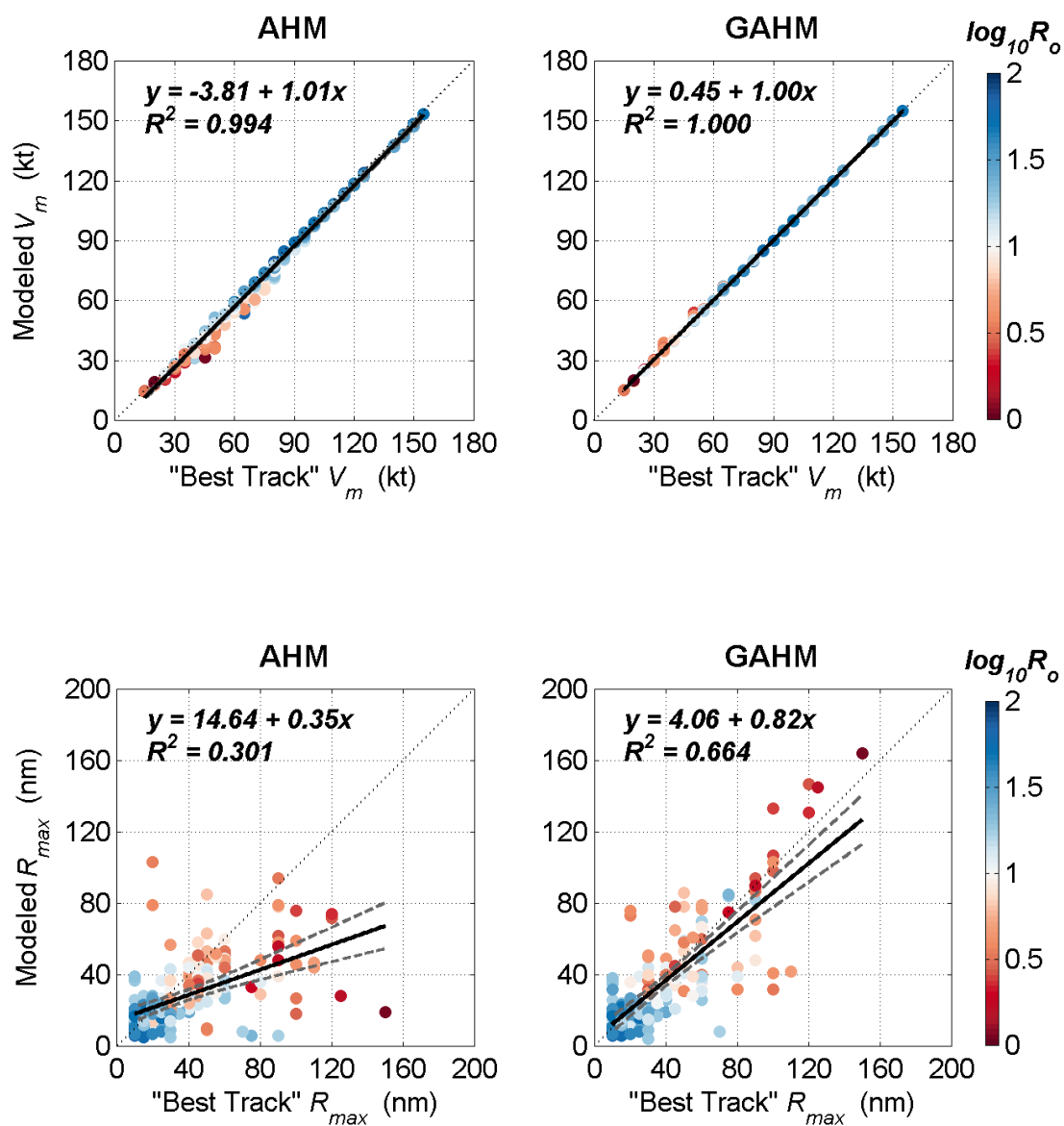


Figure 2.8. Comparison of the modeled and "Best Track"  $V_m$  (upper two panels) and the modeled and "Best Track"  $R_{max}$  (lower two panels) between the AHM and the GAHM based on all seven hurricanes.

## 2.5 Model Results using the Multiple-Isotach Approach

As demonstrated in section 2.4.1, a radial wind profile constructed by the GAHM using the single-isotach approach would only match the highest isotach instead of all isotachs, due to characteristics of the profile and limitations of this single-fitting method. In fact, underestimation of modeled winds at distances to isotachs other than the highest one was common, as the computed wind profile tended to die off too quickly away from the storm center due to the nature of GAHM's formulas. In an effort to minimize the combined error at distances to all available isotachs, and to improve the accuracy of the overall estimated wind field to a further spatial extent, the multiple-isotach approach, which is based on the composite wind method introduced in section 2.2.4, should be used whenever there is more than one isotach present in the best track file.

The 3D snapshot of Irene's radial wind profiles (left) and the interpolated spatial wind field (right) at the corresponding time by the GAHM using the single-isotach approach (upper two panels), and those using the multiple-isotach approach (lower two panels) is given (Figure 2.9). Black contours in the spatial plots denote the 34-, 50, and 64-kt isotachs. The difference in contour shape between the upper and lower spatial plots indicates the difference in these two approaches. By interpolating storm parameters both radially across all available isotachs and azimuthally among 4 storm quadrants using the composite wind method, the multiple-isotach approach allows the GAHM to generate a spatially-continuous composite wind field that consistently fit all specified isotachs in all storm quadrants.



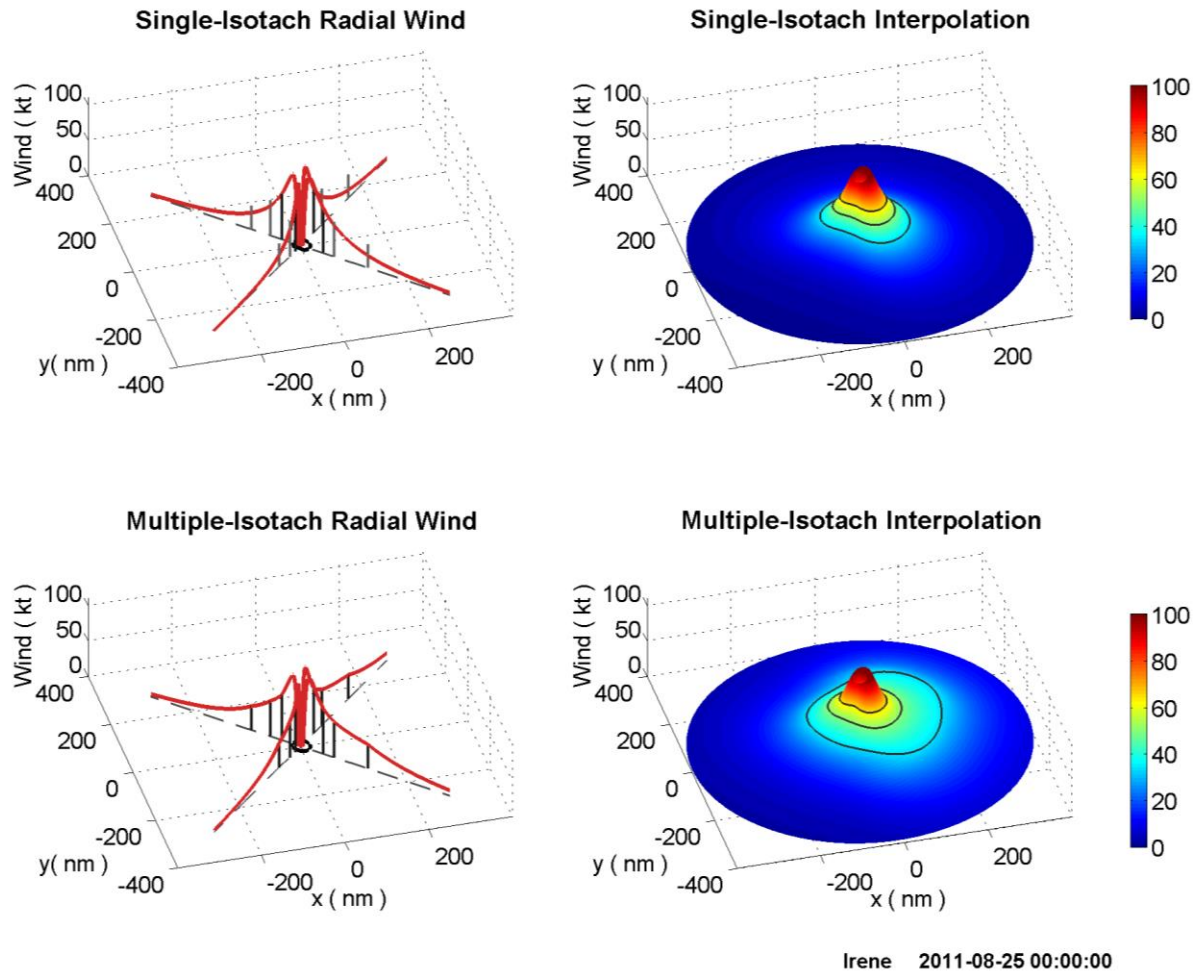


Figure 2.9. Three-dimensional snapshots of Irene’s radial wind profiles (left) and interpolated spatial wind field (right) by the single-isotach approach (upper two panels) and the multiple-isotach approach (lower two panels)

### 2.5.1 Evaluations of Composite Wind Fields

Corresponding to Table 2.2, snapshots of two-dimensional wind fields of Irene by the AHM, the GAHM using the multiple-isotach approach, the SLOSH, the H\*Wind and OWI winds were generated and shown as example in Figure 2.10. In each wind snapshot, the azimuthal RMW surrounding the storm center was calculated from the spatial wind field and shown by the black circle, and the 34-, 50-, and 64-kt isotachs are shown by the gray circles. It was suggested that during weaker periods of a hurricane, the AHM and the GAHM calculate quite different RMWs,

causing them to have quite distinctive spatial wind fields. In general, the calculated RMW in the AHM is closer to the storm center than in the GAHM, due to the cyclostrophic balance assumption made at the RMW in the AHM's formula. However, during stronger periods when there are multiple isotachs available in the "Best Track" file, the GAHM wind fields show similarity with the AHM wind fields in the inner region of the hurricane, but difference in the outer region due to the multiple-isotach approach used in the GAHM to generate its composite wind field. The SLOSH wind fields show a lot of dissimilarity when compared to the AHM and GAHM wind fields, since it uses an azimuthally constant RMW to generate its vortex wind and a distance-weighted translational speed to account for storm asymmetry. Problems arise when vortex winds are much stronger than the translational speed of the hurricane, see SLOSH wind field in the middle row of Figure 11, as the asymmetry could not be rendered properly. There were a lot of details in surface wind fields of the H\*Wind and OWI winds, but the parametric wind fields were rather simple. Although it is unlikely that the parametric winds, constructed over a minimum set of data, will ever match the level of details and complexity in the re-analysis H\*Wind and the numerical OWI winds, however, the ability of a parametric model to produce reasonable estimates of surface wind fields in a timely manner was highly desirable in the field of real-time applications.

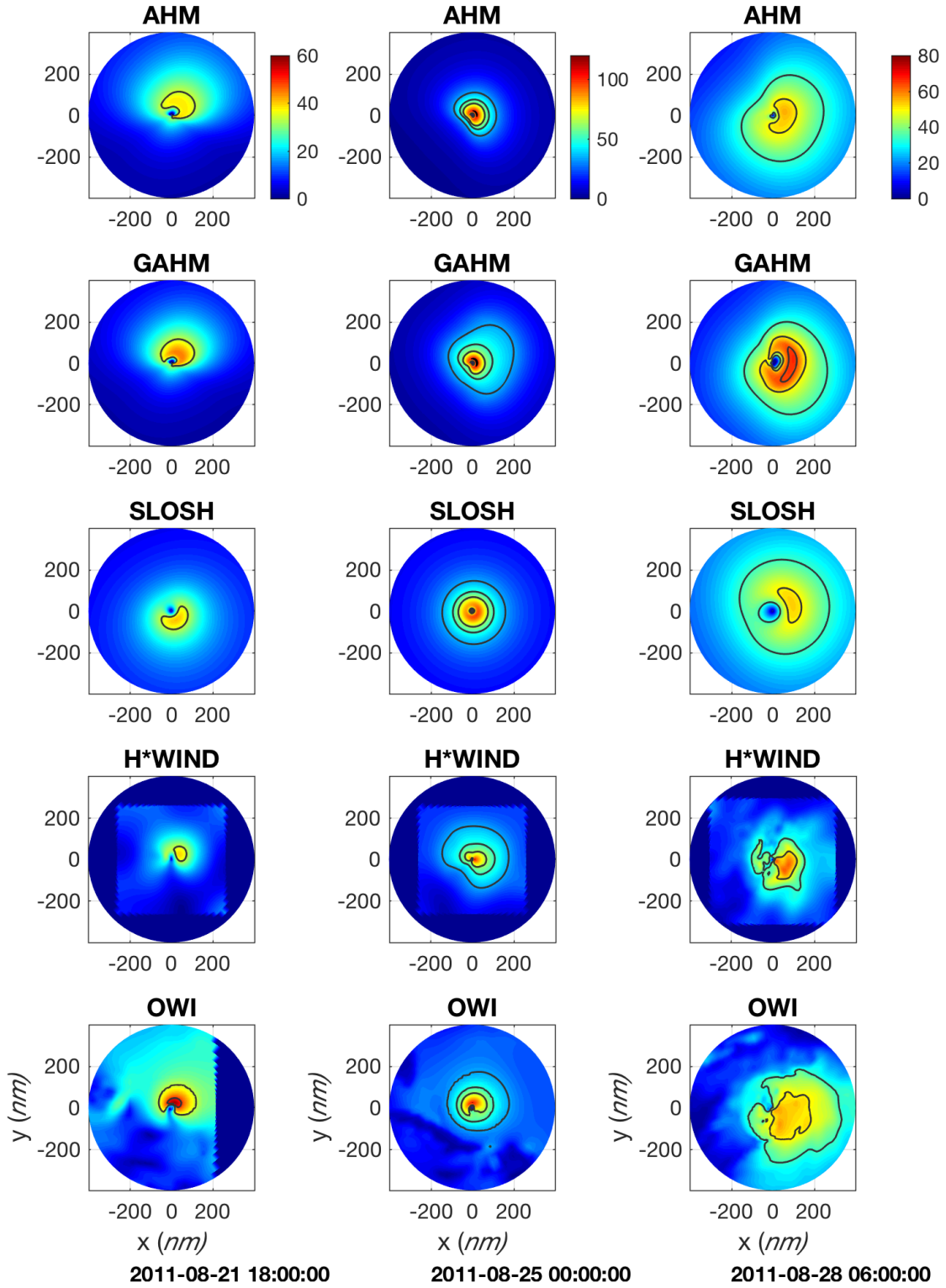


Figure 2.10. Three snapshots (in columns) of Irene's two-dimensional wind fields by the AHM, GAHM, SLOSH, H\*Wind and OWI winds corresponding to Table 2.2

Evaluations of the modeled maximum wind and the RMW are shown in Figure 2.11. The distributions of the maximum winds identified in H\*Wind, OWI winds, or SLOSH winds versus the specified maximum winds were rather dispersed, but the scatters is close to the 1:1 (dash) line, indicating a fairly good correlation, shown in upper panels. It is reasonable that the maximum winds reported in the “best track” advisories, which were approximated by experienced forecasters based on limited information, naturally may not match the maximum winds perfectly in the re-analysis H\*Wind and numerical OWI winds. Since the SLOSH model does not take the maximum winds as model input, the accuracy of its modeled maximum winds was not ideal here.

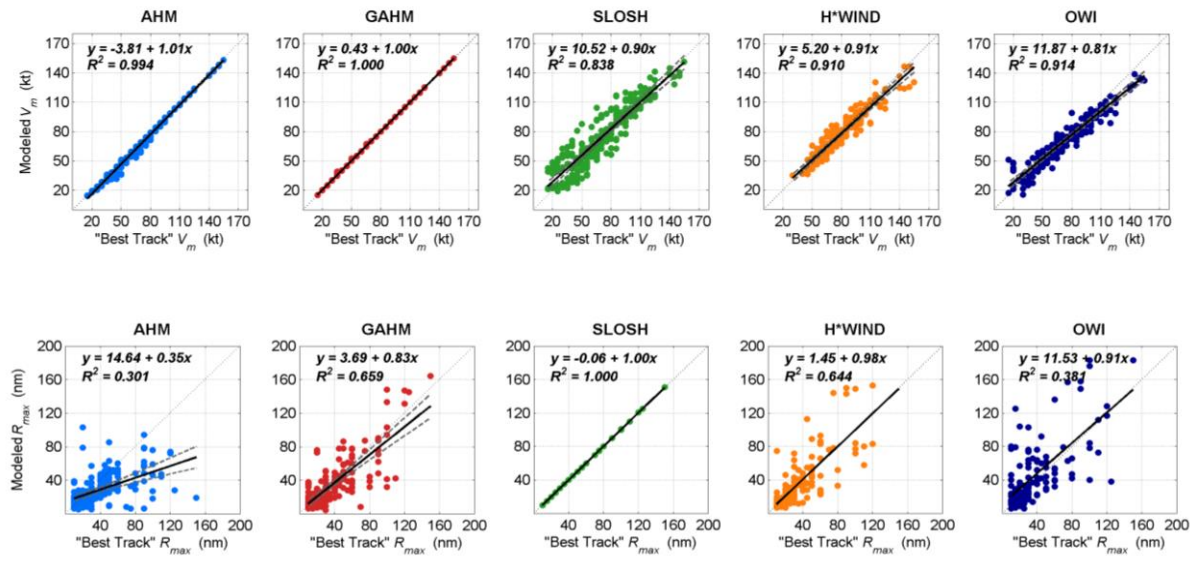


Figure 2.11. Comparison of the modeled and “Best Track”  $V_m$  (upper five panels) and the modeled and “Best Track”  $R_{max}$  (lower five panels) based on all seven hurricanes between the AHM, the GAHM, the SLOSH, the H\*Wind and OWI winds.

Comparison between the modeled and specified RMW is shown in the lower five panels, and a linear regression is made to the scatter in each panel. The correlation between the modeled and specified RMW suggested an excellent performance of the SLOSH model in estimating the RMW, which was not surprising since it uses the specified RMW in the “best track” advisories

as model input. The regression line remains close to the 1:1 (dash) line for the H\*Wind and OWI winds as well.

### **2.5.2 Model Consistency at Distances to All Available Isotach**

Time-series radial wind profiles in each of the NE, SE, SW and NW storm quadrants were generated for all seven storms using the multiple-isotach approach in the GAHM at the 6-hour interval. The composite wind profiles, along with wind profiles from the AHM, SLOSH, H\*Winds, and OWI, were evaluated against all available isotachs in the “Best Track” file. Figure 2.12 gives three snapshots (corresponding to Table 2.2 and Figure 2.7) of the estimated radial wind profiles of Hurricane Irene (2011), with the left three panels showing the SW to NE cross-section winds, and the right ones showing the NW to SE cross-section winds. For each “snapshot” of the radial wind profiles, all available isotachs in the “best track” files are plotted as black vertical bars at specified distances to storm center.

Compared to GAHM’s radial wind profiles from the single-isotach approach in Figure 2.7, Figure 2.12 shows that the composite radial wind profiles produced by the GAHM perfectly match all storm isotachs in all quadrants at all time, indicating the consistency of the multiple-isotach approach. Profiles of the SLOSH model are rather mediocre in matching the highest isotachs in all three snapshots, since SLOSH does not take the isotach information as model input. Radial wind profiles extracted from the H\*Wind and OWI winds share some similarities with each other but neither of them constantly match the highest isotachs. Their discrepancies are generally within a reasonable range.

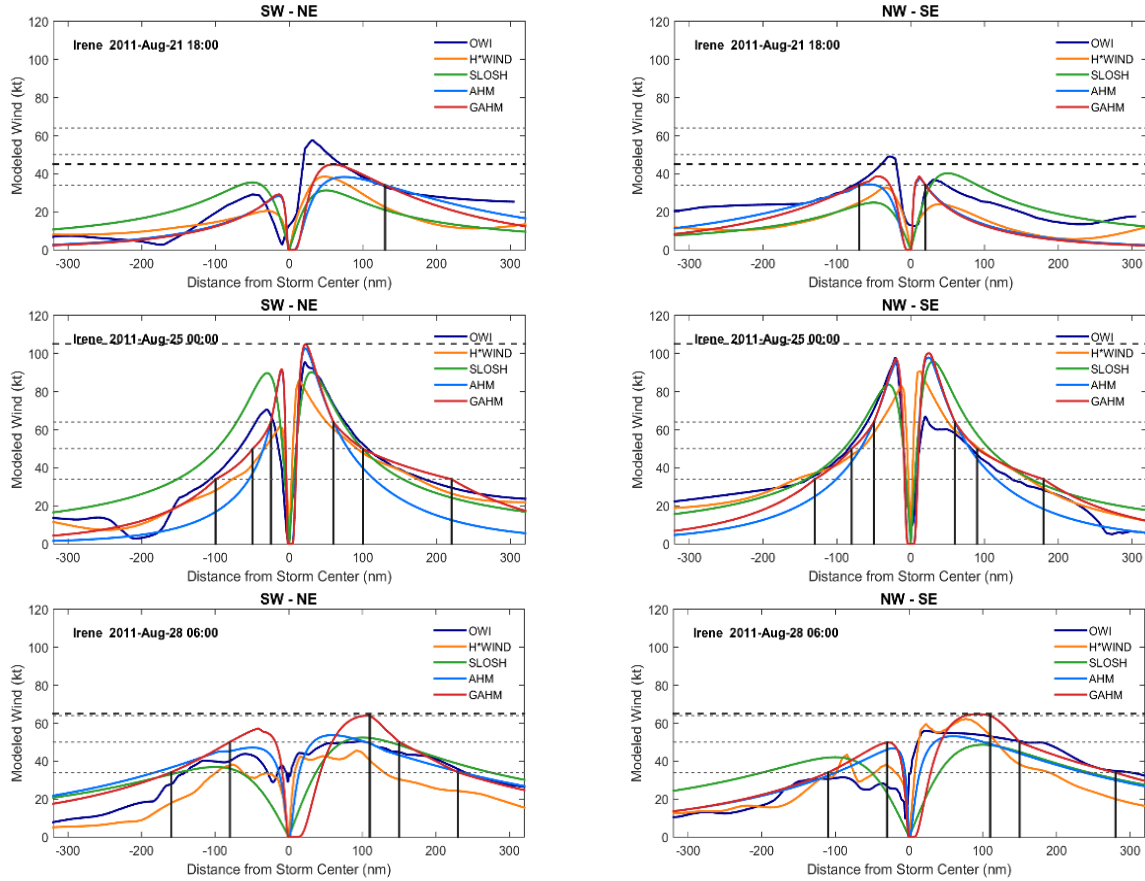


Figure 2.12. GAHM's composite radial wind profiles of Irene (2011) at 3 different developing stages. Vertical bars represent all available storm isotachs reported in NHC's "best track" file.

Considering all seven hurricanes, the overall model consistency evaluated at distances to all available specified isotach is shown in Figure 2.13, with statistics given in Table 2.3. The GAHM has almost perfect match to each of the 34-, 50-, and 64-kt isotachs, with a standard deviation generally around 0.1 kt, which is very impressive. The SLOSH does not take isotach information to construct its wind fields, thus behaves poorly by overestimating the 64-kt isotach by 5.5 kts and underestimating the 34- and 50-knot isotachs by 4.0 and 1.1 kts. It also has the widest data spread, with standard deviations  $> 11$  kts at all specified isotachs. For the H\*Wind and the OWI winds, the modeled mean wind speeds are close to each specified isotach, generally within  $\pm 3$  kts, but the spreads of data are also large compared to the AHM and the GAHM, with

a standard deviation of greater than 7 kts.

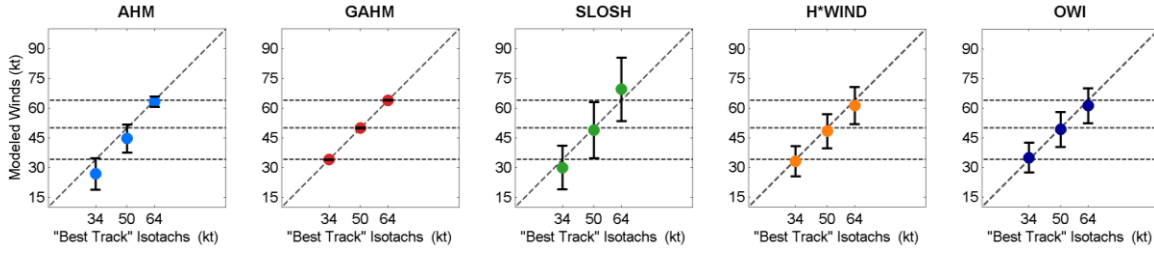


Figure 2.13. Comparison of specified isotachs and modeled winds at distances to specified isotachs for all seven selected hurricanes.

Table 2.3. Statistical analysis of modeled winds at distances to all isotachs based on all seven storms

	<i>MEAN (kt)</i>			<i>Standard Deviation (kt)</i>		
	<i>Iso-34</i>	<i>Iso-50</i>	<i>Iso-64</i>	<i>Iso-34</i>	<i>Iso-50</i>	<i>Iso-64</i>
<i>AHM</i>	26.9	44.7	63.3	7.96	7.09	2.55
<i>GAHM</i>	34.0	50.0	64.0	0.10	0.12	0.10
<i>SLOSH</i>	30.0	48.9	69.5	11.00	14.11	16.08
<i>OWI</i>	33.1	48.3	61.3	7.65	8.71	9.42
<i>H*Wind</i>	34.9	49.2	61.2	7.55	8.88	8.89

## 2.6 Summary and Discussion

In this study, efforts were made to develop a Generalized Asymmetric Holland Model (GAHM) in the ADCIRC model for operational wind forecasting purpose. Based on the classic HM, the GAHM features a set of formulae derived using the gradient wind equation without assuming the cyclostrophic balance at the RMW. Relationship between shape parameters  $A$  and  $B$  were rederived, and a modified expression of  $B$  was obtained during the derivation process, referred to as  $B_g$ . The coherently derived formulae allowed the GAHM to generate representative wind fields for a wide range of TCs consistently and faithfully, without suffering from systematic errors associated with a small  $R_o$  as the HM does. This is a huge improvement over the classic HM and the AHM, as well as many other parametric models that were developed over

the cyclostrophic wind equation, as they may fail to yield reasonable spatial wind fields under circumstances that the Coriolis force plays a significant role in the system. Similar to what was found in Wood et al. (2013) and many others, a criteria of  $\log_{10}R_o < 1$  can be identified to consider a wind flow gradient, instead of cyclostrophic, and the GAHM should be used under this circumstance to avoid distortion in the calculated RMW and maximum winds, and the overall spatial wind field. Another important feature of the GAHM is the introducing of a composite wind method, which allows the GAHM to utilize multiple storm isotachs to construct wind field validated at given radii. It ensures consistency of modeled winds when- and wherever wind observations were provided.

Evaluation of GAHM was carried out using seven selected hurricanes that struck the U.S. East Coast and the Gulf of Mexico in the past decade. Examination of modeled winds at distances to all available isotachs and the radius to maximum wind suggested that the GAHM was able to produce surface wind fields that consistently matched the NHC's advisory data. Comparison between the modeled maximum wind and RMW with the "Best Track" data in relation to the  $R_o$  also indicated that the GAHM is superior to the AHM in yielding truthful results without being influenced by the significance of the Coriolis force in the weather system. Comparison between the parametric model results and the more validated OWI and H\*Wind enlightened us to use the data in the NHC's "best track" file more objectively and cautiously, and to think twice whether our methodology was reasonable to assume the storm information in 4 storm quadrants are along 4 fixed azimuthal angles.

As a prototype for parametric wind forecasting, the GAHM was designed to interpret storm information in NHC's forecast/best track advisories to construct a composite wind field. In theory, winds observed anywhere within the influential range of a hurricane could be



synthesized into the final wind field to improve model accuracy. Future work could be taken to improve the GAHM so that it can sophisticatedly assimilate wind data from other sources to yield better representation of the realistic wind fields.

## **CHAPTER 3: EXPLICIT SURFACE WIND STRESS UNDER TROPICAL CYCLONES FOR STORM SURGE MODELING**

### **3.1 Introduction**

In contrast to land surface that is static or evolving slowly over long time scales (e.g., evolution of coastal sand dunes or vegetation coverage), surface water waves develop over short time scales under atmospheric forcings. If winds persist over a large enough fetch, the wave field evolves and reaches equilibrium. Under a transient weather system like a hurricane, the wave field is under-developed, and is rather complicated in different sectors of the storm. Also, when wind speed is high enough, the air-sea interface becomes a foam, bubble, spray layer and will affect the surface roughness of the sea, effectively making the surface more “slippery”. Quantifying exactly how much momentum is transferred under various conditions has been studied for decades.

#### **3.1.1 RHG and DCCM**

To investigate the impact of surface wave field on surface wind stress in fetch-dependent seas, Reichl et al. (2014) conducted numerical experiments to examine the influence of sea state on surface momentum flux using two wave-dependent stress calculation methods, the RHG (a modified version of Moon et al., 2004, with added influence of swell on wave growth rate), and the DCCM (Donelan et al., 2012). There are two major differences between the RHG and DCCM. One is the calculation of wave growth rate. While both RHG and DCCM uses (14) to evaluate its form drag at the surface  $z = 0$ , they calculate  $\beta(k, \theta)$  quite differently. The RHG

parameterizes  $\beta(k, \theta)$  from the turbulent stress at the inner layer height  $z = \delta/k$  (Hara and Belcher, 2004), where the parameter  $\delta$  is empirically adjusted to match the resulting total drag coefficient to observations at low to moderate wind speeds (in this study  $\delta = 0.03$ ). For wave propagating perpendicular to wind,  $\beta(k, \theta)$  is set to 0. The DCCM parameterizes  $\beta(k, \theta)$  from the wind speed; waves propagating at large angles relative to wind speed contribute significantly to the form drag, effectively increasing the misalignment between total stress and wind speed. Another major difference is the calculation of the wind profile. The RHG considers energy conservation inside the wave boundary layer. It assumes the wind shear is aligned with the turbulent stress at all heights, meaning that the wind speed vector can turn with height within the wave boundary layer. The DCCM, on the other hand, does not explicitly consider energy conservation in the wave boundary layer. In fact, it assumes the wind profile follows a logarithmic “law of the wall” profile, meaning that the wind speed vector is fixed in direction. Thus, the wind and stress can be significantly misaligned. See Reichl et al. (2014) for more mathematical details of the RHG and DCCM.

The wave spectra used in Reichl’s study were simulated using WAVEWATCH III (hereinafter WWIII, Tolman, 2009). WWIII is a third generation wave model developed at the National Center for Environmental Predictions (NCEP) for operational use. It simulates the evolution of wind waves by accounting for the wind source input, nonlinear wave-wave interaction, wave dissipation (“whitecapping”) in deep water, and additional wave shoaling and breaking processes in shallow water. The WWIII has its own  $C_d$  parameterization and wave growth rate parameterization, the latter of which being empirically adjusted to produce wave spectra that agree well observations mostly at low to moderate winds. Note, the feedback of the wave-dependent stress on wave simulations was not pursued in Reichl’s study. The WWIII

resolves wave spectrum explicitly up to  $3 \times$  the peak input frequency  $f_p$ , and internally attaches an empirical high-frequency spectral tail.

A few constant saturation tail levels for  $B(k)$  were tested in Reichl's study, including a low ( $B = 2 \times 10^{-3}$ ), a medium ( $B = 6 \times 10^{-3}$ ), and a high  $B$  value ( $B = 12 \times 10^{-3}$ ), where  $B(k) = \Psi(k)k^4$  is the directionally integrated saturation spectrum and is assumed to be constant over  $k$  at the high frequency tail. The model simulated spectrum was used up to  $1.25 \times f_p$ , then linearly transitioned to the constant tail level  $B$  from  $1.25 \times f_p$  to  $3 \times f_p$  (Figure 3.1).

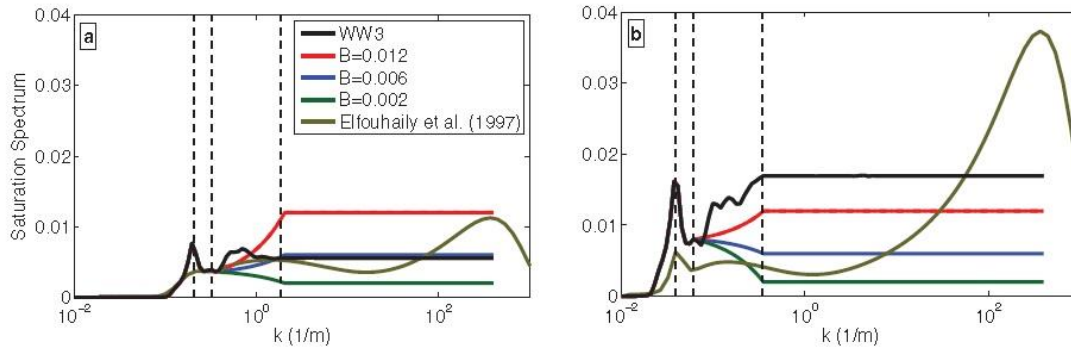


Figure 3.1. Directionally integrated saturation spectrum simulated in WWIII with WWIII original tail, three constant tail level options, and empirical tail of Elfouhaily et al., 1997 for (a) 10 m/s wind, and (b) 40 m/s wind experiments. Three vertical dashed lines represent wavenumbers corresponding to  $f_p$ ,  $1.25 \times f_p$ , and  $3 \times f_p$  (Reichl et al., 2014).

Once the wave spectra were constructed, total momentum flux from the atmosphere to the ocean was calculated using both the RHG and DCCM methods. It was found that the computed  $C_d$  is very sensitive to the spectral tail level used, but is not as sensitive to the stress calculation methods. This is the consequence of the fact that the wave induced stress is mainly supported by the high frequency part of the spectrum. Also, it was found that no single  $B$  value could produce  $C_d$  to agree well with observations such as the COARE 3.5 (Edson et al. 2013) at its entire wind speed range. If the spectral tail level is not set as constant, but as a function of

wind speed, wave age, or both, technically  $C_d$  can be constructed to match any observations or any analytical functions. It reminds us that certain physical processes that affect the surface wind stress might be missing. Riechl's results in general contradict the results by Ho12.

### 3.1.2 Objectives

As storm surge modelers, we are mostly concerned with coastal storm surge and inundations induced by tropical cyclones, especially by landfalling hurricanes. Since most observations under hurricane conditions were made over deep water, our knowledge of the surface drag mechanisms under hurricane forcings in shallow water is still limited. Previous studies suggested that the surface roughness in shallow water region would be enhanced by the existence of shoaling and breaking waves under moderate wind speeds (Taylor and Yelland, 2001; Walsh et al, 2002). We are interested to find out if sea state dependent  $C_d$  behaves differently in shallow water than in deep water under hurricane wind conditions.

Currently, the operational ADCIRC storm surge model has two options when specifying the wind drag coefficient: 1) the wind speed-dependent  $C_d$  by Garratt (1977), and b) the storm sector-dependent  $C_d$  by Powell (2007). In an effort to address the uncertainties in different surface drag estimates and their effect on storm surge modeling, we implemented the above mentioned approaches in the coupled ADCIRC and SWAN model in this study for comparisons (Table 3.1). Our main goal of this study is to investigate the behavior of explicit surface wind stress in the spirit of RHG and DCCM under various wind and wave regimes, and to examine the effect of different drag laws on storm surge modeling. More specifically, we have two main objectives.

Table 3.1. Drag laws in ADCIRC

<b>GARRATT</b>	Wind speed dependent $C_d$ , linear
<b>GFDL14</b>	Wind speed dependent $C_d$ , 2 <sup>nd</sup> order polynomial
<b>POWELL</b>	Storm sector based
<b>SWELL</b>	DSPR and wind speed based
<b>WAVE AGE</b>	Wave age based $z_0$
<b>WAVE STEEPNESS</b>	Wave steepness based $z_0$
<b>RHG</b>	Explicit Sea Surface Stress based on 2D wave spectrum
<b>DCCM</b>	Explicit Sea Surface Stress based on 2D wave spectrum

### **Sensitivity Study of the Explicit Surface Wind Stress on diagnostic tail and prognostic 2D spectrum**

There are many studies based on the concept of a physically-based formulation of surface wind stress that include the impact of all waves, but they diverge in a few main aspects, such as the parameterization of the spectral tail, the formulation of the wave growth rate  $\beta(k, \theta)$  (defined as the input rate of momentum to waves) especially for following, crossing and opposing swells, the quantification of wave breaking impacts, etc. Since shorter waves in the equilibrium range are the major rough elements, contribution of the spectral tail on surface wind stress depends significantly on its parameterization. Here we want to study the sensitivity of the surface drag to different spectral tail parameterizations, as well as to the prognostic wave spectrum simulated using different physics packages in SWAN, under various wind and wave regimes.

Waves in shallow water are much more complex than in deep water, as they suffer from shoaling, depth-induced breaking, and other physical processes approaching the shore. We speculate that the surface wind stress in shallow water is higher than in deep water, as waves slow down, become steeper and higher, and ultimately break, essentially increasing the

aerodynamic roughness of the sea surface. We will explore the behavior of RHG and DCCM in shallow water to see if there's enhancement of  $C_d$ .

### **Impact of Different Drag Laws on Storm Surge Modeling**

In storm surge modeling, a wind speed-dependent bulk formula of  $C_d$  (such as Garratt) often yields a stress field that generally follows the pattern of the surface wind field. However, a sea state-dependent surface stress field often has a very different spatial pattern, especially under tropical cyclones where waves are of different developmental stages in different sections of the hurricane. Thus, the estimated storm surge at geographical locations of interest could be highly sensitive to different drags. Also, by addressing the impact of different types of swell (following, crossing, or opposing), an explicit wave dependent drag law such as RHG and DCCM allows the estimated surface stress vectors to be misaligned with the wind vectors, a phenomenon commonly observed under hurricane vortex winds. Influence of the sea state-dependent surface wind stress on storm surge modeling should be examined.

## 3.2 Methodology

### 3.2.1 Implementation of Sea State Dependent Stress in Coupled ADCIRC + SWAN

Swan is a third generation wave model for estimating wave parameters in coastal areas given wind, bottom, and current conditions, and solves the wave action balance equation with source and sink terms, including wind input, whitecapping, depth-induced breaking, dissipation by bottom friction, and wave-wave interactions in both deep and shallow water.

Since there are several physics packages in SWAN, when coupling RHG and DCCM to ADICRC+SWAN, we would like to examine the sensitivity of the explicit sea state dependent  $C_d$  to SWAN's different physics packages. Three out of four of SWAN's physics packages (except the most recent ST6, which we plan to add in the future) were used to conduct the experiments (Table 3.2).

Table 3.2. Physics packages in SWAN

<b>KOMEN</b>	Komen et al. (1984)
<b>JANSSEN</b>	Janssen (1991)
<b>WESTHUYSEN</b>	Van der Westhuysen et al. (2007)
<b>ST6</b>	Rogers et al. (2012)

A schematic implementation of RHG and DCCM in the coupled ADCIRC+SWAN is shown in Figure 3.2 (items in green boxes are still under development). Both RHG and DCCM can readily be ported from WWIII to SWAN by changing the variable dependencies. Table 3.3 gives the input and output variables of RHG and DCCM.



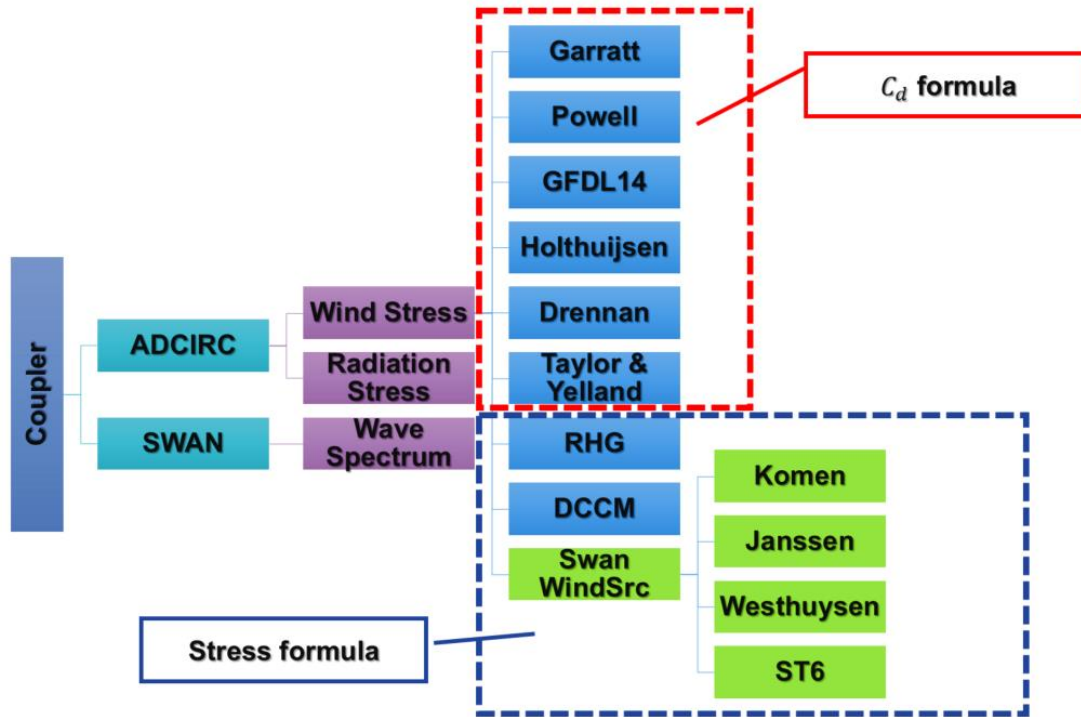


Figure 3.2. Coupling different drag laws to ADCIRC+SWAN

Table 3.3 Input and output list for RHG and DCCM

	VARIABLES	DESCRIPTIONS
INPUT	ASPC	2-d Wave action spectrum
	FPI	Peak input frequency
	WNDX	Wind magnitude in x-direction
	WNDY	Wind magnitude in y-direction
	ZWND	Height of wind vector
	DEPTH	Depth of water
OUTPUT	RIB	Bulk Richardson number
	UST	Magnitude of friction velocity
	USTD	Direction of friction velocity
	Z0	Roughness height
	TAUNX	Total Stress (x)
	TAUXY	Total Stress (y)

The total stress will be passed to ADCIRC to provide atmospheric forcing. It is important to note that a strong assumption is often made for the boundary condition in storm surge modeling: the surface wind stress equals to the ocean stress, which is the downward flux of momentum from the air into the currents. This assumption is valid for fully developed seas, in other words, the wave field is neither growing nor decaying. This assumption does not hold in transient weather systems such as hurricanes. When strongly forced by the wind, growing waves act like a giant momentum reservoir, effectively reducing the momentum flux from the air to the ocean currents. On the other hand, decaying waves release wave momentum to the current and effectively increase the ocean stress. In this study, we simply assume that the atmospheric stress equals to the ocean stress.

Since the integrated  $C_d$  was found to be very sensitive to the saturation tail level (Reich et al., 2014), we carried out sensitivity tests using a different tail option than Reichl's empirical tail: the extended tail. With this new option, a  $k^{-4}$  spectral tail will be attached to the SWAN spectrum at  $3 \times f_p$ , with the saturation tail level B equal to the model computed saturation level at  $3 \times f_p$  (Table 3.4).

Table 3.4. Specification of saturation tails in this study

<b>REICHL'S EMPIRICAL TAIL</b>	$k^{-4}$ spectral tail with saturation tail level B as a function of wind speed, attached at $3 \times f_p$ and linearly interpolated between $1.2 \times f_p$ and $3 \times f_p$
<b>EXTENDED TAIL</b>	$k^{-4}$ spectral tail with saturation tail level B computed at $3 \times f_p$ and attached at $3 \times f_p$

### 3.2.2 Experimental Design

A relatively course unstructured grid (node-31435, element-58369, no high resolution grids at coastal area) is used to conduct the experimental runs for efficiency rather than accuracy purpose (Figure 3.3). No tide is setup at the open ocean boundary in ADCIRC. In SWAN, we set the number of directional bins to  $MDC = 36$  with a constant directional resolution  $\Delta\theta = 10^\circ$ , and the number of spectral bins to  $MSC = 40$  with  $\Delta f = 0.1f$  and  $f_{min} = 0.031 \text{ s}^{-1}$  (logarithmic). Two major experiments are conducted in this study.

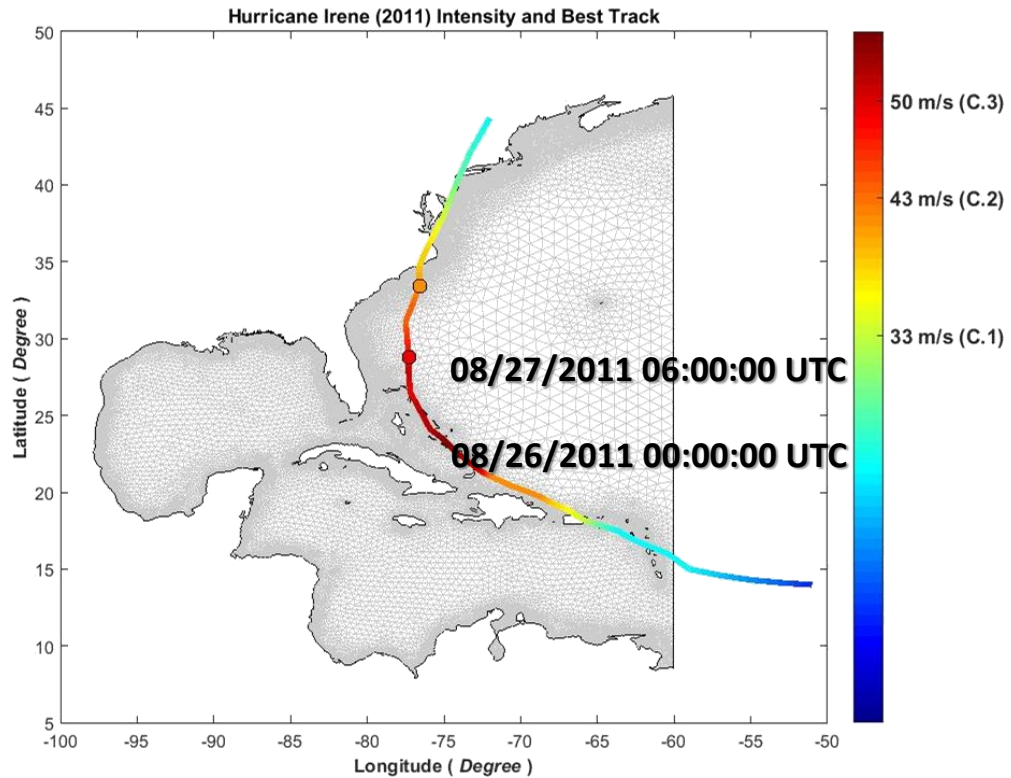


Figure 3.3. Intensity and Best Track of Hurricane Irene (08/20/2011 00:00:00 – 08/29/2011 00:00:00 UTC). Model results are investigated at two instances indicated by the circles.

## Experiment A

Sensitivity test of the explicit sea state-dependent stress to both the prognostic wave spectrum and diagnostic tail is carried out in section 3.3. An idealized symmetrical hurricane vortex is constructed using the GAHM with  $R_{max} = 142 \text{ nm}$  and  $V_{max} = 64 \text{ kt}$ , and is set to translate along Irene's best track then set stationary once storm center reaches at (77.4W, 30.0N) in deep water .

## Experiment B

Effect of different drag laws on coastal storm surge modeling using a real hurricane is carried out in section 3.4. Hurricane Irene's wind and pressure fields are reconstructed using the GAHM. Figure 3.10 shows Irene's best track and intensity. Model results at two selected snapshots are examined to cover deep and coastal water scenarios respectively: 08/26/2011 00:00 UTC and 08/27/2011 00:06 UTC.

### 3.3 Sensitivity Study of the Explicit Sea State Dependent Stress

In this section, sensitivity study of explicit sea state dependent stress on SWAN's prognostic wave spectrum and the attached diagnostic spectral tail is carried out. Since RHG and DCCM share common traits, here we use DCCM to demonstrate the results.

#### 3.3.1 Directionally-integrated Wave Spectra and Saturation Spectra

As mentioned in Section 3.2.1, SWAN has several physics packages available. To examine the modeled wave spectra from different packages, diagnostic outputs are made at 8 stations at two snapshots: 08/26/2011 03:00 UTC and 08/28/2011 21:00 UTC of an idealized hurricane (Figure 3.4).

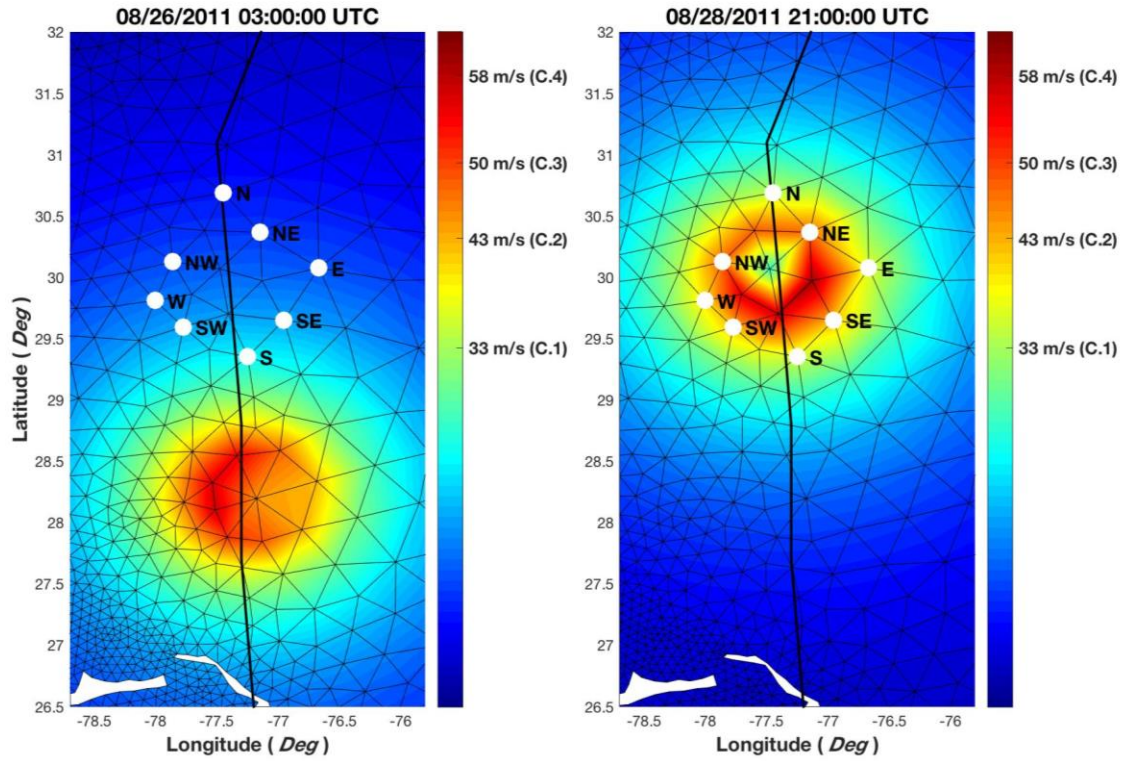


Figure 3.4. Spatial wind field at two snapshots: 08/26/2011 03:00 UTC (left panel) and 08/28/2011 21:00 UTC (right panel). Diagnostic stations are shown in white dots.

Figure 3.5 gives the comparison of 1-D wave spectra and the 1-D saturation spectra among Komen, Janssen, and Westhuysen at the first snapshot (08/26/2011 03:00 UTC) for the translating hurricane. Results suggest that the modeled spectra differ greatly at the stations as well as with different physics packages, especially at frequencies above  $3 \times f_p$ . More importantly, the modeled saturation levels begin to diverge even before  $3 \times f_p$ . Depending on which high frequency tail option we use and at what frequency we attach the tail, the resulted spectra for integrating wave stress in RHG and DCCM can be quite different. Spectra attached with Reichl's empirical tail and our extended tail are given in Figure 3.6 and 3.7, respectively. Since Reichl's saturation tail level is purely wind speed dependent, it is expected that the same tail is attached above  $3 \times f_p$  at each station no matter what physics package we use (interpolated

between  $1.2 \times f_p$  and  $3 \times f_p$ ). On the contrary, the extended tail is attached at  $3 \times f_p$  and it maintains the modeled saturation tail level at  $3 \times f_p$  at each station. Thus, quite distinctive spectral tail levels at each station and among different physics packages are found. At this snapshot, saturation levels of Reichl's empirical tail option are much higher than that of the extended tail option, and a much higher integrated wind stress is expected from the former tail option.

Figure 3.8~3.10 give the same comparisons as Figure 3.5~3.7 do except at the second snapshot (08/28/2011 21:00 UTC). In this case, the idealized hurricane has been set stationary in deep water long enough for the wave field underneath to reach steady state. Thus, differences in spectra and saturation spectra are much smaller among different stations compared to the previous snapshot. Again, with Reichl's empirical tail, the same tail is attached at each station depending on the wind speed no matter what physics package we use. With the extended tail, the saturation tail levels are generally very high. It is expected that a higher integrated stress can be found from the latter tail option.

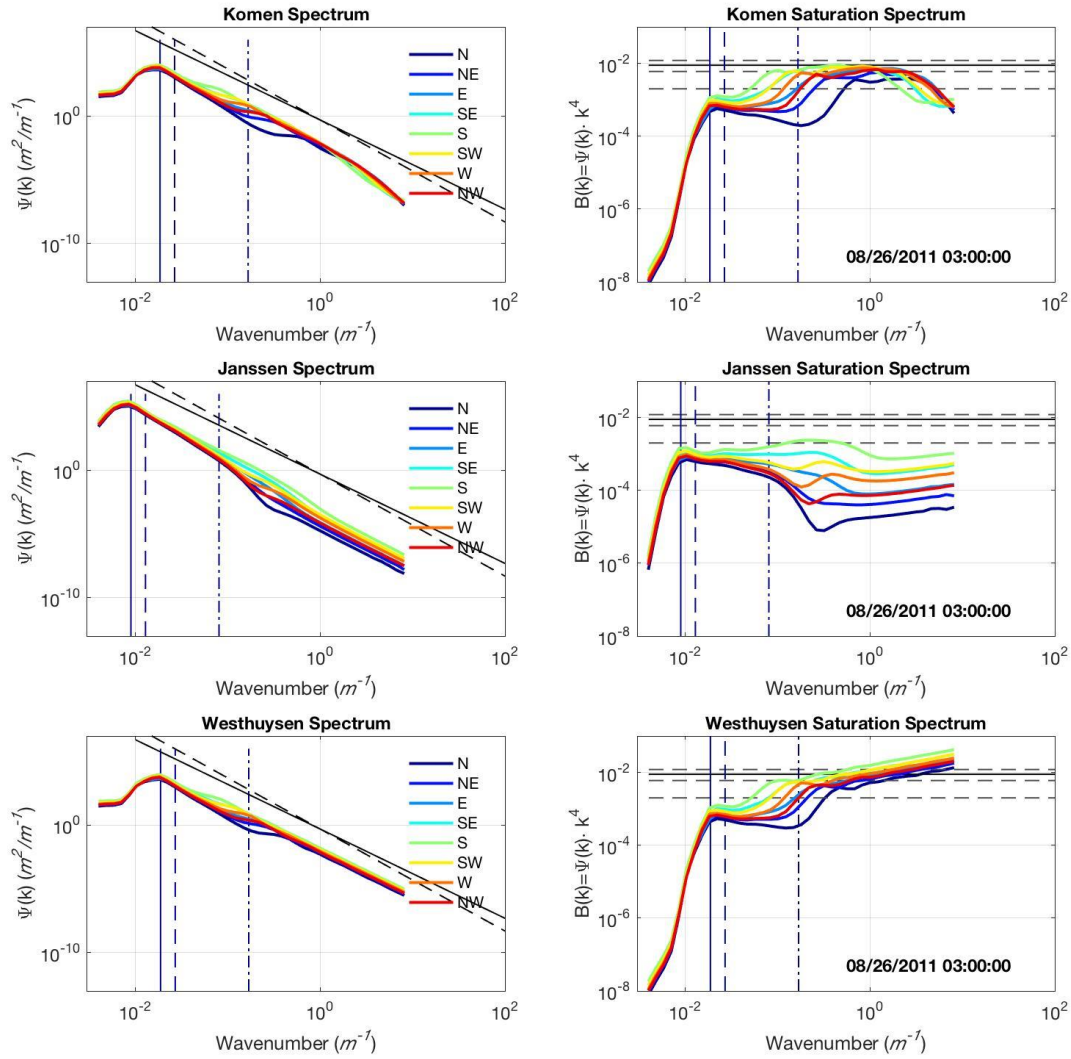


Figure 3.5. Comparison of 1-D wave spectra (left column) and the corresponding saturation spectra (right column) among Komen, Janssen, and Westhuysen in SWAN at eight stations (shown with different colored lines) at the first snapshot (08/26/2011 03:00 UTC). Three vertical (dashed) lines from left to right in each panel represent the wavenumbers corresponding to  $f_p$ ,  $1.2 \times f_p$ , and  $3 \times f_p$  of the first station.

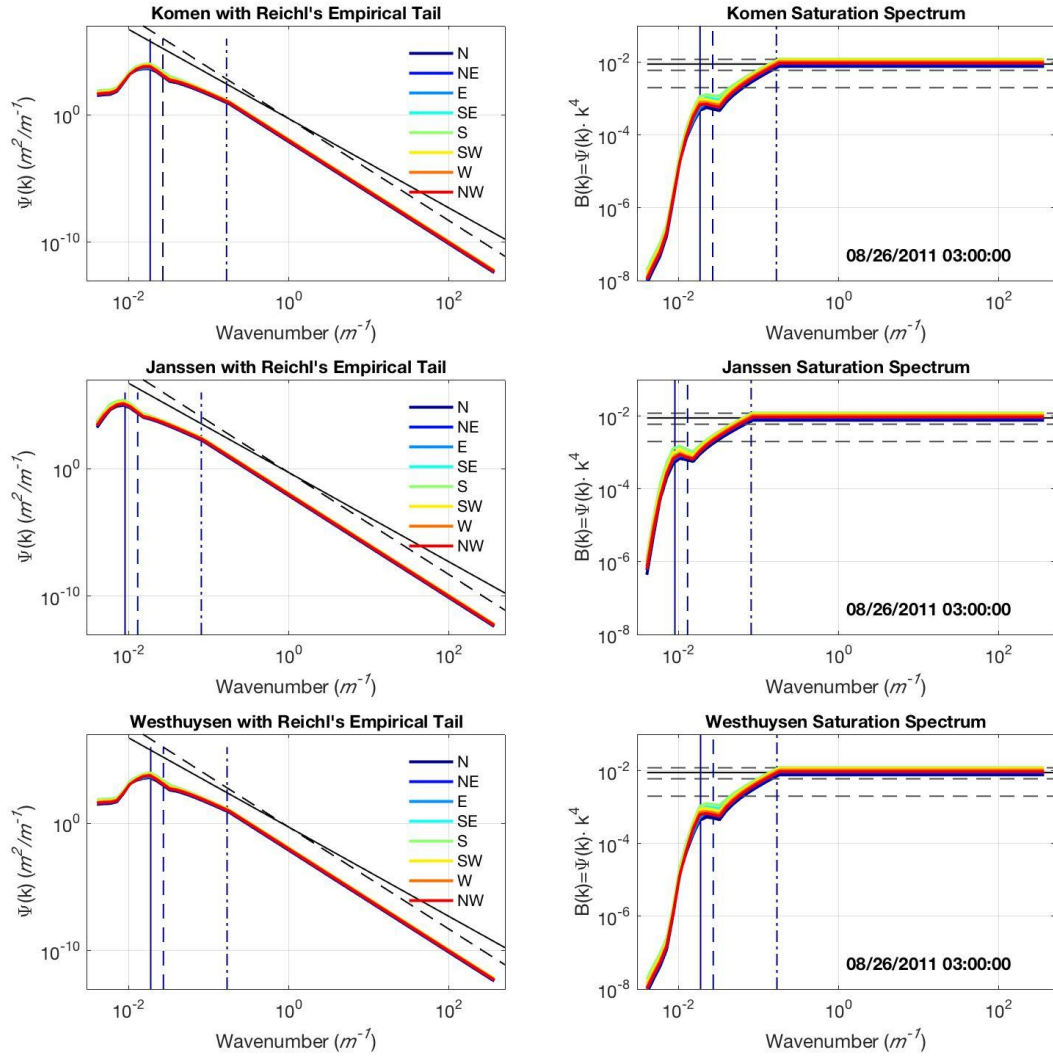


Figure 3.6. Comparison of 1-D wave spectra (left column) and the corresponding saturation spectra (right column) attached with the Reichl's empirical tail among three different physics packages at the first snapshot.



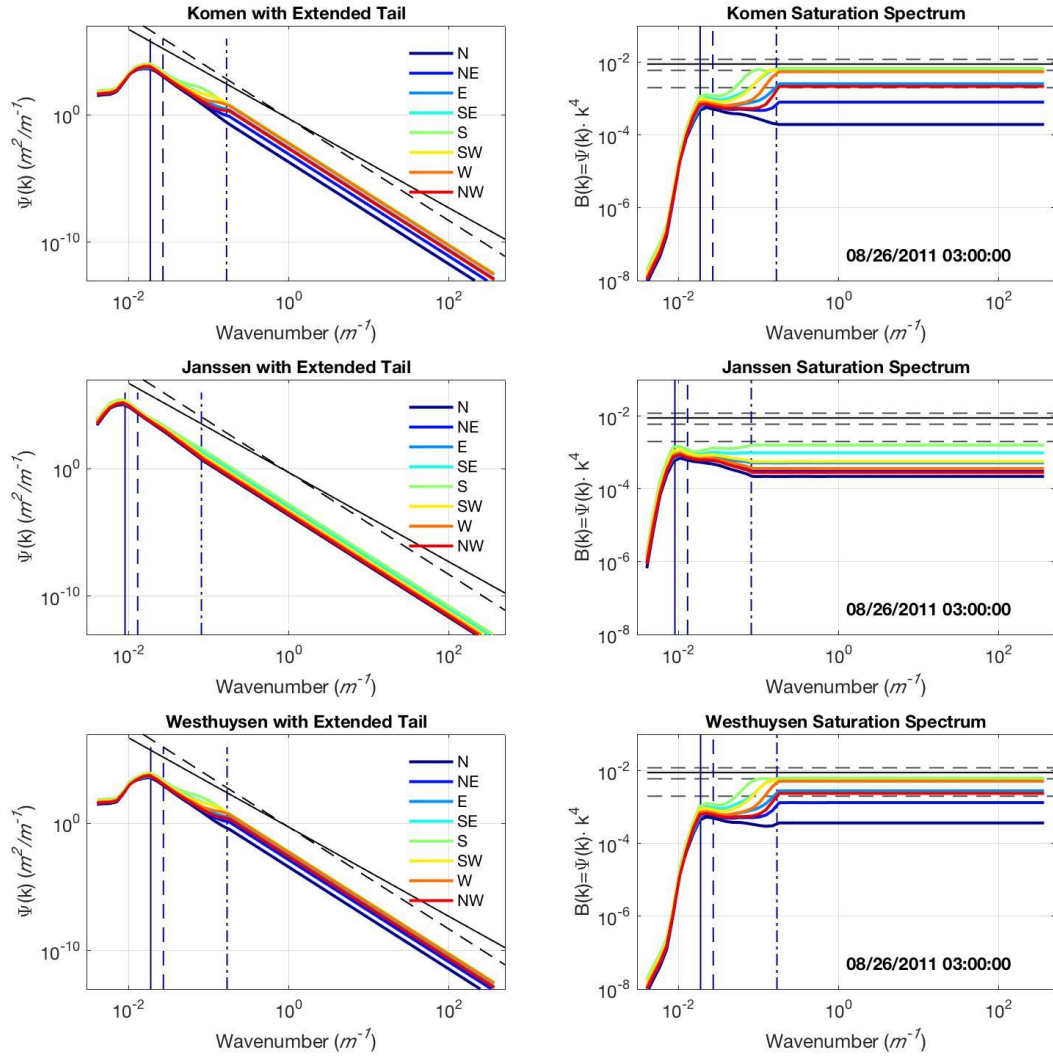


Figure 3.7. Comparison of 1-D wave spectra (left column) and the corresponding saturation spectra (right column) attached with the extended tail among three different physics packages at the first snapshot.

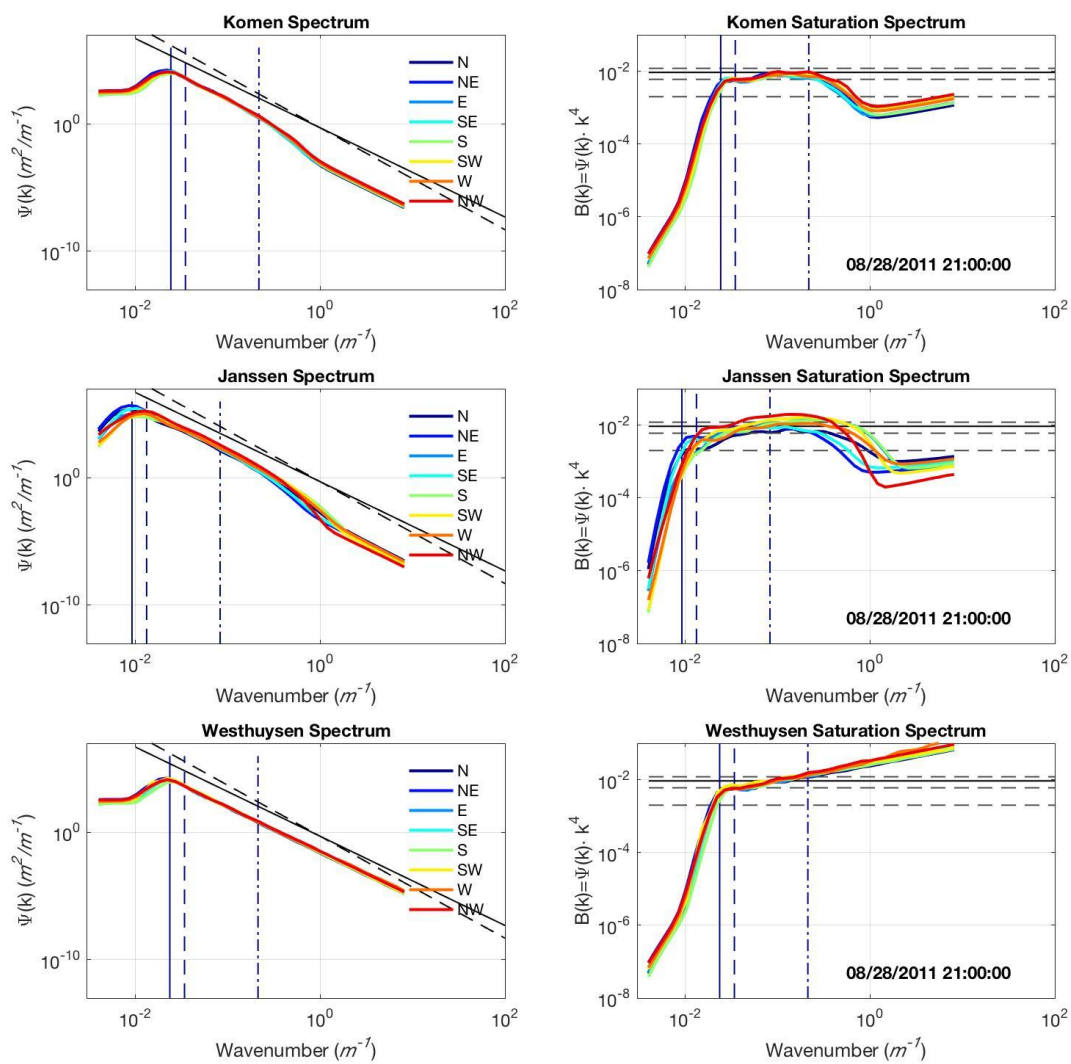


Figure 3.8. Same as Figure 3.5 but at the second snapshot (08/28/2011 21:00 UTC).

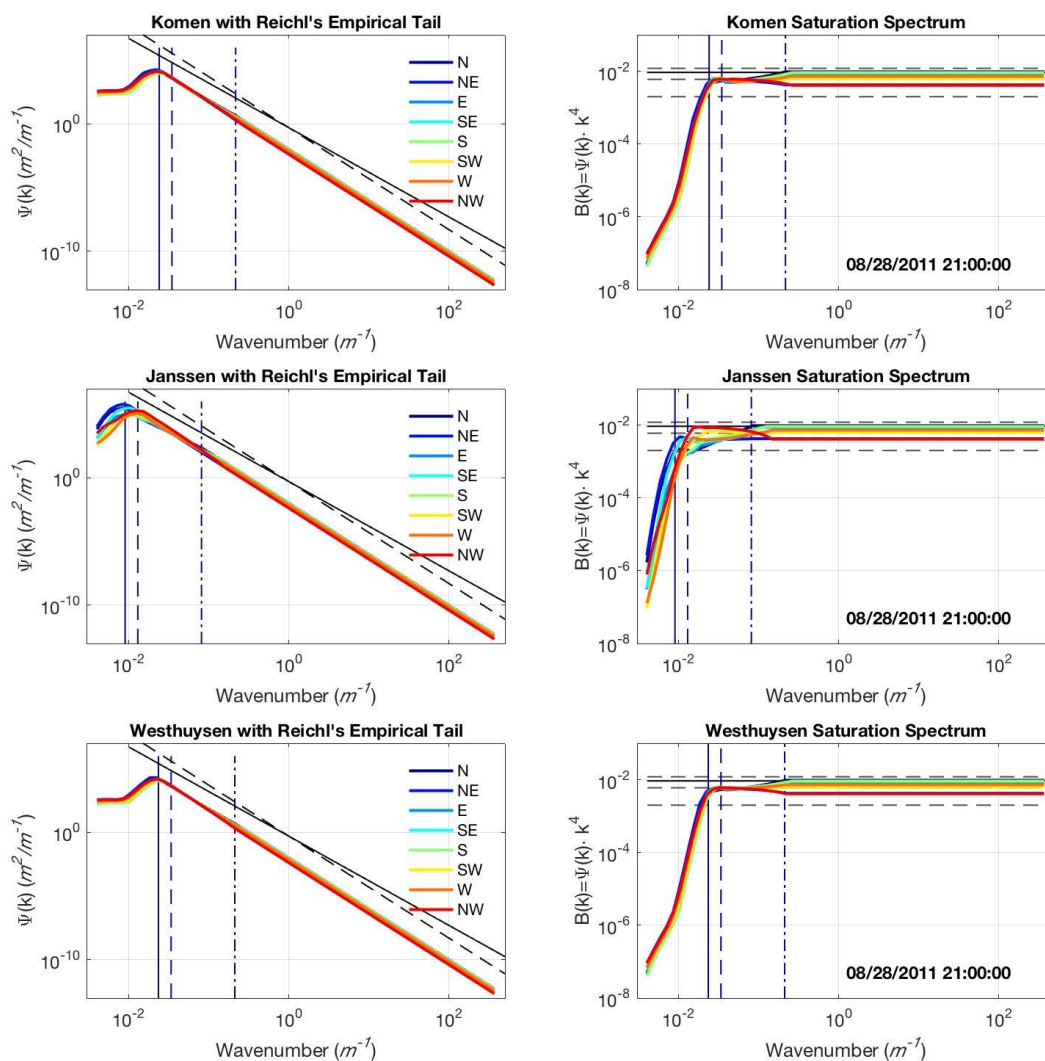


Figure 3.9. Same as Figure 3.6 but at the second snapshot (08/28/2011 21:00 UTC).

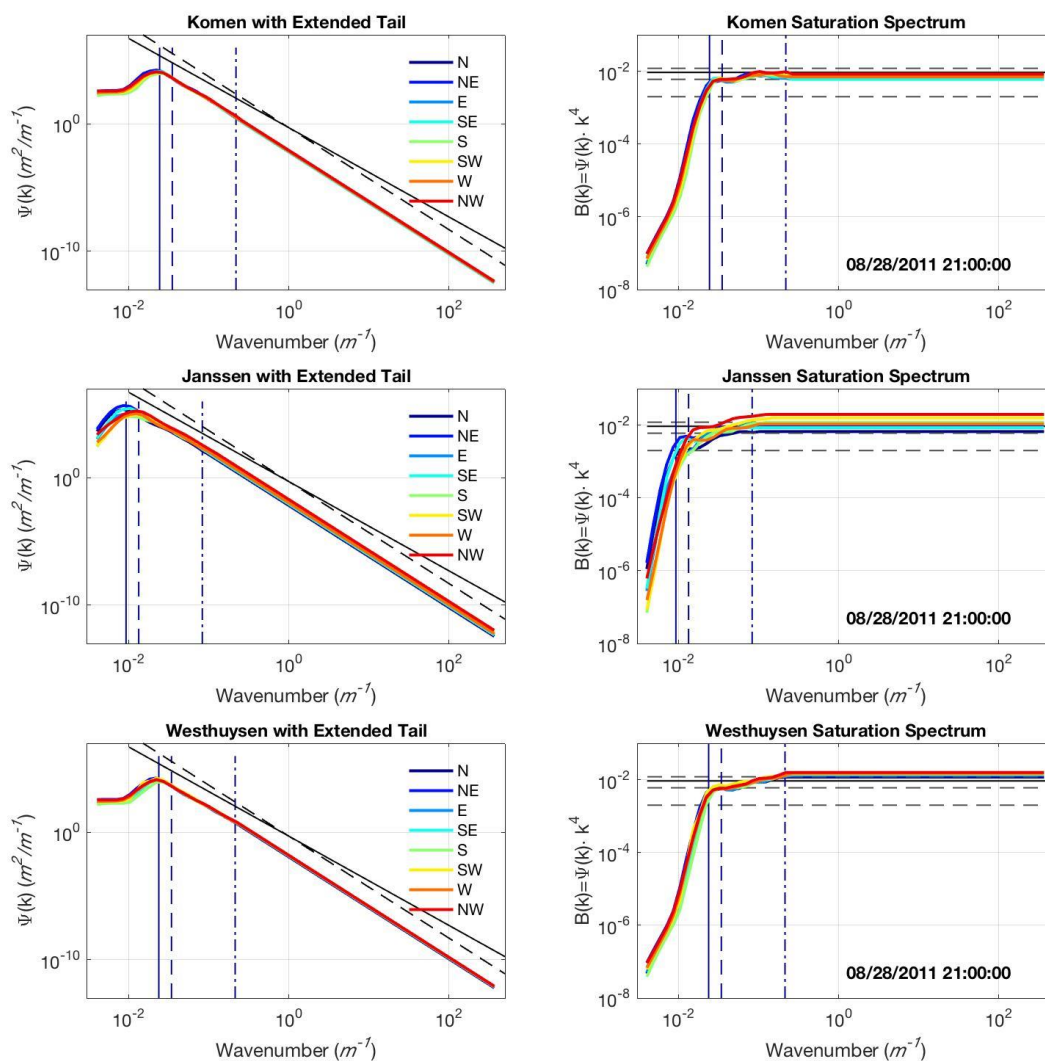


Figure 3.10. Same as Figure 3.7 but at the second snapshot (08/28/2011 21:00 UTC).

### 3.3.2 Integrated Wave Form Stress

In this section, wave spectra from Komen are used to demonstrate how wave form stress is computed in DCCM via (1.16). Both tail options are examined at eight stations at the same two snapshots: 08/26/2011 03:00 UTC and 08/28/2011 21:00 UTC.

Figure 3.11 gives the original Komen spectra and the corresponding saturation spectra computed at 08/26/2011 03:00 UTC (same as the first row of Figure 3.5); the Komen spectra attached with Reichl's empirical tail and the corresponding saturation spectra (same as the first row of Figure 3.6); and the 1-D directionally integrated wave form stress  $\tau_{wave}$  and its CDF (cumulative distribution function) over wavenumber  $k$ . The cumulative curves reveal the contribution of the spectral tail (above  $3 \times f_p$ ) to the total integrated  $\tau_{wave}$ , or effectively the form drag coefficient  $Cd_{wave}$  (values shown in the 6<sup>th</sup> panel). In this case, with wind speed ranging between 8~28 m/s, the contribution of the tail to the form stress ranges from ~65% to ~98%. In general, the higher the spectral tail level, the higher the integrated stress and the contribution of the tail. Figure 3.12 shows results for the extended tail option. In this case, the range of the saturation levels are large, and the contribution of the tail to the total integrated  $\tau_{wave}$  ranges from ~2%~ 95%. Similar to Reichl's tail option, we find that the higher the saturation level the larger the integrated stress and the contribution of the tail. But the saturation levels of the extended spectra are much lower than those of Reichl's, and as a results the  $Cd_{wave}$  is in general lower in this case.

Results for steady state wave field at 08/28/2011 21:00 UTC for Reichl's empirical tail as well as the extended tail are also given (Figure 3.13 and 3.14). With wind speed ranging between 34 m/s ~ 48 m/s and the spectral tail contributing ~60% to ~80% of the total  $\tau_{wave}$  with the

former option and ~70% with the latter option. Similar conclusion can be drawn from these two figures: the higher the saturation level, the larger the  $C_{d\_wave}$  and the contribution of the tail.

From the practices conducted in this section, we can speak with confidence that the DCCM drag is indeed very sensitive to the saturation tail level, especially for wave field under a transient weather system such as a translating hurricane. However, contribution of the tail to the total integrated  $\tau_{wave}$  also depends on the physics packages used in SWAN to a certain degree (results not shown here). This can be explained by the fact that the resolved part of the spectrum among different packages are slightly different, and if the extended tail option is used, the saturation level computed at  $3 \times f_p$  can be quite different among different physics packages (Figure 3.7 and 3.10).

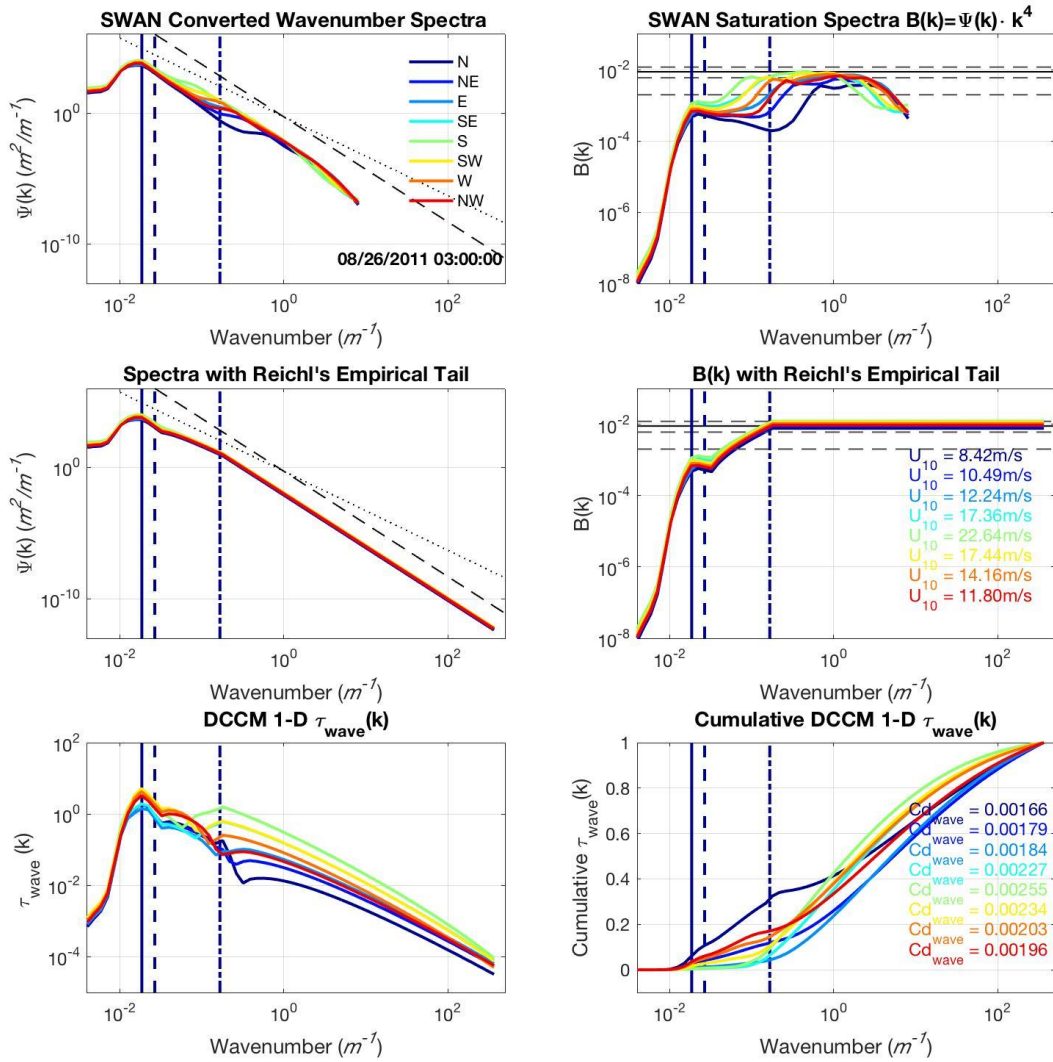


Figure 3.11. Wave spectra, saturation spectra, and integrated wave form stress profiles at 08/26/2011 03:00 UTC: a) Directionally integrated SWAN wave spectra using Komen physics package, b) SWAN saturation spectra, c) SWAN spectra with Reichl's empirical tail, d) Saturation spectra with Reichl's empirical tail, d) 1-D wave form stress over  $k$ , e) CDF of 1-D form stress over  $k$ .

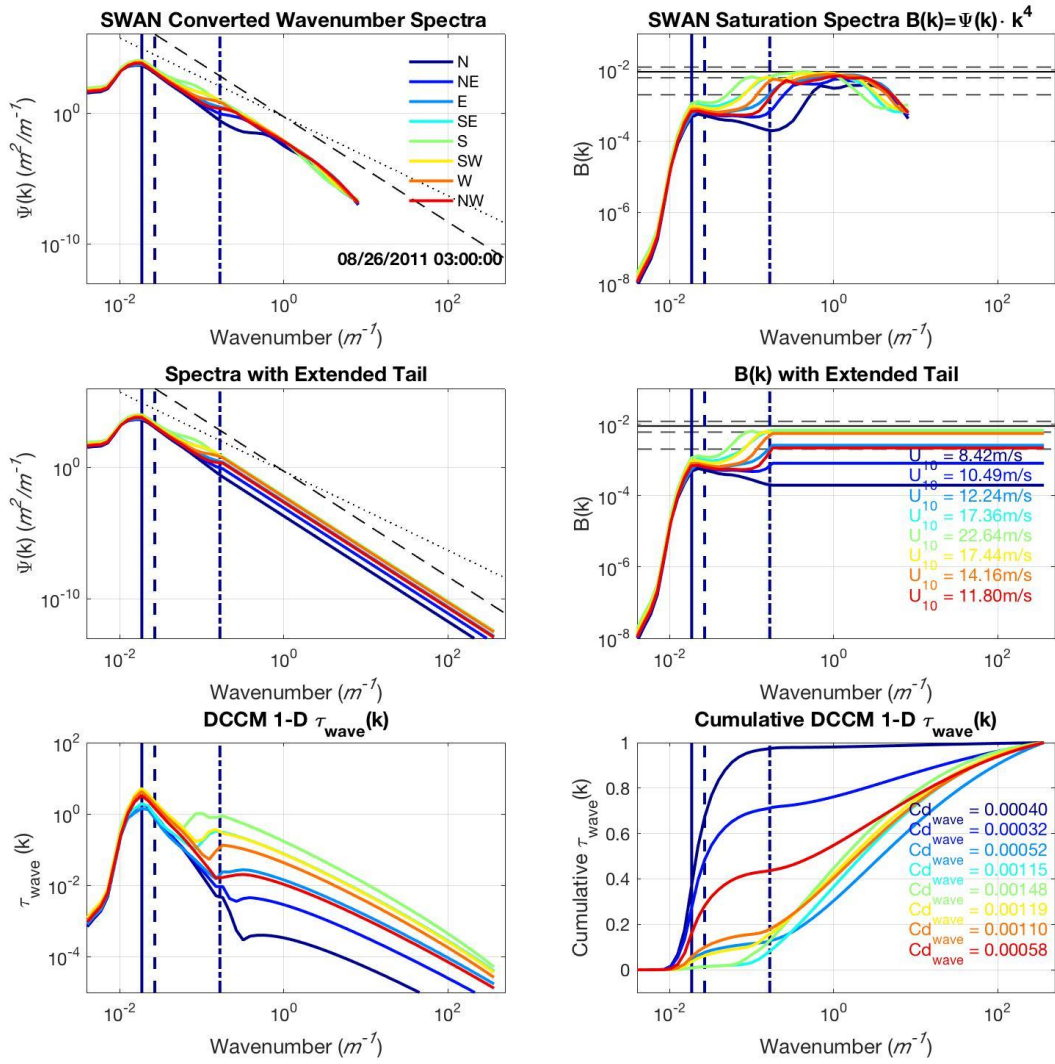


Figure 3.12. Wave spectra, saturation spectra, and integrated wave form stress profiles at 08/26/2011 03:00 UTC for the extended tail option at 08/26/2011 03:00 UTC.



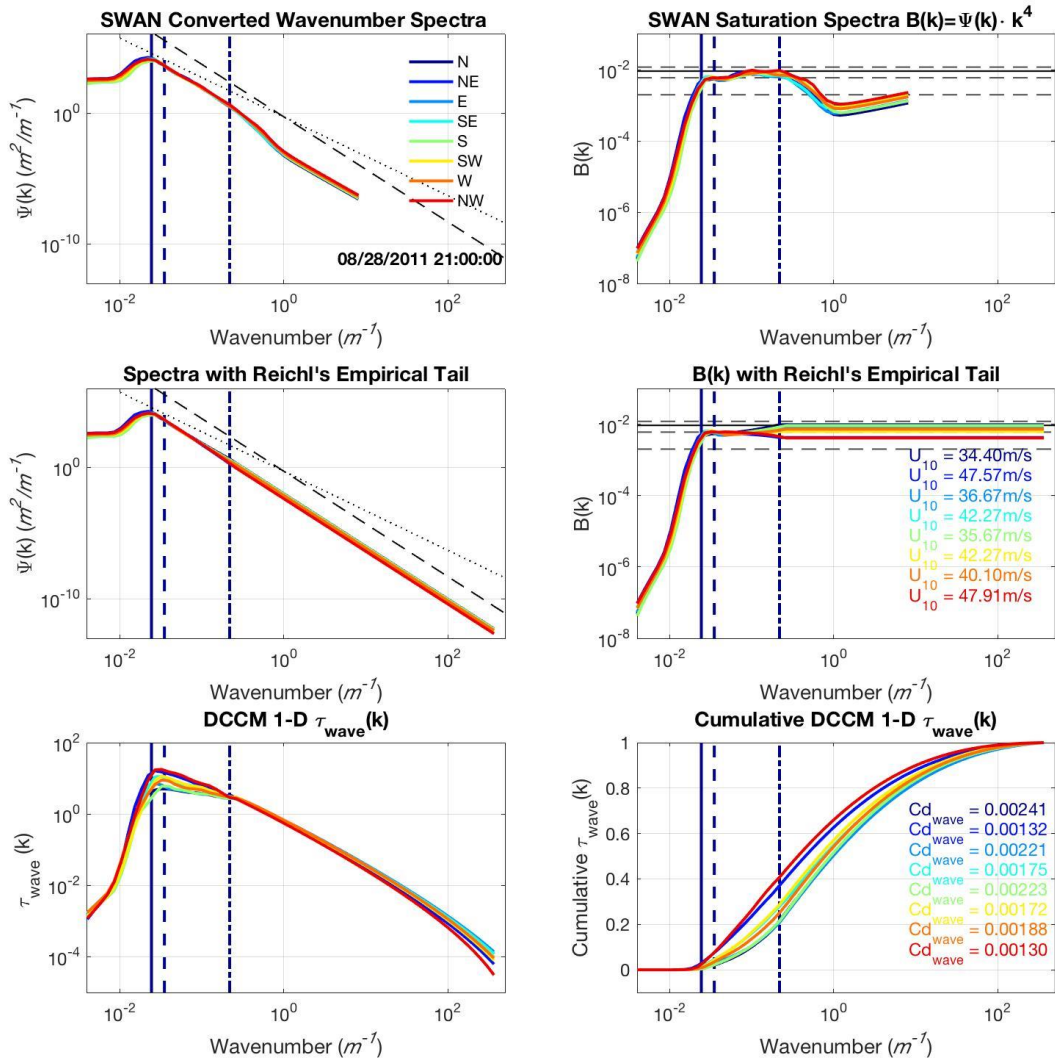


Figure 3.13. Same as Figure 3.11, except at 08/28/2011 21:00 UTC when wave field reaches steady state.

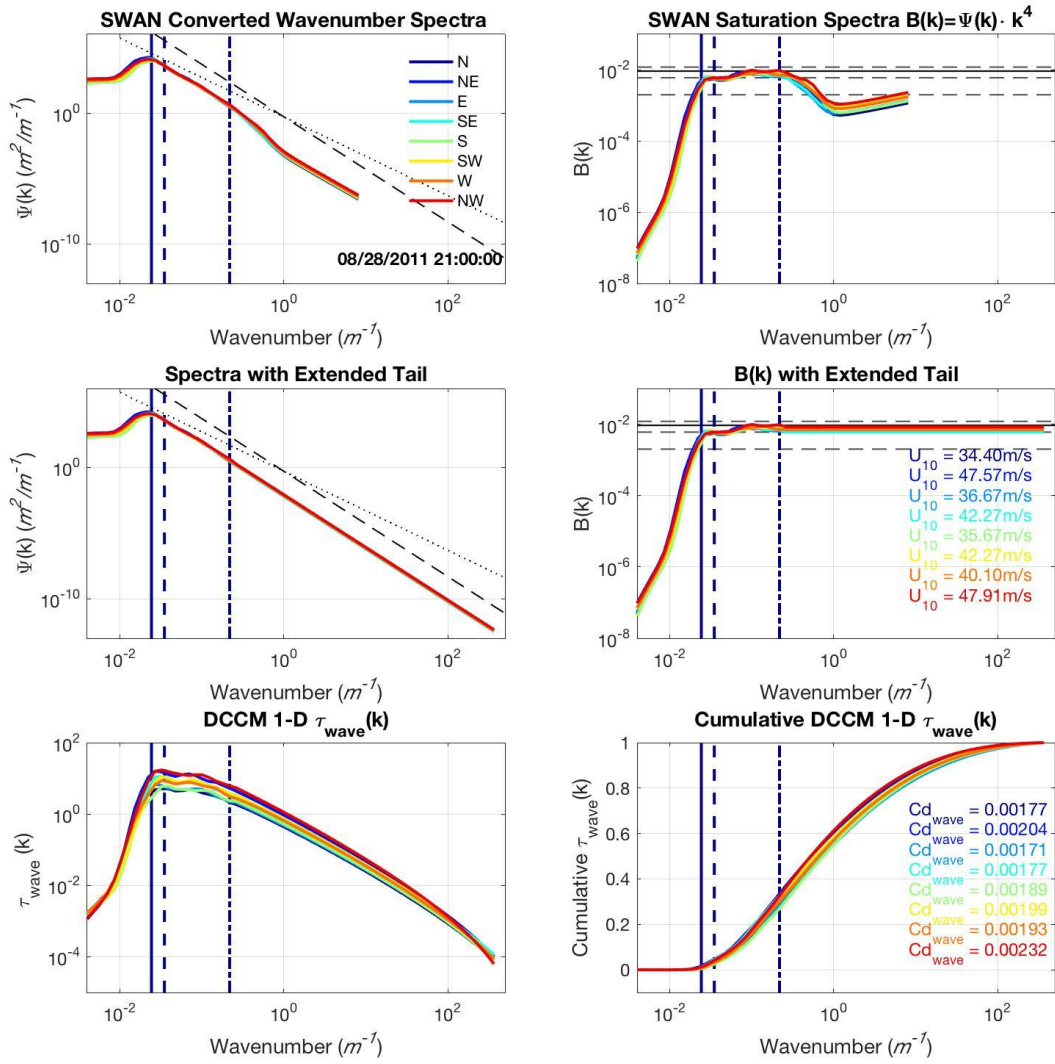


Figure 3.14. Same as Figure 3.12, except at 08/28/2011 21:00 UTC when wave field reaches steady state.

### 3.3.3 Sensitivity of $C_d$ to Prognostic Wave Spectrum and Diagnostic spectral tail

In this section, the same idealized hurricane is used as in the previous section, but we allow it to translate along Irene's best track towards shore to cover both deep and shallow water conditions (at the two snapshots marked in Figure 3.10). Since RHG and DCCM behave similarly, we use DCCM to demonstrate the results.

#### Deep Water

Spatial comparisons of the DCCM drag (along with other parameters such as saturation level  $B$  and wave directional spreading DSPR) among Komen, Janssen, and Westhuysen are given for the Reichl's empirical tail option at 08/26/2011 00:00 UTC (Figure 3.15). Note, the DCCM drag includes both the wave form stress and the viscous stress (a small portion). Since Reichl's empirical tail level is purely wind speed dependent, the spatial distribution of  $B$  follows closely to the spatial distribution of the wind field (very symmetrical in this idealized hurricane case) and is exactly the same among different physics packages. Thus, the resulted  $C_d$  share a very similar pattern. However, slight variations of  $C_d$  can be found in the Janssen package, indicating that the resolved part of the wave spectra do contribute to the total stress although the influence is relatively small in this case.

Similar spatial comparisons of the DCCM drag along with other parameters are also given for the extended tail option at 08/26/2011 00:00 UTC (Figure 3.16). The distributions of  $B$  as well as  $C_d$  behave drastically differently than those with the previous tail option, and also among different packages. This can be explained by the fact that the resolved part of the modeled spectra are different among different physics packages, which causes the saturation levels of the extended tail to be quite different.

A more direct comparison among wind speed,  $B$ ,  $C_d$  and DSPR for different tail options is given (Figure 3.17). No strong correlation between DSPR and  $B$ , or DSPR and  $C_d$  are found at the moment. Distributions of  $C_d$  as a function of wind speed are quite consistent among different physics packages for Reichl's empirical tail option, which make sense as Reichl's empirical tail was designed to fit the resulted  $C_d$  to the GFDL14 curve. For the extended tail option,  $C_d$  in general increases with wind speed (not linearly, rate of increase slows down towards high wind), and reaches very high  $C_d$  value at high winds. This obviously contradicts with Powll's findings under hurricane wind conditions.

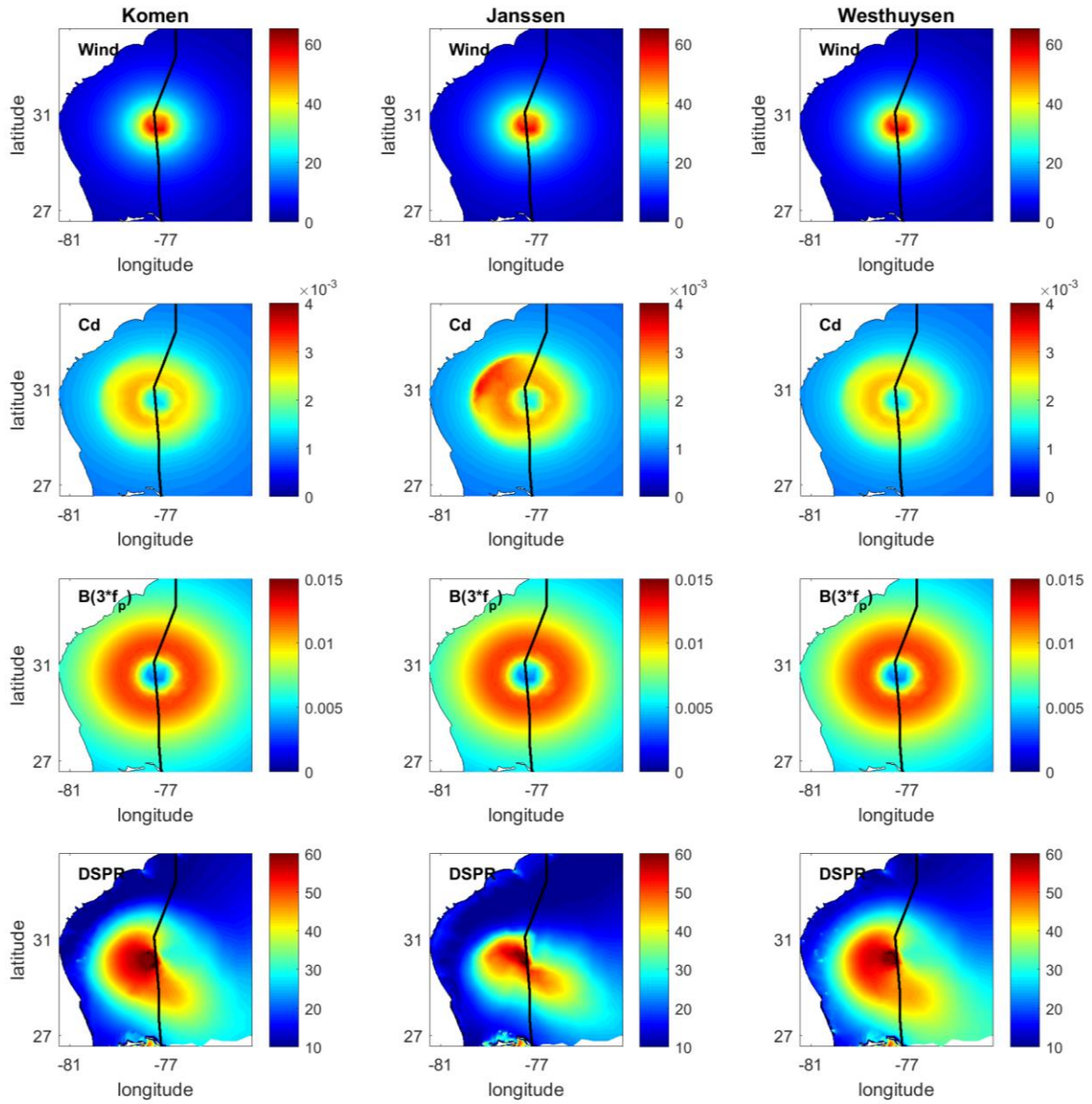


Figure 3.15. Spatial plot of wind speed,  $C_d$ , Saturation tail level, and DSPR at 08/26/2011 00:00 UTC for Reichl's empirical tail option

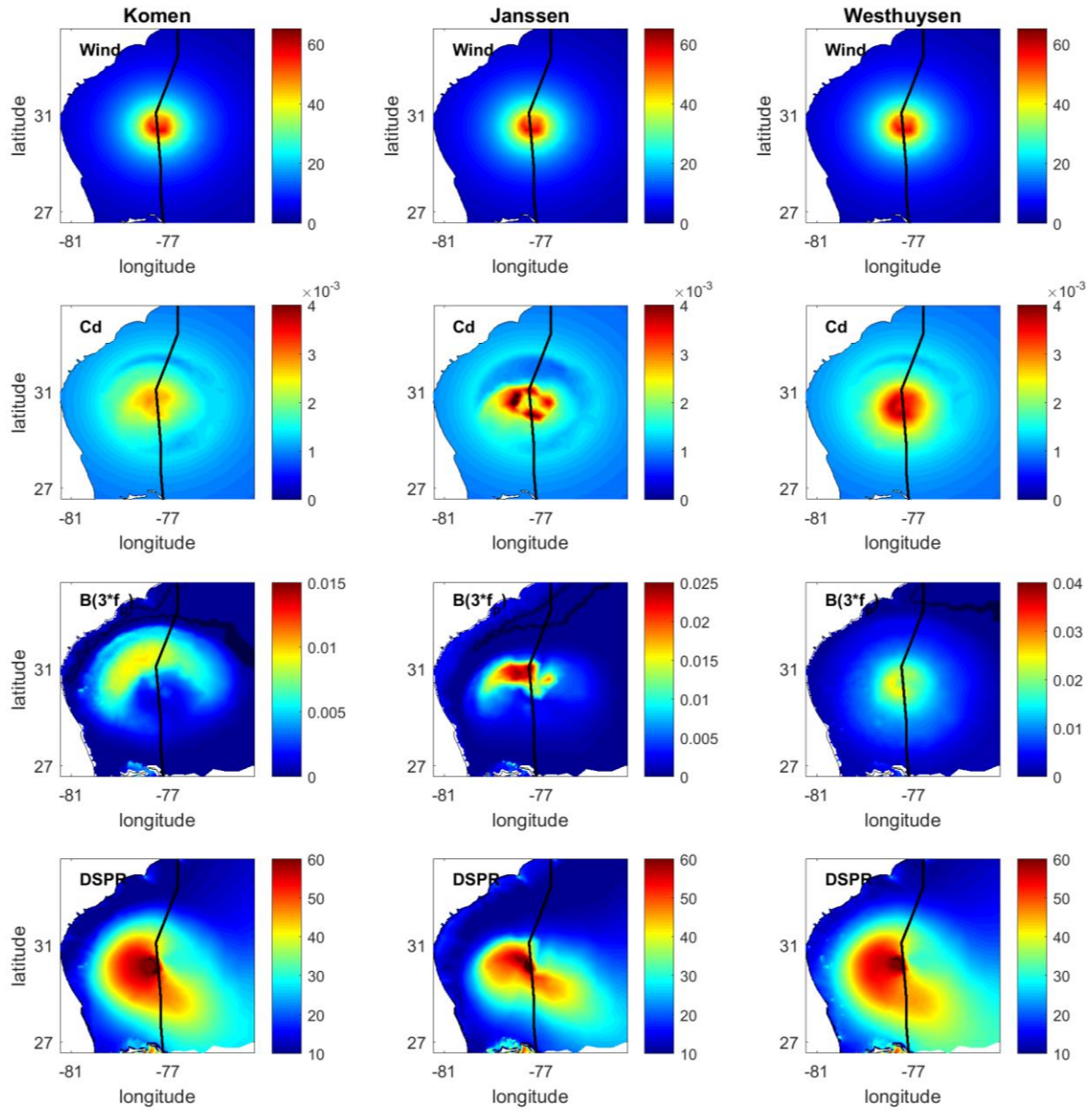


Figure 3.16. Same as Figure 3.22, but for the extended tail option at 08/26/2011 00:00 UTC

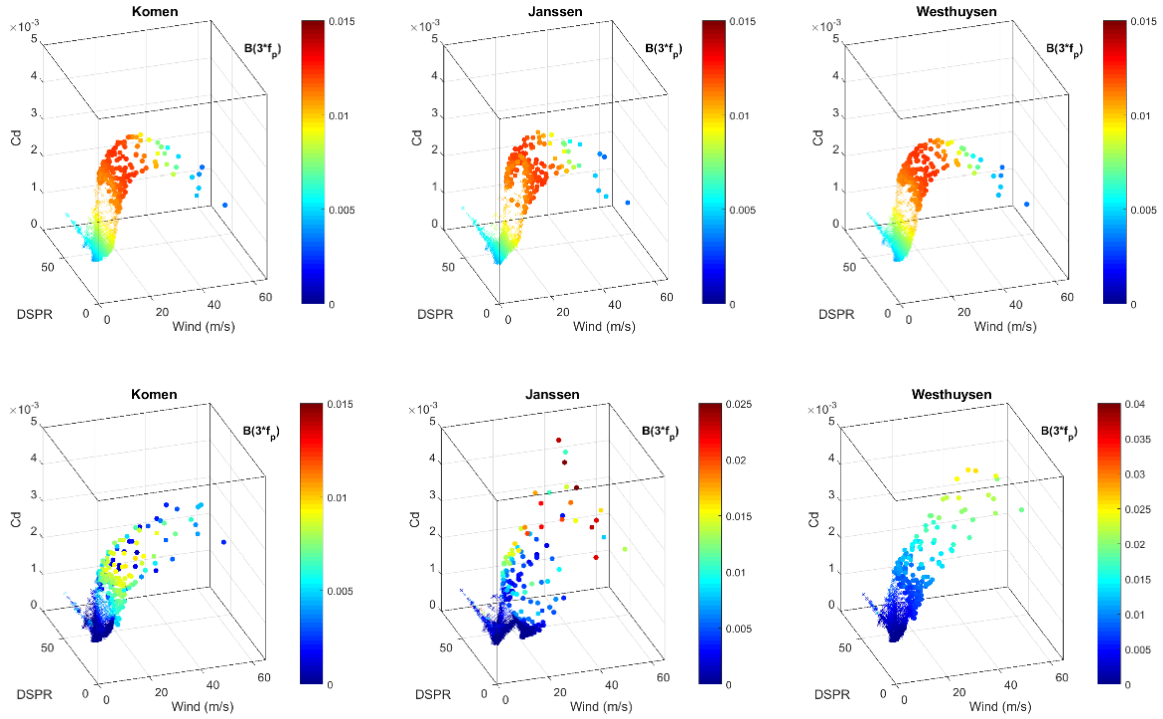


Figure 3.17. 3D plot of Wind (x), DSPR (y),  $C_d$  (z) and Saturation level B (color) for Reichl's empirical tail option (upper panel)) and the extended tail (lower panel)) at 08/26/2011 00:00 UTC

### Shallow Water

Model results at 08/27/2011 00:06 UTC are also examined to study the behavior of the DCCM  $C_d$  in shallow water. Similarly, spatial comparisons of the wind speed,  $C_d$ ,  $B$ , and DSPR are given for both the empirical tail option and extended tail option among Komen, Janssen, and Westhuysen.

When using Reichl's empirical saturation tail (Figure 3.18), behavior of  $C_d$  in shallow water is similar to that in deep water, although a larger spread of  $C_d$  can be observed for Janssen especially at wind speeds higher than 40m/s. We speculate that the large spread is due to Janssen's inconsistent performance in shallow water, but the exact reason to that inconsistency is unknown. When using the extended tail (Figure 3.19), behavior of  $C_d$  is much more problematic in shallow water. The main concern is the unrealistically high saturation tail level attached at  $3 \times$

$f_p$ , especially for Westhuysen. Also, saturation “hotspots” develop under the lower left quadrant of the storm as hurricane slowly approaching shore, which is rather puzzling. It is possible that a  $k^{-4}$  tail that is commonly used for deep water waves is no longer suitable for shallow water waves.

Comparison among wind speed,  $B$ ,  $C_d$  and DSPR for different tail options is also given for shallow water conditions (Figure 3.20). The differences in the distribution of  $C_d$  between the two tail options are more evident. Again, no strong correlation between DSPR and  $B$ , or DSPR and  $C_d$  are found. For Reichl’s empirical tail option,  $C_d$  behaves similarly among different physics packages, while the extended tail option produces very high  $C_d$  at high wind speeds.



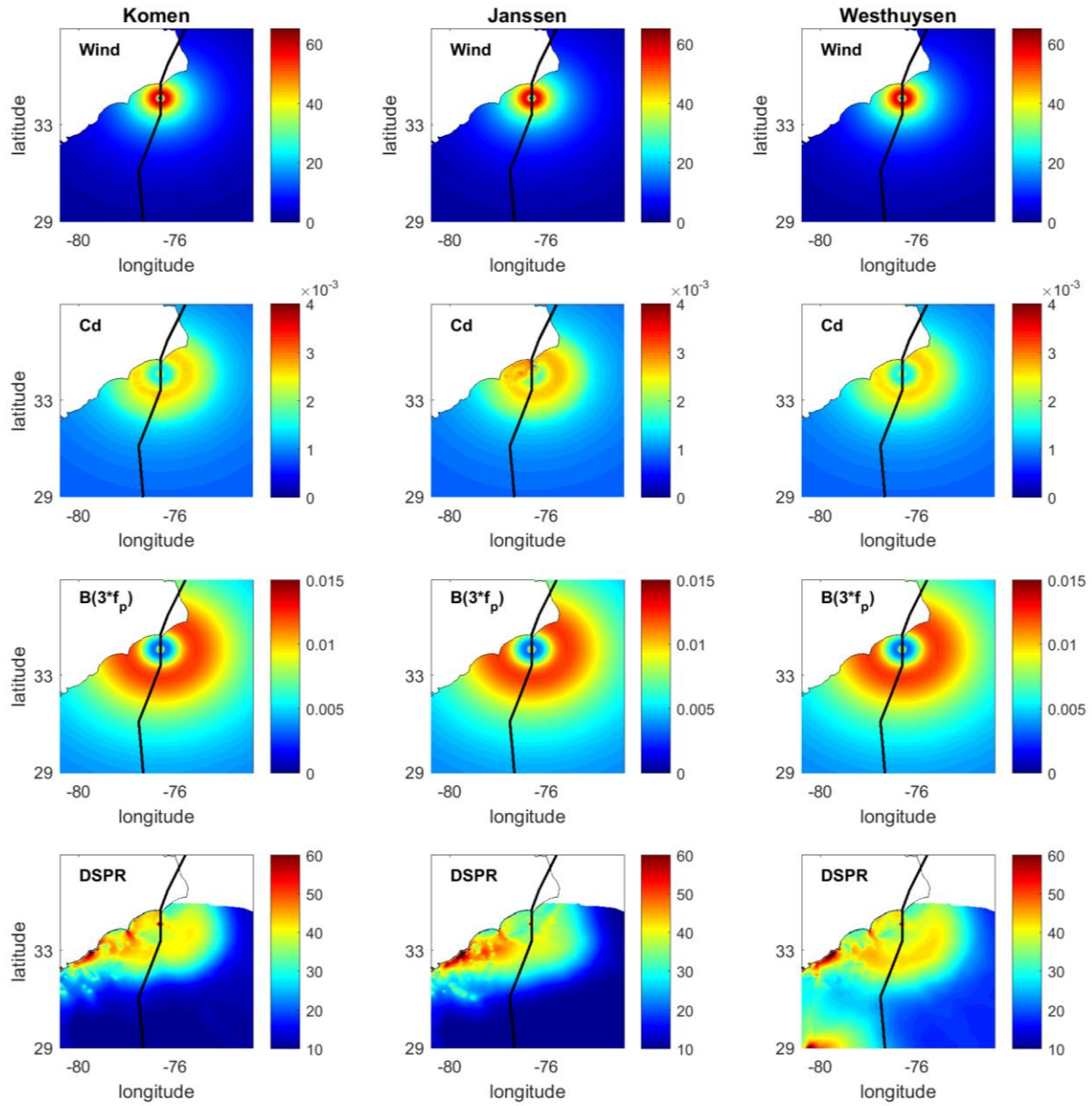


Figure 3.18. Same as Figure 3.15 for Reichl's empirical tail option, but for shallow water at 08/26/2011 00:00 UTC

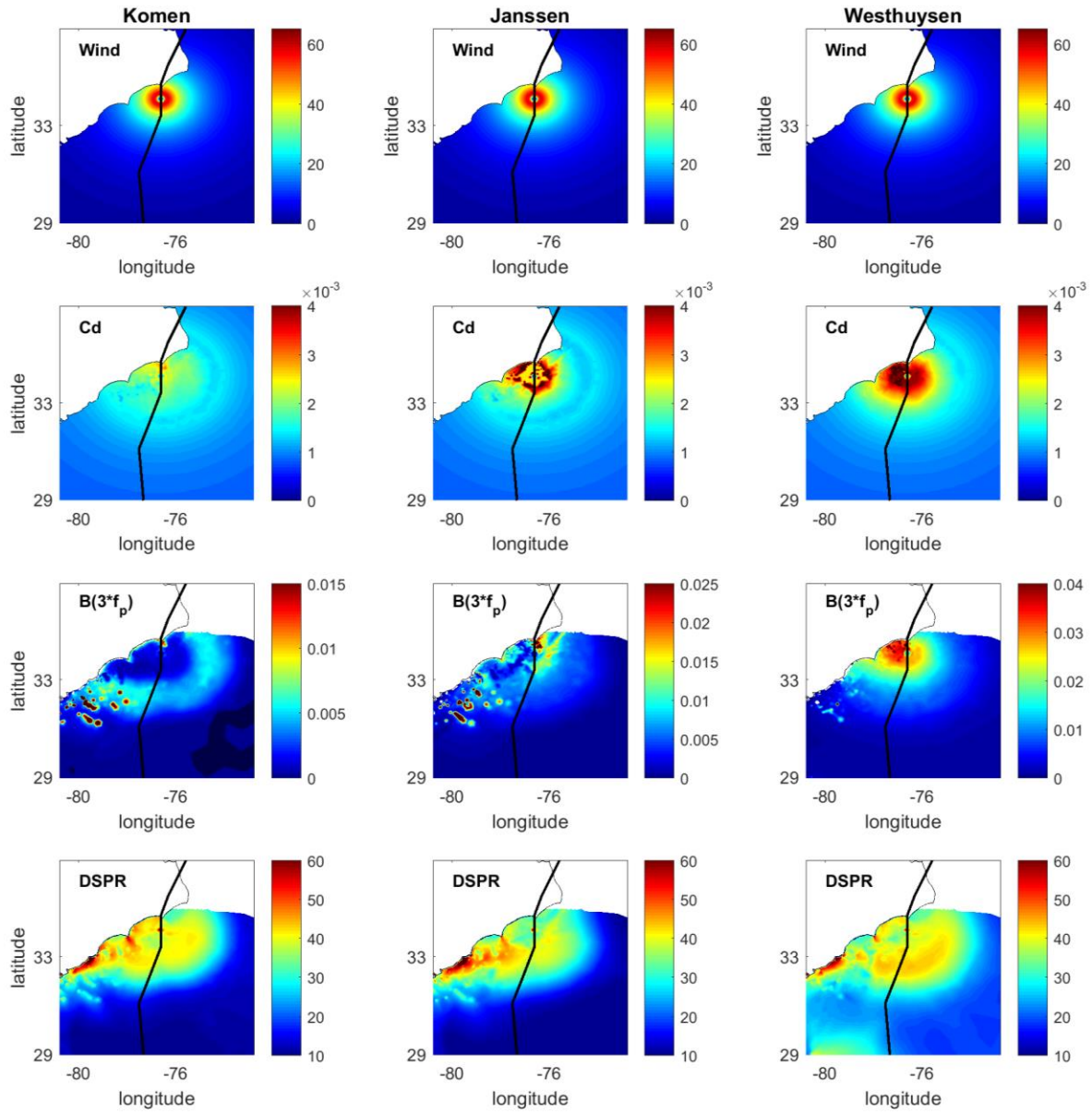


Figure 3.19. Same as Figure 3.16 for the extended tail option, but for shallow water at 08/26/2011 00:00 UTC

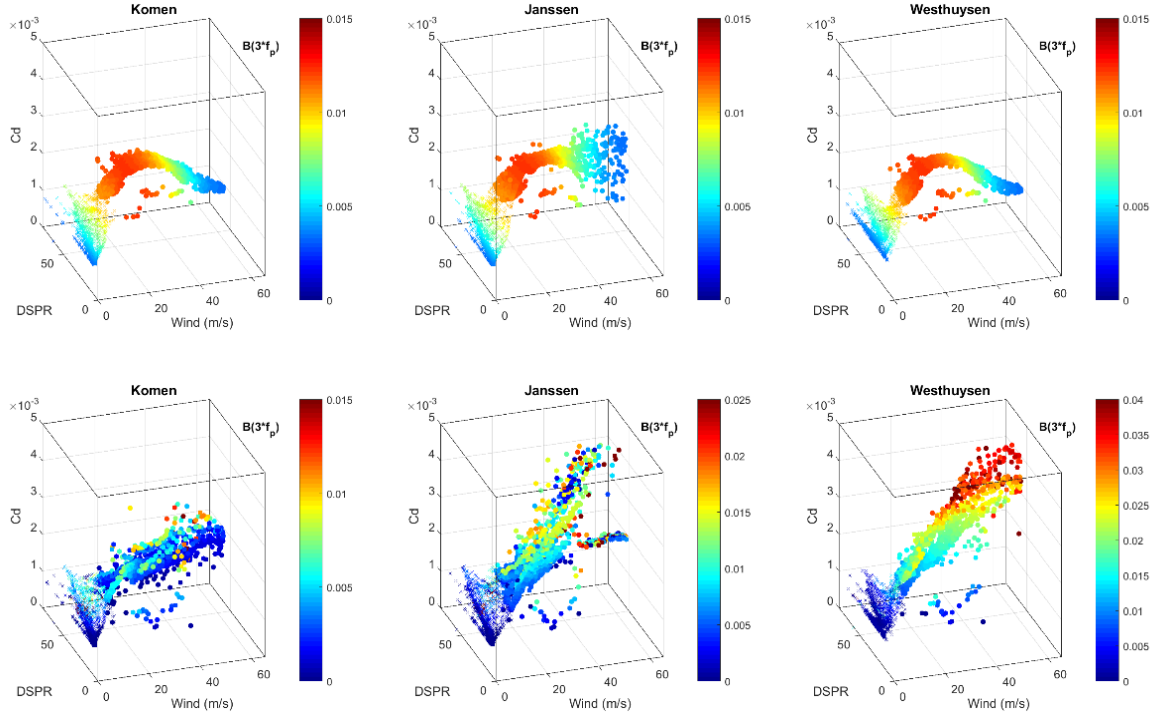


Figure 3.20. Same as Figure 3.17, but for shallow water at 08/27/2011 06:00 UTC

### 3.3.4 Summary and Conclusions

Sensitivity study of the explicit sea state dependent stress by DCCM on SWAN's prognostic wave spectrum and the attached diagnostic tail was carried out in this section. We started by comparing the resolved wave spectrum and its corresponding saturation spectrum among different physics packages, and for wave spectra attached with either Reichl's empirical tail or the extended tail. We found that the saturation tail levels of the extended tail can be quite different than those of the empirical tail, especially for wave field under a transient weather system. We then demonstrated the integration of  $\tau_{wave}$  for different tail options. We found that the saturation tail level plays a big role in determining the integrated wave form stress, and the contribution of the tail to the total integrated stress vary greatly depending on the tails attached. A general rule of thumb is that a higher saturation level will result a higher integrated  $\tau_{wave}$  and

a higher contribution of the tail to the total integrated stress. The resolved part of the spectrum does contribute to the total  $\tau_{wave}$ , however the influence can be relatively small depending on the level of the saturation tail. Last but not least, we compared the spatial distribution of  $B$  and  $C_d$  between two tail options in both deep and shallow water. With Reichl's empirical tail, behavior of  $C_d$  is quite consistent among different physics packages for both deep and shallow water conditions. The extended tail option is rather problematic at producing reasonable  $C_d$  at high wind speeds, especially for shallow water. It is possible that a  $k^{-4}$  tail that is commonly used for deep water is no longer suitable for shallow water, in which further research is needed. Reichl's empirical tail is recommended to use in both RHG and DCCM for consistent performances.

### **3.4. Storm Surge Study using Different Drag Laws**

In this section, effects of different surface drag laws (Table 3.1) on storm surge predictions are investigated using Hurricane Irene 2011. The GAHM is used to reconstruct Irene's wind and pressure fields based on its best track issued by the NHC, and the following eight different drag laws are used to force ADCIRC for storm surge predictions: Garratt, GFDL14, Powell, Swell (Ho12). RHG, DCCM, Wave Age (D03) and Wave Steepness (YT01). Model results at two snapshots, 08/26/2011 00:00:00 UTC and 08/27/2011 06:00:00 UTC, are examined to cover both deep and shallow water conditions.

#### **3.4.1 Drag Comparison among Different Methods**

Spatial plots of the wind speed,  $C_d$  from DCCM, water elevation, and a few wave parameters such as wave age (inversed), wave steepness, and significant wave height are given at 08/26/2011 00:00 UTC (Figure 3.21). Under a translating hurricane, relatively older and higher

waves can be observed in the front-right sector of the storm, while younger and steeper waves in the rear-left sector. Figure 3.22 gives the spatial comparison of  $C_d$  among different drag laws and Figure 3.23 plots  $C_d$  as a function of wind speed. It is found that  $C_d$  behaves quite differently among different methods, although resemblances in  $C_d$  distribution can be found between Garratt and GFDL14, Powell and Ho12, RHG and DCCM, D03 and TY01. Garratt's  $2.5 \times 10^{-3}$  cap acts like the leveling off behavior of GFDL14 (although no decreasing at even higher wind speed); Powell's sector-based drag law mimics the effect of different swell types in Ho12; both RHG and DCCM use Reichl's empirical tail option so they behave similarly; wave age and wave steepness are interconnected wave parameters, and both D03 and YT01 overestimate  $C_d$  at high wind speeds since their formula were derived under low to moderate winds. Note, although  $C_d$  in both RHG and DCCM is tuned to fit the GFDL14 drag law, spatial plots of  $C_d$  reveal that the RHG and DCCM have a much broader spatial distribution of  $C_d$  than that of the GFDL14, and may have very different storm surge results.

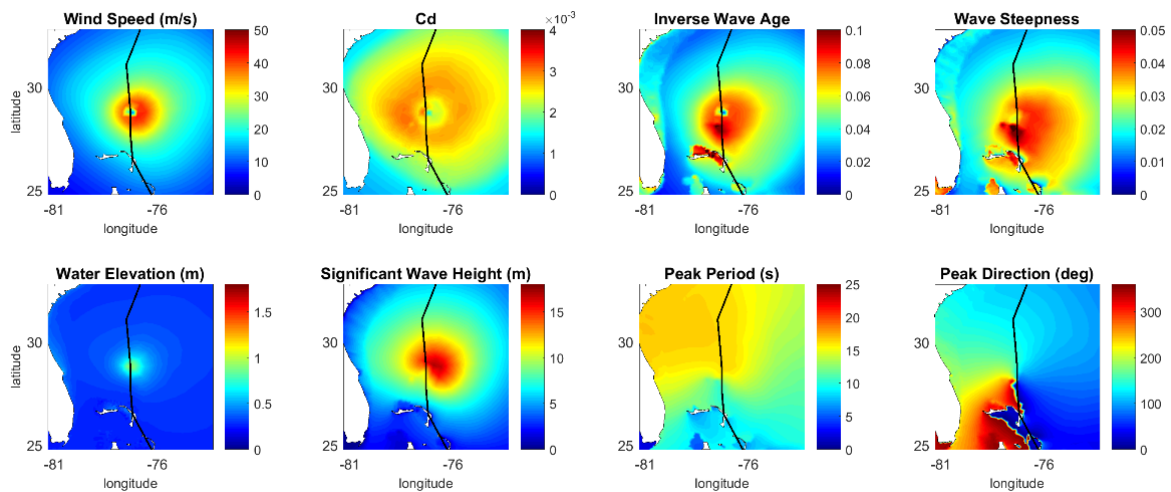


Figure 3.21. Spatial plots of the wind speed,  $C_d$  from DCCM, water elevation and a few wave for the deep water condition at 08/26/2011 00:00:00 UTC.

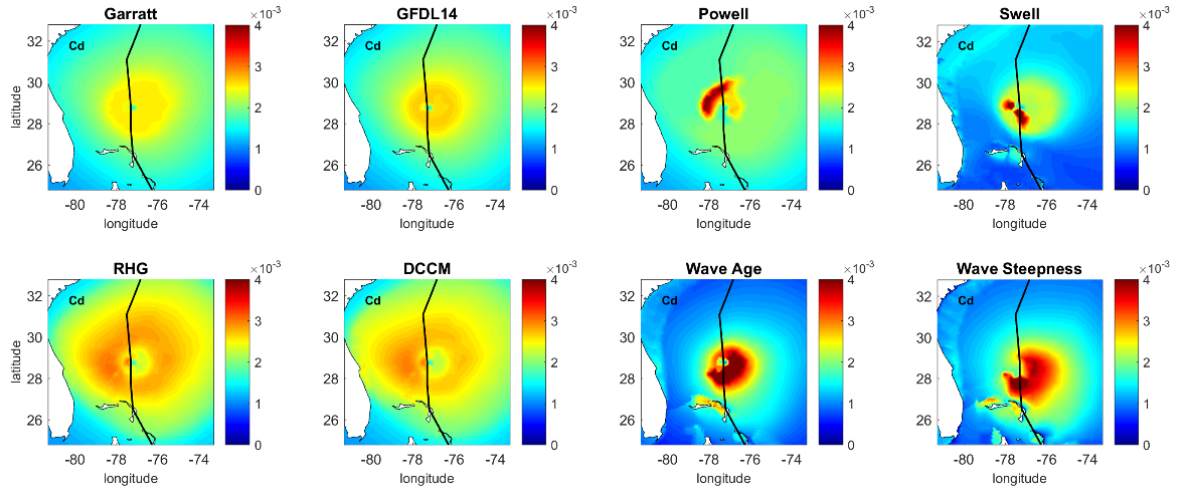


Figure 3.22. Spatial distribution of  $C_d$  among different drag laws at 08/26/2011 00:00:00 UTC. Upper panels from left to right: Garratt, GFDL14, Powell, Swell (Ho12). Lower panels from left to right: RHG, DCCM, Wave Age (D03) and Wave Steepness (YT01).

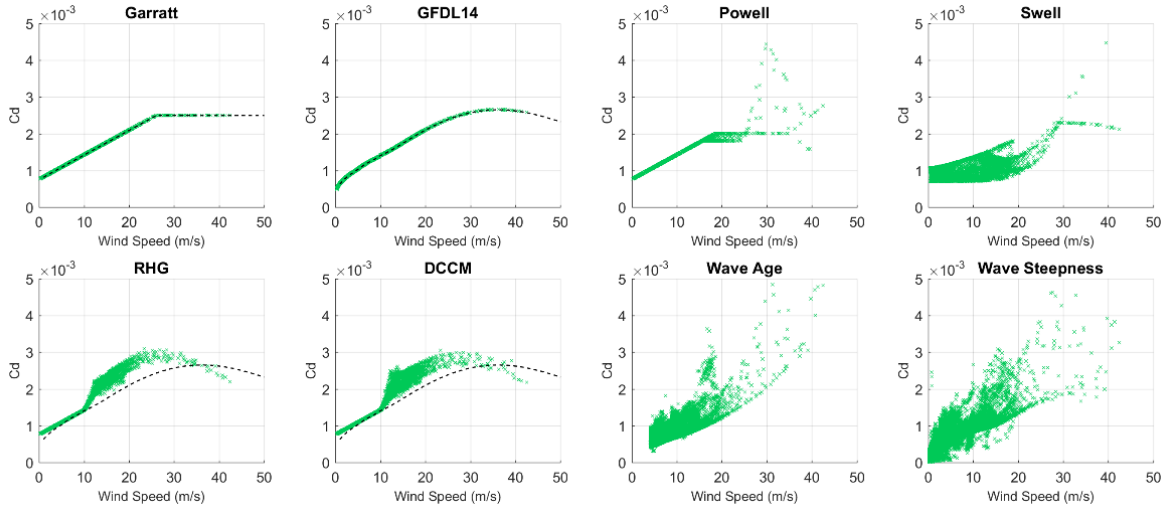


Figure 3.23. Comparison of  $C_d$  as a function of wind speed at 08/26/2011 00:00:00 UTC.

Spatial plots of wind speed,  $C_d$  from DCCM, water elevation, and a few wave parameters are also given at 08/27/2011 06:00:00 UTC when Irene is approaching shore (Figure 3.31).

Correspondingly, spatial comparison of  $C_d$  (Figure 3.32) and  $C_d$  as a function of wind speed

(Figure 3.33) among different drag laws are also given. Again, the Garratt and GFDL14 bulk drag laws share similarities in the behavior of  $C_d$ , and RHG and DCCM with the same empirical tail do too. However, discrepancies between Powell and Swell, as well as between Wave Age and Wave Steepness, get larger in shallow water. As waves gradually transitioning from deep to shallow water, surface wave field becomes more and more complex. It is understandable if certain drag laws fail to yield reasonable drags, such as the Powell, as its three distinctive storm sectors observed in deep water may not be applicable to shallow water.

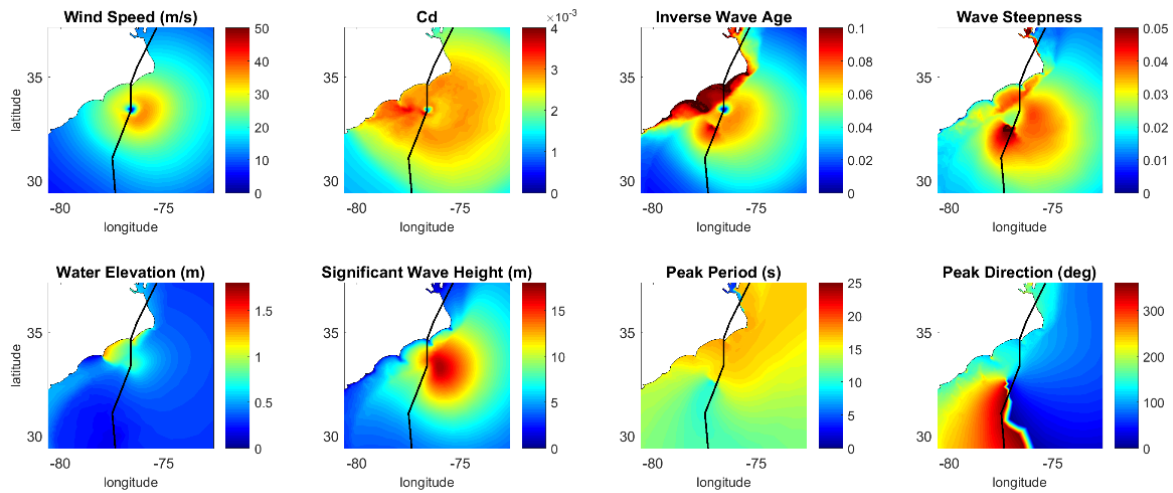


Figure 3.24. Same as Figure 3.21, but at 08/27/2011 06:00:00 UTC.



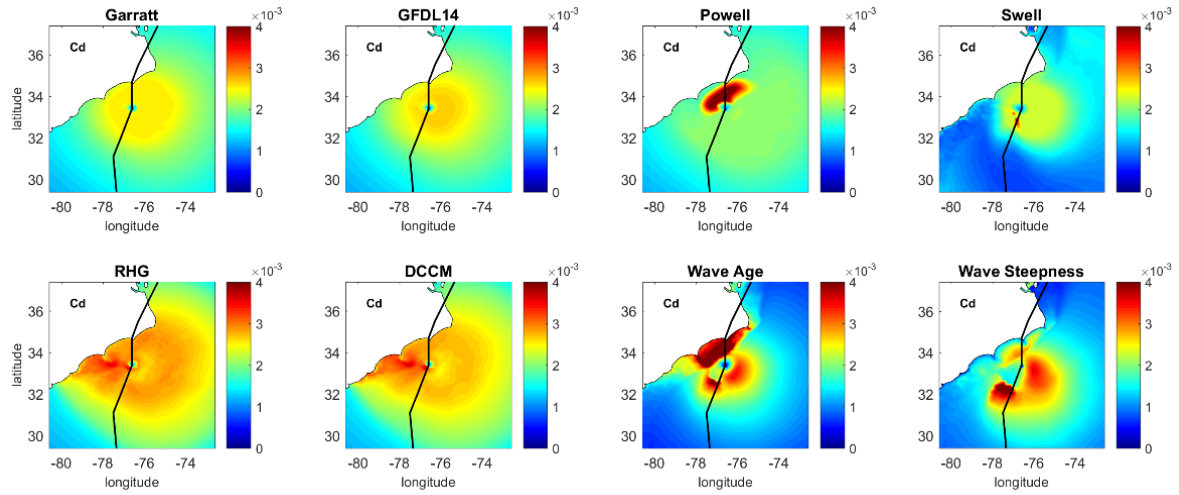


Figure 3.25. Same as Figure 3.22, but at 08/27/2011 06:00:00 UTC.

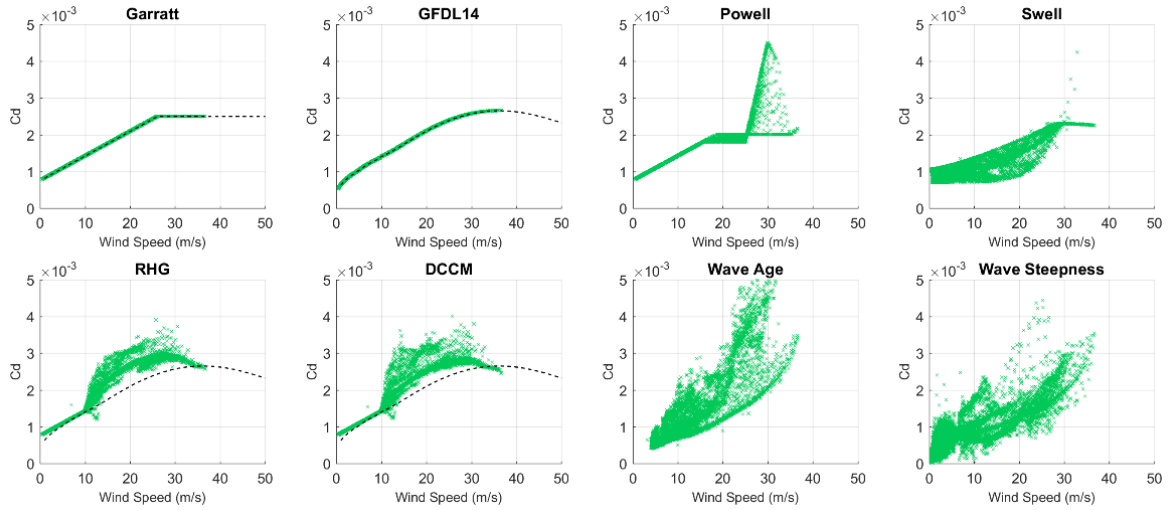


Figure 3.26. Same as Figure 3.23, but at 08/27/2011 06:00:00 UTC.

### 3.4.2 Influence on Storm Surge

Comparisons of  $C_d$  in the previous section suggest that different drag laws usually exhibit different spatial patterns but can also share similarities among a few. In this section, effect of



different drag laws on storm surge predictions is investigated. Figure 3.27 shows the spatial distribution of maximum water elevation from different drag laws. Using Garratt as the benchmark run, the differences in maximum water elevation between each drag law and Garratt is given in Figure 3.28 for easier comparisons. We can see that the surges from Garratt and GFDL14 have very similar spatial patterns, and the same happens between RHG and DCCM. The rest of the drag laws have very distinctive surge patterns, with both D03 and Powell over-predicting in large regions along shore, and YT01 and Ho12 under-predicting. The surge patterns are greatly influenced by the spatial patterns of  $C_d$  especially when storm approaching shore.

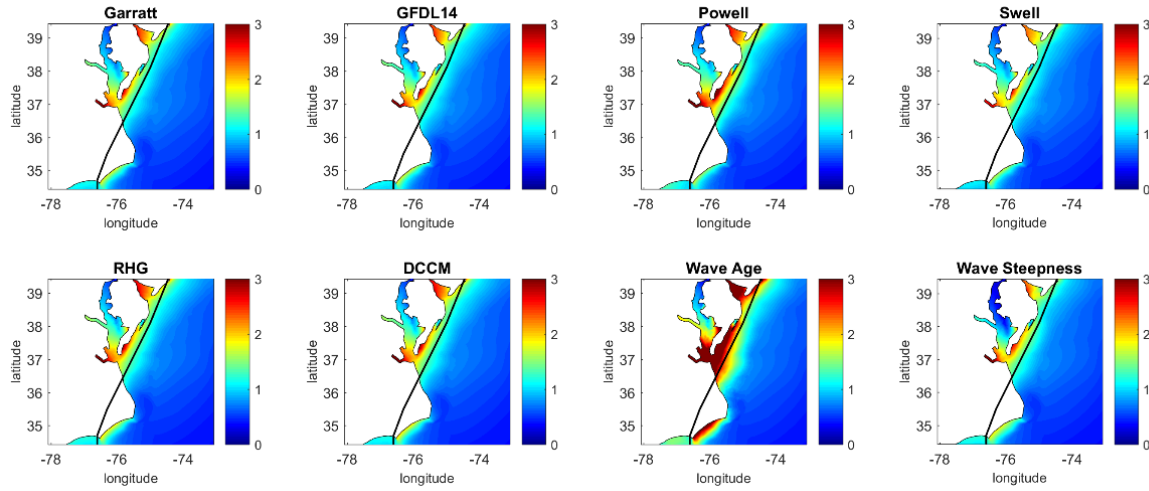


Figure 3.27. Spatial plot of Maximum water elevation resulted from different drag laws

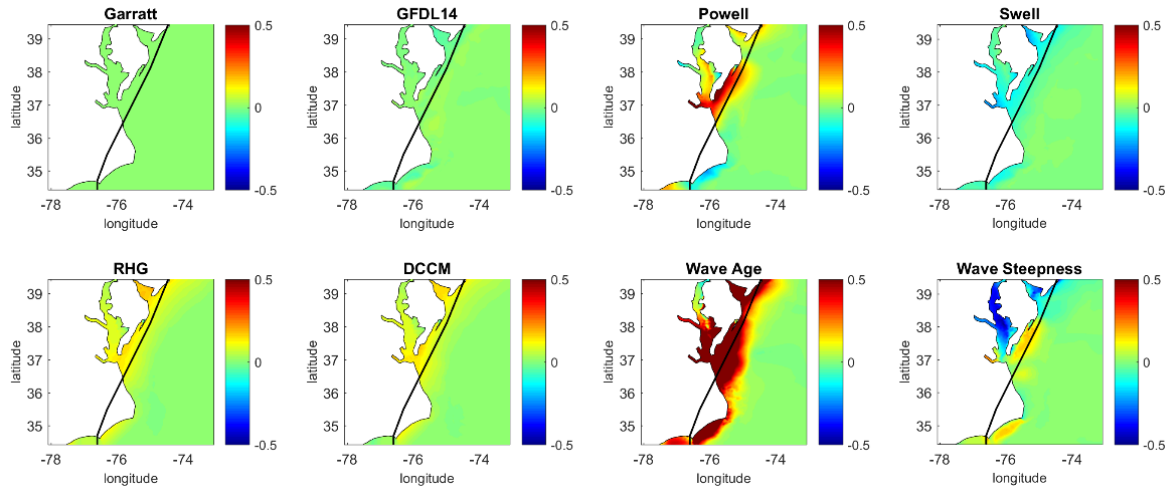


Figure 3.28. Using Garratt as bench mark, Maximum water elevation from different drag laws relative to Garratt

### 3.4.3 Summary and Conclusions

Effects of different surface drag laws on storm surge predictions were investigated using Hurricane Irene 2011 in this section. We compared the spatial patterns of  $C_d$  among different drag laws, and found that while each drag law has its own characteristics, similarities can be found among a few. Reichl's empirical tail was used in both RHG and DCCM as it provides a more consistent model performance. When using Reichl's empirical tail option, little sea state dependency of  $C_d$  were found in RHG and DCCM, which contradicts the findings by Powell and Ho12. There could be a few explanations: 1) in the resolved part of the spectrum, influence of different types of swell (following, crossing, or opposing) on the surface wind stress is under-addressed; 2) the use of a wind speed-dependent spectral tail is inadequate as it does not contribute to sea state dependency of  $C_d$ , and 3) important physics such as wave breaking and sea spray are missing from this surface stress formulation. Thus, assumptions in RHG and DCCM need to be re-examined. Also, as theories invoked in RHG and DCCM are developed

under assumption of deep water and high winds (Reichl et al., 2014; Ginis et al., 2015), adaptations for shallow water applications should be re-visited in the future.

We also examined the effect of different drags on storm surge predictions. Compared to the bulk drag laws, both RHG and DCCM showed a small degree of sea state dependency, but not enough to produce drastically different surge results. The main take-home message from this section is that the spatial pattern of  $C_d$  plays a big role on coastal storm surge predictions. In another word, information of  $C_d$  as a function of wind speed only is not enough.

## CHAPTER 4: DISCUSSION AND CONCLUSIONS

### 4.1 Discussion on the GAHM

This section describes the development of a Generalized Asymmetric Holland Model (GAHM) based on the classic HM for operational storm surge forecasting. In the past, storm surge modelers had found that the classic HM sometimes failed to represent the wind and pressure fields for a large but weak storms. A closer examination of the HM's formulation revealed that the cyclostrophic balance assumption made at the RMW during the derivation of the Holland B parameter is not valid under certain circumstances. More specifically, cyclostrophic balance assumption should only be made when the Rossby number ( $R_o$ , which is a dimensionless number relating the ratio of nonlinear accelerations to the Coriolis force) at the RMW is large enough that the Coriolis term can be dropped. So the purpose was to remove the cyclostrophic balance assumption at the RMW, and re-derive the radial wind and pressure profiles using the full gradient wind equation. A modified expression of  $B$  was obtained, referred to as  $B_g$ , together with a new parameter introduced, the scaling factor  $\varphi$ . The generalized equations now can be used for a wide range of TCs without suffering from systematic errors associated with a small  $R_o$  as the HM does. This is a huge improvement of the GAHM over the classic HM, especially for storms with  $\log_{10} R_o < 1$ . Another important feature of the GAHM is the introduction of the composite wind method, which allows the GAHM to use up to three storm isotachs in the forecast or best track to reconstruct wind and

pressure fields during active storms.

Performance of the GAHM was evaluated using seven selected hurricanes that struck the U.S. East Coast and the Gulf of Mexico in the past decades. Comparison between given isotachs and the modeled winds at distances to those isotachs suggested that the GAHM was able to consistently produce surface wind fields that match the NHC's advisory data. Comparison between the GAHM winds and the OWI and H\*Wind indicated the GAHM is still in lack of many details of a hurricane, however, it is a good candidate for timely forecast use.

As a prototype for parametric wind forecasting, the GAHM was designed to interpret storm information in NHC's forecast or best track advisories to construct a composite wind field for a wide range of TCs. In theory, wind observations made anywhere within the influential range of a hurricane could be synthesized into the final product by the parametric wind model. Future work is proposed to improve the GAHM so that it can assimilate wind data from other sources to yield better representation of the hurricane wind fields.

## **4.2 Discussion on Surface Wind Stress and Storm Surge Modeling**

This section discusses the surface wind stress for storm surge modeling. As storm surge modelers, we are mostly concerned with coastal storm surge induced by landfalling hurricanes. Many approaches have been developed to estimate the surface wind stress  $\vec{\tau}$  over the past few decades, however, results are far from conclusive. In this study, we implemented a few sea state dependent stress formulations to the coupled ADCIRC+SWAN to examine their influences on storm surge predictions. Recognizing possible similarities and differences among different surface drag laws and identifying their limitations is the first step towards further application in coastal storm surge modeling.

Garratt's wind speed-dependent, D03's wave age-dependent, and TY01's wave steepness-dependent formulas were derived from measurements at low to moderate wind speeds. To use these empirical formulas at hurricane wind speeds,  $C_d$  values are simply extrapolated and sometimes can reach unreasonably large values. A cap value must be applied to avoid overestimation of  $C_d$  at high wind speeds, which is not ideal.

D03 and TY01 use statistically-derived formulas to relate the sea surface roughness  $z_0$  to statistical wave parameters, the wave age and wave steepness, respectively. However, their performances vary with sea states. Drennan et al. (2005) found that

- Both methods yielded reasonable results of  $z_0$  for systems dominated by wind sea
- D03 was preferred for undeveloped “young” wind sea
- TY01 was favored for general mixed seas
- Both two methods failed to provide adequate representation of  $z_0$  for systems dominated with swell

Thus, D03 and TY01 cannot be universally applied for varies wind and wave regimes.

The Powell's storm sector- and Holthuijsen's (Ho12) wave directional spreading-dependent formulas were derived from GPS dropsonde data under hurricane wind forcing in deep water open ocean conditions. Both of them categorize different swell types of the surface wave field around the storm center and yield azimuthally-varying  $C_d$  as a function of wind speed, with the Ho12 being more sophisticated. Compared to previous studies, Powell and Holthuijsen's controversial results provide insight into our understanding of the sea state-dependent surface roughness under hurricane vortex winds.

The 2D wave spectrum-dependent surface stress formulas, RHG and DCCM, show the most promise for general application, although physics are not included to explicitly account for the impacts of breaking-wave, sea spray and air-flow separation on the surface roughness. Both RHG and DCCM compute the wave-induced form stress by integrating the momentum flux into waves over the entire frequency/wavenumber range. Since wave models such as SWAN and WWIII can only resolve wave spectrum up to 3 times the peak frequency, a spectral tail needs to be attached at the high frequency equilibrium range. Reichl et al. (2014) found that the surface stress is very sensitive to the value of the saturation tail level  $B$ . However, very few direct measurements of  $B$  exist under hurricane winds and its dependence on wind speed or wave age (or possibly other parameters) remains unclear. If the saturation level is taken to be a function of wind speed, wave age, or both, then the drag coefficient can be constructed to match any given observations or empirical parameterizations.

In this study, two major experiments were conducted. The first experiment involved sensitivity test of the explicit sea state dependent drag to both prognostic wave spectrum and the diagnostic spectral tail. Two different saturation tails were examined, the well-tuned empirical one, and a more rudimentary extended one with a  $k^{-4}$  slope and saturation tail level of that computed at  $3 \times f_p$  of the modeled spectrum. The most important finding of this study is that the drag coefficient is very sensitive to the spectral saturation level but is not as sensitive to the resolved part of the spectrum. For both tail options, it was found that the computed  $C_d$  as well as the contribution of the tail to the total  $C_d$  depend greatly on the saturation tail level specified. The extended tail option yields interesting results in deep water, but is rather problematic in shallow water. It is speculated that the  $k^{-4}$  spectral tail commonly used for deep water condition might not be suitable for shallow water condition. Although the drag coefficient is not very sensitive to

the prognostic wave field, it still introduces certain sea state dependency of  $C_d$  compared to the bulk formula. Depending on the physics packages used in SWAN, the 2D wave spectrum simulated will be slightly different, and the stress computed in DCCM and RHG will slightly differ from each other. Thus, it is important to be aware of a) saturation tail option used and b) the wave physics packages used when computing the explicit sea state dependent drag using RHG and DCCM.

The main take-home message from this experiment is that: 1) wave dependent stress is indeed very sensitive to the specification of the spectral tail; 2) the resolved wave spectrum introduces sea state dependency to  $C_d$ , and is responsible for any misalignment between the total stress and the wind vector by taking into account the effect of opposing and crossing wind swells; 3) if as suspected that  $C_d$  in coastal water is larger than in deep water, then the empirical tail that's derived under deep water conditions has to be tailored for shallow water application, but more observational and theoretical studies of surface drags in coastal water is needed. Although the explicit wave dependent stress formula is flawed at the moment, it still has merits that other bulk drag formula don't.

Last but not least, we studied the effect of different drag laws on storm surge predictions using Hurricane Irene (2011) as a study case. The eight selected drag laws as discussed earlier were used to force the couple ADCIRC+SWAN model, and the maximum elevation were examined. Results suggested that different drag laws show distinctive spatial patterns although a few share similarities. Also the surge patterns are closely related to the spatial patterns of different drag laws. In the future, it is recommended to use real observational data to quantify the behavior of each drag law.



## REFERENCES

- Battjes, J. A., 1972: Radiation stresses in short-crested waves, *J. Mar. Res.*, 30(1), 56–64.
- Black, P. G., E. A. D’Asaro, W. M. Drennan, J. R. French, P. P. Niiler, T. B. Sanford, E. J. Terrill, E. J. Walsh, J. A. Zhang, 2007: Air-sea exchange in hurricanes - Synthesis of observations from the coupled boundary layer air-sea transfer experiment. *Bulletin of the American Meteorological Society*, 88(3) 357-374.
- Dietrich, C., 2010: Wind Drag Based on Storm Sectors. <https://ccht.ccee.ncsu.edu/wind-drag-based-on-storm-sectors/>
- Chalikov, D. V., and V. K. Makin, 1991: Models of the wave boundary layer. *Bound-Layer Meteor.*, 56, 83-99.
- Charnock, J., 1955, Wind stress on a water surface. *Quart. J. Roy. Meteor. Soc.*, 81, 639-640.
- Donelan, M. A., J. Hamilton, and W. H. Hui, 1985: Directional spectra of wind-generated waves. *Phil. Trans. Roy. Soc. London*, A315, 509-562.
- Donelan, M. A., F.W. Dobson, S. D. Smith, , and R. J. Anderson, 1993: On the dependence of sea surface roughness on wave development. *J. Phys. Oceanogr.*, 23, 2143–2149.
- Donelan, M. A., B. K. Haus, N. Ruel, W. J. Stianssnie, H. C. Graber, O. B. Brown, and E. S. Saltzman, 2004: On the limiting aerodynamic roughness of the ocean in very strong winds. *Geophys. Res. Lett.*, 31, L18306.
- Donelan, M. A., M. Curcic, S. S. Chen, and A. K. Magnusson, 2012: Modeling waves and wind stress, *J. Geophys. Res.*, 117, C00J23, doi: 10.1029/2011JC007787.
- Drennan, W. M., H. C. Graber, D. Hauser, and C. Quentin, 2003: On the wave age dependence of wind stress over pure wind seas. *J. Geophys. Res.*, 108, 8062.
- Drennan, W. M., Taylor, P. K., & Yelland, M. J. (2005). Parameterizing the sea surface roughness. *J. PHYSICAL OCEANOGRAPHY*, 35(5), 835-848.  
<https://doi.org/10.1175/JPO2704.1>
- Edson et al., 2013: On the Exchange of Momentum over the Open Ocean, *J. Phys. Oceanogr.*, 43, 1589-2590, doi:10.1175/JPO-D-12-0173.1.
- Fan, Y., I. Ginis, and T. Hara, 2010: Momentum flux budget across the air-sea interface under tropical cyclone winds. *J. Phys. Oceanogr.*, 40, 2221-2242, DOI: 10.1175/2010JPO4299.1.
- Garratt, J. R., 1977, Review of drag coefficients over oceans and continents. *Mon. Wea. Rev.*, 105, 915-919.
- Geernaert, G. L., K. B. Katsaros, and K. Richter, 1986, Variation of the drag coefficient and its dependence on sea state. *J. Geophys. Res.*, 91, 7667-7679.

- Georgiou, P., 1985: Design wind speeds in tropical cyclone prone regions. Ph.D. thesis, University of Western Ontario, 295 pp.
- Isaac Ginis, University of Rhode Island, Narragansett, RI; and M. A. Bender, B. Thomas, M. J. Morin, V. Tallapragada, and A. V. Soloviev, 2015: A New Drag Coefficient Formulation and its Impact on the GFDL and HWRF Hurricane Model Predictions. 19th Conference on Air-Sea Interaction, <https://ams.confex.com/ams/95Annual/webprogram/Paper268750.html>
- Hara, T., and S. E. Belcher, 2004: Wind profile and drag coefficient over mature ocean surface wave spectra, *J. Phys. Oceanogr.*, 34, 2345-2358.
- Hasselmann, K., Barnett, T. P., Bouws, E., Carlson, H., Cartright, D. E., Enke, K., Ewing, J. A., Gienapp, H., Hasselmann, D. E., Meerburg, A., Muller, P., Olbers, D. J., Richter, K., Sell, W., and Walden, H., 1973, Measurements of wind-wave growth and swell decay during the Joint Sea Wave Project (JONSWAP), *Disch. Hydrog. Ze. 80, (Suppl. A)*, N12, 95 pp.
- Holland, G. J., 1980: An analytic model of the wind and pressure profiles in hurricanes. *Monthly Weather Review*, 108, 1212-1218.
- Holland, G. J., 2008: A revised hurricane pressure-wind model. *Monthly Weather Review*, 136, 3432-3445.
- Holthuijsen, L. H., 2007, Waves in Oceanic and Coastal Water, *Cambridge University Press*.
- Holthuijsen, L. H., M. D. Powell, and J. D. Pietrzak (2012), Wind and waves in extreme hurricanes, *J. Geophys. Res.*, 117, C09003, doi: 10.1029/2012JC007983.
- Houston, S.H.; Shaffer, W.A.; Powell, M.D., 1999: Comparisons of HRD and SLOSH surface wind fields in hurricanes: Implications for storm surge modeling. *Weather Forecast*, 14, 671–686.
- Hsu, S. A., 1974: A dynamic roughness equation and its application to wind stress determination at the air-sea interface. *J. Phys. Oceanogr.*, 4, 116–120.
- Hwang, P. A., D. W. Wang, E. J. Walsh, W. B. Krabill and R. N. Swift, 2000, Airborne measurements of the wave number spectra of ocean surface waves. Part I: Spectral slope and dimensionless spectral coefficient, *J. Phys. Oceanogr.*, 30, 11, 2753–2767.
- Hu, K., Q. Chen, and P. Fitzpatrick, 2012: Assessment of a Parametric Hurricane Surface Wind Model for Tropical Cyclones in the Gulf of Mexico. *InTech*, <http://dx.doi.org/10.5772/51288>.
- Hu, K., Q. Chen, and S. K. Kimball, 2012: Consistency in hurricane surface wind forecasting: an improved parametric model. *Nature Hazards*, 61, 1029-1050.
- Jarosz, E., D. A. Mitchell, D. W. Wang, and W. J. Teague, 2007: Bottomup determination of air-sea momentum exchange under a major tropical cyclone, *Science*, 315, 1707–1709, doi:10.1126/science.1136466.

- Janssen, P. A. E. M., 1989: Wave-induced stress and the drag of airflow over sea waves. *J. Phys. Oceanogr.*, 19, 745-754.
- Janssen, P. A. E. M., 1991: Quasi-linear theory of wind-wave generation applied to wave forecasting, *J. Phys. Oceanogr.*, 21, 1631-1642
- Jelesnianski, C.P., J. Chen, and W. A. Shaffer, 1992: SLOSH: sea, lake, and overland surges from hurricanes. *National Weather Service*, Silver Springs, MD.
- Kenney, B. C., 1982: Beware of spurious self-correlations!, *Water Resour. Resea.* Vol. 18, No. 4, Pages 1041-1048.
- Komen, G.J., Hasselmann, S., Hasselmann, K., 1984. On the existence of a fully developed wind-sea spectrum. *J. Phys. Oceanogr.* 14, 1271–1285.
- Kitaigorodskii, S. A. and Y. A. Volkov, 1965: On the roughness parameter of the sea surface and the calculation of momentum flux in the near-water layer of the atmosphere. *Izv. Atmos. Oceanic Phys.*, 1, 973–988.
- Large, W. G., and S. Pond, 1981: Open ocean momentum flux measurements in moderate to strong winds. *J. Phys. Oceanogr.*, 11, 324–336.
- Lin, N., K. Emanuel, M. Oppenheimer, and E. Vanmarcke, 2012a: Physically based assessment of hurricane surge threat under climate change. *Nat. Climate Change*, 2, 462–467, doi:10.1038/nclimate1389.
- Lin, N., and D. Chavas, 2012b: On hurricane parametric wind and applications in storm surge modeling, *J. Geophys. Res.*, 117, D09120, doi:10.1029/2011JD017126.
- Luetich, R. A., J. J. Westerink, and N. W. Scheffner, 1991: ADCIRC: An advanced three-dimensional circulation model for shelves, coasts and estuaries; Report 1: Theory and methodology of ADCIRC-2DDI and ADCIRC-3DL, *Technical Report DRP-92-6*, Headquarters, U.S. Army Corps of Engineers, Washington DC.
- Luetich, R. A., J. J. Westerink, and N. W. Scheffner, 1992. ADCIRC: An advanced three-dimensional circulation model for shelves, coasts, and estuaries; Report 1, Theory and methodology of ADCIRC-2DDI and ADCIRC-3DL, Technical Report DRP-92-6, Vicksburg, MS: U.S. Army Engineer Waterways Experiment Station.
- Mattocks, C., C. Forbes, and L. Ran, 2006: Design and implementation of a real-time storm surge and flood forecasting capability for the State of North Carolina. *UNC-CEP Technical Report*, University of North Carolina, 103pp.
- Mattocks, C., and C. Forbes, 2008: A real-time, event-triggered storm surge forecasting system for the state of North Carolina. *Ocean Modelling*, 25, 95-119.
- Miles, J. W., 1957: On the generation of surface waves by shear flows, *J. Fluid Mech.*, 3, 185-204.

- Moon, I.-J., I. Ginis, and H. Tetsu, 2004: Effect of Surface Waves on Air–Sea Momentum Exchange. Part II: Behavior of Drag Coefficient under Tropical Cyclones
- National Oceanic and Atmospheric Administration, National Weather Service, National Centers for Environmental Prediction, National Hurricane Center. Automated Tropical Cyclone Forecast (ATCF) best track data, <ftp://ftp.tpc.ncep.noaa.gov/atcf/archive/>.
- Oost, W. A., G. J. Komen, C. M. J. Jacobs, and C. V. Oort, 2002: New evidence for a relation between wind stress and wave age from measurements during ASGAMAGE. *Bound.-Layer Meteor.*, 103, 409–438.
- Phillips 1958.
- Petersen, G. N., and I. A. Renfrew, 2009: Aircraft-based observations of air–sea fluxes over Denmark Strait and the Irminger Sea during high wind speed conditions. *Q. J. R. Meteorol. Soc.*, 135, 2030–2045.
- Phadke, A. C., C. D. Martino, K. F. Cheung, and S. H. Houston, 2003: Modeling of tropical cyclone winds and waves for emergency management. *Ocean Eng.*, 30, 553–578.
- Phillips, O., 1958: The equilibrium range in the spectrum of wind-generated waves. *Journal of Fluid Mechanics*, 4(4), 426–434. doi:10.1017/S0022112058000550
- Phillips, O. M., 1977: The dynamics of the upper ocean, *Camps. Univ. Press*.
- Pierson, W. J. and L. Moskowitz, 1964: A proposed spectral form for fully-developed wind seas based on the similarity law of S. A. Kitaigorodskii. *J. Geophys. Res.*, 69, 5181–5203.
- Powell, M. D., S. H. Houston, and T. Reinhold, 1996: Hurricane Andrew’s landfall in south Florida. Part I: Standardizing measurements for documentation of surface wind fields. *Wea. Forecasting*, 11, 304–328
- Powell, M. D., P. J. Vickery, and T. A. Reinhold, 2003: Reduced drag coefficient for high wind speeds in tropical cyclones. *Nature*, 422, 279–283.
- Powell, M. D., G. Soukup, S. Cocke, S. Gulati, N. Morisseau-Leroy, N. Dors, and L. Axe, 2005: State of Florida Hurricane Loss Projection Model: Atmospheric science component. *J. Wind Eng. Ind. Aerodyn.*, 93, 651–674.
- Powell, M. D., 2007: Final Report to the National Oceanic and Atmospheric Administration (NOAA) Joint Hurricane Testbed (JHT) Program. 26 pp.
- Powell, M. D., E. W. Uhlhorn, and J. D. Kepert, 2009: Estimating maximum surface winds from hurricane reconnaissance measurements. *Wea. Forecasting*, 24, 868–883.
- Queensland Government, 2011: Queensland Climate Change and Community Vulnerability to Tropical Cyclone, Ocean Hazards Assessment – Stage 1.
- Reichl, B. G., T. Hara, and I. Ginis, 2014: Sea state dependence of the wind stress over the ocean under hurricane winds, *J. Geophys. Res. Oceans.*, 119, 30–51, doi: 10.1002/2013JC009289

- Shapiro, L. J., 1983: The asymmetric boundary layer under a translating hurricane. *J. Atmos. Sci.*, 40, 1984–1998.
- Smith, S. D., 1980: Wind Stress and heat flux over the ocean in gale force winds. *J. Phys. Oceanogr.*, 5, 750–760.
- Smith, S. D., 1992: Sea surface wind stress and drag coefficients: The HEXOS results. *Bound. Layer Meteor.*, 60, 109–142.
- Soloviev, A., Lukas, R., Donelan, M., Haus, B., & Ginis, I., 2014: The air-sea interface and surface stress under tropical cyclones. *Nature Scientific Reports*, 4, 5306
- Taylor, P. K. and M. J. Yelland, 2001: The dependence of sea surface roughness on the height and steepness of the waves. *J. Phys. Oceanogr.*, 31, 572–590.
- Toba, Y., 1973: Local balance in the air-sea boundary processes, III. On the spectrum of wind waves. *J. Oceanogr. Soc. Japan*, 29, 209–220.
- Toba, Y., N. Lida, H. Kawamura, N. Ebuchi, and I. S. F. Jones, 1990: Wave dependence on sea-surface wind stress. *J. Phys. Oceanogr.*, 20, 705–721.
- Tolman, H. L., 2009: User manual and system documentation of WAVEWATCH III version 3.14, Tech. Note 276, NOAA/NWS/NCEP/EMC/MMAB, Camp Springs. [Available at [http://polar.ncep.noaa.gov/mmab/papers/tn276/MMAB\\_276.pdf](http://polar.ncep.noaa.gov/mmab/papers/tn276/MMAB_276.pdf).]
- Walsh, E. J., C. W. Wright, D. Vandemark, and W. B. Krabill, 2002: Hurricane directional wave spectrum spatial variation at landfall. *J. Physical Ocean.*, 32, 1667–1684.
- Van der Westhuysen, A.J., M. Zijlema and J.A. Battjes, 2007: Nonlinear saturation based whitcapping dissipation in SWAN for deep and shallow water, *Coastal Engineering*, 54, 151–170
- Westerink, J. J., R. A. Luettich, C. A. Blain, and N. W. Scheffner, 1992: ADCIRC: An advanced three-dimensional circulation model for shelves, coasts and estuaries; Report 2: Users manual for ADCIRC-2DDI. *Technical Report DRP-92-6*, Headquarters, U.S. Army Corps of Engineers, Washington DC.
- Willoughby, H. E., 1990: Gradient balance in tropical cyclones. *J. Atmos. Sci.*, 47, 265–274.
- Willoughby, H. E., and M. E. Rahn, 2004: Parametric Representation of the Primary Hurricane Vortex. Part I: Observations and Evaluation of the Holland (1980) Model. *American Meteorological Society*, 132, 3033–3048
- Willoughby, H. E., R. W. R. Darling, and M. E. Rahn, 2006: Parametric Representation of the Primary Hurricane Vortex. Part II: A New Family of Sectionally Continuous Profiles. *Monthly Weather Review*, 134, 1102–1120.

- Wood, V. T., and L. W. White, 2011: A new parametric model of vortex tangential-wind profiles: Development, testing, and verification. *J. Atmos. Sci.*, 68, 990–1006.
- Wood, V. T., White, L. W., Willoughby, H. E., and Jorgensen, D. P., 2013: A new parametric tropical cyclone tangential wind profile model. *Mon. Wea. Rev.*, 141, 1884–1909, doi:10.1175/MWR-D-12-00115.1.
- Wright, C. W., E. J. Walsh, D. Vandemark, W. B. Krabill, A. W. Garcia, S. H. Houston, M. D. Powell, P. G. Black, and F. D. Marks, 2001: Hurricane directional wave spectrum spatial variation in the open ocean, *J. Phys. Oceanogr.*, 31, 2472–2488.
- Wu, J., 1982: Wind-stress coefficients over sea surface from breeze to hurricane. *Journal of Geophysical Research*, 87, C12, 9704-9706.
- Xie, L., S. Bao, L. J. Pietrafesa, K. Foley, and M. Fuentes, 2006: A real-time hurricane surface wind forecasting model: Formulation and verification. *Monthly Weather Review*, 134, 1355-1370.
- Yelland, M., and P. K. Taylor, 1996: Wind stress measurements from the open ocean. *J. Phys. Oceanogr.*, 26, 541–558.
- Zhao, W., and S. S. Chen, 2005: A coupled atmosphere-wave-ocean framework for high-resolution modeling of tropical cyclones and coastal storms. *Extended Abstracts, WRF/MM5 Users' Workshop, Boulder, CO, NCAR*, 5.5.
- Zijlema, M., G. Ph. Van Vledder, L. H. Holthuijsen, 2012: Bottom friction and wind drag for wave models, *Coastal Engineering*, 65, 19-26, doi:10.1016/j.coastaleng.2012.03.002.